1 A single-point modeling approach for the intercomparison and
2 evaluation of ozone dry deposition across chemical transport models
3 (Activity 2 of AQMEII4)

4 Olivia E. Clifton[1], Donna Schwede[2], Christian Hogrefe[2], Jesse O. Bash[2], Sam Bland[3], Philip Cheung[4],
5 Mhairi Coyle[5], Lisa Emberson[6], Johannes Flemming[7], Erick Fredj[8], Stefano Galmarini[9], Laurens
6 Ganzeveld[10], Orestis Gazetas[9,11], Ignacio Goded[9], Christopher D. Holmes[12], László Horváth[13], Vincent
7 Huijnen[14], Qian Li[15], Paul A. Makar[4], Ivan Mammarella[16], Giovanni Manca[9], J. William Munger[17], Juan L.
8 Pérez-Camanyo[18], Jonathan Pleim[19], Limei Ran[20], Roberto San Jose[18], Sam J. Silva[21], Ralf Staebler[22],
9 Shihan Sun[23], Amos P. K. Tai[23,24], Eran Tas[15], Timo Vesala[16,25], Tamás Weidinger[26], Zhiyong Wu[27],
10 Leiming Zhang[4]

11
12 [1]NASA Goddard Institute for Space Studies, New York, NY, 10025 USA
13 [2]United States Environmental Protection Agency, Office of Research and Development, Research Triangle Park, NC, 27711
14 USA
15 [3]Stockholm Environment Institute, Environment and Geography Department, University of York, York, YO10 5DD UK
16 [4]Air Quality Research Division, Atmospheric Science and Technology Directorate, Environment and Climate Change Canada,
17 Toronto, M3H 5T4, Canada
18 [5]United Kingdom Centre for Ecology and Hydrology, Bush Estate, Penicuik, Midlothian, EH26 0QB UK, and The James Hutton
19 Institute, Craigiebuckler, Aberdeen, AB15 8QH UK
20 [6]Environment and Geography Department, University of York, York, YO10 5DD UK
21 [7]European Centre for Medium-Range Weather Forecasts, Reading, RG2 9AX UK
22 [8]Department of Computer Science, The Jerusalem College of Technology, Jerusalem, Israel
23 [9] European Commission, Joint Research Centre (JRC), Ispra, Italy
24 [10]Wageningen University, Meteorology and Air Quality Section, Wageningen, the Netherlands
25 [11]Now at: Scottish Universities Environmental Research Centre (SUERC), East Kilbride G75 0QF, UK
26 [12]Earth, Ocean and Atmospheric Science, Florida State University, Tallahassee, FL, 32306 USA
27 [13]Department of Optics and Quantum Electronics, ELKH-SZTE Photoacoustic Research Group, University of Szeged, Szeged,
28 Hungary
29 [14]Royal Netherlands Meteorological Institute, De Bilt, Netherlands
30 [15]The Institute of Environmental Sciences, The Robert H. Smith Faculty of Agriculture, Food and Environment, The Hebrew
31 University of Jerusalem, Rehovot 76100, Israel
32 [16]Institute for Atmospheric and Earth System Research/Physics, University of Helsinki, Helsinki, Finland
33 [17]School of Engineering and Applied Sciences and Department of Earth and Planetary Sciences, Harvard University, Cambridge,
34 MA, USA
35 [18]Computer Science School, Technical University of Madrid (UPM), Madrid, Spain
36 [19]Center for Environmental Measurement & Modeling, U.S. Environmental Protection Agency, Research Triangle Park, NC,
37 USA
38 [20]Natural Resources Conservation Service, US Department of Agriculture, Greensboro, NC, USA
39 [21]Department of Earth Sciences, University of Southern California, Los Angeles, CA
40 [22]Air Quality Processes Section, Environment and Climate Change Canada, Toronto, M3H 5T4, Canada
41 [23]Earth and Environmental Sciences Programme, Faculty of Science, The Chinese University of Hong Kong, Hong Kong, China
42 [24]State Key Laboratory of Agrobiotechnology and Institute of Environment, Energy and Sustainability, The Chinese University
43 of Hong Kong, Hong Kong, China
44 [25]Institute for Atmospheric and Earth System Research/Forest Sciences, University of Helsinki, Helsinki, Finland
45 [26]Department of Meteorology, Institute of Geography and Earth Sciences, Eötvös Loránd University, Pázmány Péter sétány 1/A,
46 Budapest 1117, Hungary

47 [27]ORISE Fellow at Center for Environmental Measurement and Modeling, US Environmental Protection Agency, Research
48 Triangle Park, NC, 27711 USA
49
50 *Correspondence to*: Olivia E. Clifton (olivia.e.clifton@nasa.gov)

51 **Abstract.** A primary sink of air pollutants and their precursors is dry deposition. Dry deposition estimates differ across chemical

52 transport models yet an understanding of the model spread is incomplete. Here we introduce Activity 2 of the Air Quality Model

53 Evaluation International Initiative Phase 4 (AQMEII4). We examine dry deposition schemes from regional and global chemical

54 transport models as well as standalone models used for impacts assessments or process understanding. We configure eighteen

55 schemes as single-point models at eight northern hemisphere locations with observed ozone fluxes. Single-point models are

56 driven by a common set of site-specific meteorological and environmental conditions. Five of eight sites have at least three years

57 and up to twelve years of ozone fluxes. The spread across models that de-emphasizes outliers in multiyear mean ozone

58 deposition velocities ranges from a factor of 1.2 to 1.9 annually across sites and tends to be highest during winter compared to

59 summer. No model is within 50% of observed multiyear averages across all sites and seasons, but some models perform well for

60 some sites and seasons. For the first time, we demonstrate how contributions from depositional pathways vary across models.

61 Models can disagree in relative contributions from the pathways, even when they predict similar deposition velocities, or agree in

62 the relative contributions but predict different deposition velocities. Both stomatal and nonstomatal uptake contribute to the large

63 model spread across sites. Our findings are the beginning of results from AQMEII4 Activity 2, which brings scientists who

64 model air quality and dry deposition together with scientists who measure ozone fluxes to evaluate and improve dry deposition

65 schemes in chemical transport models used for research, planning, and regulatory purposes.

66

67 **Short summary.** A primary sink of air pollutants is dry deposition. Dry deposition estimates differ across models used to

68 simulate atmospheric chemistry on regional to global scales. Here we introduce an effort to examine dry deposition schemes

69 from atmospheric chemistry models. We provide our approach's rationale, document the schemes, and describe datasets used to

70 drive and evaluate the schemes. We also launch the analysis of results by evaluating against observations and identifying the

71 processes leading to model-model differences.

72 **1 Introduction**

73 Dry deposition is a sink of air pollutants and their precursors, removing compounds from the atmosphere after turbulence

74 transports them to the surface and the compounds stick to or react with surfaces. Dry deposition may be a key influence on air

75 pollution levels including high episodes (Vautard et al., 2005; Solberg et al., 2008; Emberson et al., 2013; Huang et al., 2016;

76 Anav et al., 2018; Baublitz et al., 2020; Clifton et al., 2020b; Lin et al., 2020; Gong et al., 2021). Dry deposition can also harm

77 plants when gases diffuse through stomata (Krupa, 2003; Ainsworth et al., 2012; Lombardozzi et al., 2013; Grulke and Heath,

78 2019; Emberson, 2020). In particular, stomatal uptake of ozone adversely impacts crop yields (Mauzerall and Wang, 2001; Tai et

79   al., 2014; McGrath et al., 2015; Guarin et al., 2019; Hong et al., 2020; U.S. EPA 2020a,b), carbon storage (Ren et al., 2007; Sitch
80   et al., 2007; Lombardozzi et al., 2015; Oliver et al., 2018), and ecosystem services (Paoletti et al., 2010; Manes et al., 2012).
81
82   Chemical transport models are key tools for research, planning, and regulatory purposes, including quantifying the influence of
83   meteorology and emissions on air pollution. Accurate estimates of sinks like dry deposition are needed for source attribution.
84   Simulated tropospheric and near surface abundances of air pollutants are highly sensitive to dry deposition (Wild, 2007; Tang et
85   al., 2011; Walker, 2014; Bela et al., 2015; Beddows et al., 2017; Hogrefe et al., 2018; Baublitz et al., 2020; Sharma et al., 2020;
86   Ryan and Wild, 2021; Liu et al., 2022). However, chemical transport models do not always reproduce observed variability in dry
87   deposition or in near-surface abundances of air pollutants expected to be influenced strongly by dry deposition (Hardacre et al.,
88   2015; Clifton et al., 2017; Kavassalis and Murphy, 2017; Silva and Heald, 2018; Travis and Jacob, 2019; Visser et al., 2021;
89   Wong et al., 2022; Ye et al., 2022).
90
91   Dry deposition rates differ across chemical transport models (Dentener et al., 2006; Flechard et al., 2011; Hardacre et al., 2015;
92   Li et al., 2016; Vivanco et al., 2018). Differences can stem from dry deposition scheme (Le Morvan-Quéméner et al., 2018; Wu
93   et al., 2018; Wong et al., 2019; Otu-Larbi et al., 2021; Sun et al., 2022) as well as near-surface concentrations of the air pollutant
94   and model-specific forcing related to meteorology and land use/land cover (LULC) (Hardacre et al., 2015; Tan et al., 2018, Zhao
95   et al., 2018; Huang et al., 2022). Even with the same forcing, deposition velocities, or the strength of the dry deposition
96   independent from near-surface concentrations, can vary by 2- to 3-fold across models (Flechard et al., 2011; Schwede et al.,
97   2011; Wu et al., 2018; Wong et al., 2019; Cao et al., 2022; Sun et al., 2022), highlighting roles for process representation and
98   parameter choice. Minimizing process, parametric, and structural uncertainties in dry deposition schemes is not only important
99   for chemical transport models used for forecasting and regulatory applications, but also for improved understanding of long-term
100   trends and variability in air pollution and impacts on humans, ecosystems, and resources, and building predictive ability using
101   global Earth system and chemistry-climate models (Archibald et al., 2020; Clifton et al., 2020a).
102
103   In addition to dry deposition occurring after diffusion through stomata, dry deposition occurs via nonstomatal pathways,
104   including soil and leaf cuticles, as well as snow and water (Wesely and Hicks, 2000; Helmig et al., 2007; Fowler et al., 2009;
105   Hardacre et al., 2015; Clifton et al., 2020a). A recent review estimates that nonstomatal uptake is 45% on average of ozone dry
106   deposition over physiologically active vegetation (Clifton et al., 2020a). For highly soluble gases, nonstomatal uptake may
107   dominate dry deposition (e.g., Karl et al., 2010; Nguyen et al., 2015; Clifton et al., 2022). Observations show strong unexpected
108   spatiotemporal variations in nonstomatal uptake (Lenschow et al., 1981; Godowitch, 1990; Fuentes et al., 1992; Rondón et al.,
109   1993; Coe et al., 1995; Mahrt et al., 1995; Fowler et al., 2001; Coyle et al., 2009; Helmig et al., 2009; Stella et al., 2011; Rannik
110   et al., 2012; Potier et al., 2015; Wolfe et al., 2015; Fumagalli et al., 2016; Clifton et al., 2017; Clifton et al., 2019; Stella et al.,
111   2019). A dearth of common process-oriented diagnostics has prevented a clear picture of the deposition pathways driving
112   differences in past model intercomparisons.

113   Measured turbulent fluxes are the best existing observational constraints on dry deposition but are limited in informing relative
114   roles of individual deposition pathways (Fares et al., 2017; Clifton et al., 2020a; He et al., 2021). While we can build mechanistic
115   understanding of individual processes with laboratory and field chamber measurements (Fuentes and Gillespie, 1992; Cape et al.,
116   2009; Fares et al., 2014; Fumagalli et al., 2016; Sun et al., 2016a,b; Potier et al., 2017; Finco et al., 2018), the models that are
117   used to scale processes to the ecosystem scale, often the same models used in dry deposition schemes in chemical transport
118   models, are highly empirical and poorly constrained. For example, a recent synthesis finds that while we have basic knowledge
119   of processes controlling ozone dry deposition, the relative importance of various processes remains uncertain and we lack ability
120   to predict spatiotemporal changes (Clifton et al., 2020a).

121   Launched in 2009, the Air Quality Model Evaluation International Initiative (AQMEII) has organized several activities (Rao et
122   al., 2011). The fourth phase of AQMEII emphasizes process-oriented investigation of deposition in a common framework
123   (Galmarini et al., 2021). AQMEII4 has two main activities. Activity 1 evaluates both wet and dry deposition across regional air
124   quality models (Galmarini et al., 2021). Here we introduce Activity 2, which examines dry deposition schemes as standalone
125   single-point models at eight sites with ozone flux observations. Importantly, single-point models are forced with the same, site-
126   specific observational datasets of meteorology and ecosystem characteristics, and thus the intercomparison and evaluation can
127   focus on deposition processes and parameters, as recommended by a recent review (Clifton et al., 2020a).
128
129   The four aims of Activity 2 are:
130   1. To quantify the performance of a variety of dry deposition schemes under identical conditions
131   2. To understand how different deposition pathways contribute to the intermodel spread
132   3. To probe the sensitivity of schemes to environmental factors, and variability in the sensitivities across schemes
133   4. To understand differences in dry deposition simulated in regional models in Activity 1
134
135   Our effort builds on recent work using observation-driven single-point modeling of dry deposition schemes at Borden Forest
136   (Wu et al., 2018), Ispra and Hyytiälä (Visser et al., 2021), and two sites in China (Cao et al., 2022), but is designed to test more
137   sites and schemes as well as gain better understanding of intermodel differences. For example, sites examined represent a range
138   of ecosystems in North America, Europe, and Israel, and single-point models are required to archive process-level diagnostics to
139   facilitate understanding of simulated variations. Although our fourth aim is to contextualize differences among regional air
140   quality models in Activity 1, we also include schemes from global chemical transport models and used always as standalone
141   models to allow for a more comprehensive range of intermodel variation.
142
143   Below we describe single-point models (Sect. 2), as well as the northern hemisphere locations and site-specific meteorological
144   and environmental datasets used to drive and evaluate the models (Sect. 3) and post-processing of observed and simulated values
145   (Sect. 4). Our focus on ozone reflects availability of long-term ozone flux measurements. With five datasets with more than three
146   years of observations, model evaluation can not only examine seasonality and diel cycles, but also interannual and day-to-day

147   variability (unique to this intercomparison). In the results (Sect. 5), we present how models differ in capturing observed

148   seasonality in ozone deposition velocities, including the contribution of different deposition pathways and how some

149   environmental factors drive changes. We focus on multiyear averages and thus climatological evaluation but examine some

150   aspects of interannual variability for sites with ozone flux records with three or more years. We then present a summary of our

151   findings (Sect. 6). To our knowledge, this is the first model intercomparison demonstrating how the contribution of different

152   pathways varies across dry deposition schemes and contributes to the model spread in ozone deposition velocities.

153   **2 Single-point models**

154   Single-point models used here are standalone dry deposition schemes driven by meteorological and environmental inputs from

155   observations at sites with ozone fluxes. The single-point models were extracted from regional models used in AQMEII4 Activity

156   1 as well as other chemical transport models, or are always configured as single-point models. Dry deposition schemes vary in

157   structure and level of detail in terms of the processes represented. Because there is limited documentation in the peer-reviewed

158   literature of dry deposition schemes (especially as the schemes are configured in chemical transport models), and complete and

159   consistent model descriptions aid our effort, we fully describe the participating schemes here. Due to our focus on ozone, we

160   limit our description to dry deposition of ozone. For brevity, we limit our description to the implementation of the schemes in the

161   single-point models at the eight sites examined, as opposed to how the schemes work at larger scales as embedded within the

162   chemical transport models (hereinafter, 'host models').

163

164   We note that surface- and soil-dependent parameter choices in the host model implementation of the schemes have likely been

165   optimized for generalized LULC and soil classification schemes as well as environmental conditions and meteorology generated

166   or used by the host model. Thus, our prescription of common site-specific drivers across the single-point models in this study

167   may create potential inconsistencies with performance inside host models. However, this separation and unification of drivers is

168   key for realistic estimates of the model spread due to parameter choice and process representation.

169

170   Table 1 gives measured and inferred variables or parameters used to force single-point models as well as other common variables

171   used in the models. The meaning and units of variables listed in Table 1 are consistent throughout the manuscript. If a variable is

172   not listed in Table 1 then that variable's meaning and units cannot be assumed to be consistent across models or the manuscript.

173   The first time that we mention variables included in Table 1, we refer to Table 1.

174

175   The forcing variables provide inputs to drive models with detailed dependencies on biophysics, such as coupled photosynthesis-

176   stomatal conductance models, as well as models that depend mainly on atmospheric conditions. Not every model uses every

177   forcing variable. In general, input variables used by each single-point model should reflect the operation of the dry deposition

178   scheme. For example, if the scheme in the host model ingests precipitation to calculate canopy wetness, rather than ingesting

179   canopy wetness, then the single-point model should ingest precipitation to calculate canopy wetness.

180

181   We note that dry deposition schemes in many chemical transport models use methods derived from classic schemes like Wesely

182   (1989). Implementations of classic schemes may deviate from original parameterization description papers in ways that can

183   affect simulated rates (e.g., Hardacre et al., 2015) but may not be well documented. For example, there may be changes to

184   LULC-specific parameters or the use of different LULC categories. In addition, implementations may tie processes to variables

185   like leaf area index to capture seasonal changes rather than relying on season-specific parameters. To foster understanding of

186   how adaptations from original schemes influence simulated dry deposition rates, we encouraged participation in Activity 2 from

187   models using schemes based on classic parameterizations, in addition to models with different approaches.

188   **Table 1: Variables related to forcing datasets for single-point models.**

Variables in forcing data	Other common model variables
B parameter related to soil moisture [unitless]	D_{O_3} diffusivity of ozone in air [m^2 s^{-1}]
$[CO_2]$ ambient carbon dioxide mixing ratio [ppmv]	D_w diffusivity in air of water vapor [m^2 s^{-1}]
d displacement height [m]	D_{CO_2} diffusivity in air of carbon dioxide [m^2 s^{-1}]
f_{wet} fraction of the canopy that is wet [fractional]	e_{sat} saturation vapor pressure [Pa]
G incoming shortwave radiation [W m^{-2}]	f_0 reactivity factor for ozone [unitless]
h canopy height [m]	H Henry's Law constant [M atm^{-1}]
LAI leaf area index [m^2 m^{-2}]	κ thermal diffusivity of air [m^2 s^{-1}]
$[O_3]$ ambient ozone mixing ratio [ppbv]	L Obukhov length [m]
P precipitation rate [mm hr^{-1}]	M_{air} molar mass of air [g mol^{-1}]
p_a air pressure [Pa]	Pr Prandtl number [unitless]
PAR photosynthetically active radiation [μmol m^{-2} s^{-1}]	ρ air density [kg m^{-3}]
RH relative humidity [fractional]	Sc Schmidt number [unitless]
r_0 roughness length [m]	v_d ozone deposition velocity [m s^{-1}]
SD snow depth [cm]	VPD vapor pressure deficit [kPa]
SH sensible heat flux [W m^{-2}]	ψ_{leaf} leaf water potential [MPa]
T_a air temperature [ºC]	ψ_{soil} soil matric potential [kPa]
T_g ground temperature near surface [ºC]	
u wind speed [m s^{-1}]	
u^* friction velocity [m s^{-1}]	
w_g volumetric soil water content near surface [m^3 m^{-3}]	
w_2 volumetric soil water content at root zone [m^3 m^{-3}]	
w_{fc} volumetric soil water content at field capacity [m^3 m^{-3}]	
w_{sat} volumetric soil water content at saturation [m^3 m^{-3}]	
w_{wlt} volumetric soil water content at wilting point [m^3 m^{-3}]	
z_0 roughness length [m]	
z_r reference height [m]	
θ solar zenith angle [º]	

189

190   Like many model intercomparisons, our effort is an 'ensemble of opportunity' (e.g., Galmarini et al., 2004; Tebaldi and Knutti,

191   2007; Potempsky and Galmarini, 2009; Solazzo and Galmarini, 2014; Young et al., 2018) and may underestimate uncertainty

192   due to process, structural, and parametric differences across models. Nonetheless, the design of our effort, with emphasis on

193   processes, parameters, and sensitivities, is designed to explore uncertainty more systematically than past attempts.

194

195   The first set of Activity 2 simulations is driven by inputs from observations, and those simulations are examined here. Future

196   work will examine sensitivity tests in which dry deposition is calculated with perturbed values of input variables (e.g., air

197   temperature, leaf area index). We will also design tests that isolate the influence of input parameters (e.g., initial resistance to

198   stomatal uptake, field capacity of soil).

199

200   Diagnostic outputs required from single-point models follow requirements of Activity 1 (see Table 4 in Galmarini et al. (2021)).

201   Among required outputs are effective conductances (Paulot et al., 2018; Clifton et al., 2020b) for dry deposition to plant stomata,

202   leaf cuticles, the lower canopy, and soil. Not all single-point models simulate deposition to the lower canopy. As explained and

203   defined in Galmarini et al. (2021), an effective conductance [m s^{-1}] represents the portion of v_d that occurs via a single pathway.

204   The sum of the effective conductances is v_d. Archiving effective conductances facilitates comparison of the contribution of each

205   pathway across dry deposition schemes with varying resistance frameworks (i.e., structures) and resistances to transport.

206   Previous model comparisons examine different absolute conductances, suggesting that differences in processes lead to

207   differences in v_d (Wu et al., 2018; Huang et al., 2022); our approach with effective conductances offers an apples-to-apples

208   comparison across models.

209

210   The classic resistance network for ozone deposition velocity (v_d) [m s^{-1}] (Table 1) is based on three resistances, which are added

211   in series, following:

212    $v_d = (r_a + r_b + r_c)^{-1}$ (1)

213   The variable r_a is aerodynamic resistance; r_b is quasi-laminar boundary layer resistance around the bulk surface; r_c is surface

214   resistance. All resistances (denoted by r) are in s m^{-1} throughout the manuscript. Models examined here employ Eq. (1).

215   Exceptions are MLC-CHEM, which is a multilayer canopy model that simulates the ozone concentration gradient within the

216   canopy, and CMAQ STAGE, which uses surface-specific quasi-laminar resistances. Thus, MLC-CHEM and CMAQ STAGE

217   deviate from Eq. (1); we present v_d equations for these models in the individual model subsections below. Otherwise, in this

218   section, we describe methods for r_a and r_b across models (Tables S1, S2, S3), and ozone-specific dry deposition parameters as

219   related to all three main resistances (Table S4). Equations for r_c are in individual model subsections.

220

221   All models except one use r_a equations based on Monin-Obukhov Similarity Theory (Table S1). However, the exact forms of the

222   equations vary across models. Obukhov length (L) [m] (Table 1) is often used in r_a equations but is not observed. Most model L

223   equations are similar, apart from whether models use virtual or ambient temperature and whether they include bounds on L (and

224   what the bounds are) (Table S2).

225

226   Models are configured to accept inputs and return predicted values at the specified ozone flux measurement height at the given

227   site (i.e., reference height z_r [m] (Table 1)). Roughness length (z_0) [m] (Table 1) and displacement height (d) [m] (Table 1) are

228   also often used in r_a equations yet are not observed, and are especially important in estimating fluxes at z_r rather than the lowest

229 atmospheric level of the host model. Thus, we supply consistent estimates of these variables across the models that employ them.

230 Estimates follow Meyers et al. (1998):

231 $z_0 = h\left(0.23 - \frac{LAI^{0.25}}{10} - \frac{a-1}{10}\right)$ (2)

232 $d = h\left(0.05 + \frac{LAI^{0.2}}{2} + \frac{a-1}{20}\right)$ (3)

233 The variable h [m] is canopy height (Table 1); LAI [m^2 m^{-2}] is leaf area index (Table 1); a [unitless] is a parameter based on

234 LULC (Meyers et al., 1998). Meyers et al. (1998) suggest a correction for z_0 if $LAI < 1$ but we do not employ this correction

235 given that it creates discontinuities in the time series.

236

237 For models employing quasi-laminar boundary layer resistance around the bulk surface (i.e., r_b in Eq. (1)), most use r_b from

238 Wesely and Hicks (1977) (Table S3). A key part of r_b parameterizations is the ratio scaling the quasi-laminar boundary layer

239 resistance for heat to ozone ($R_{diff,b}$) (Table S4). Fundamentally, $R_{diff,b} = Sc/Pr$, where Sc [unitless] is the Schmidt number

240 (Table 1) and Pr [unitless] is the Prandtl number (Table 1). All but one employ $R_{diff,b} = Sc/Pr = \kappa/D_{O_3}$ where κ [m^2 s^{-1}] is

241 thermal diffusivity of air (Table 1), and D_{O_3} [m^2 s^{-1}] is ozone diffusivity in air (Table 1); however, values of κ and D_{O_3} vary

242 across models (Table S4).

243

244 Table S4 also presents model prescriptions for the ratio that scales stomatal resistance from water vapor to ozone ($R_{diff,st}$),

245 reactivity factor for ozone (f_0) [unitless] (Table 1), and Henry's Law constant for ozone (H) [M atm^{-1}] (Table 1). Where used,

246 values of f_0 and H are very similar across models. Some models employ temperature dependencies on H. Notably, values of

247 $R_{diff,st}$ vary from 1.2 to 1.7 across models. The current estimate of this ratio is 1.61 (Massman, 1998). GEM-MACH Zhang and

248 models based on GEOS-Chem prescribe lower $R_{diff,st}$ values.

249 **2.1 Documentation of single-point models**

250 **2.1.1 WRF-Chem Wesely**

251 WRF-Chem uses a scheme based on Wesely (1989). Parameters in Table S5 are site- and season-specific. WRF-Chem has two

252 seasons: midsummer with lush vegetation [day of year between 90 and 270] and autumn with unharvested croplands [day of year

253 less than 90 or greater than 270]. If we reference Table S5, then the parameter's value is in Table S5.

254 Surface resistance (r_c) follows:

255 $r_c = \left(\frac{1}{r_{st}+r_m} + \frac{1}{r_{cut}} + \frac{1}{r_{dc}+(r_{cl}+r_T)} + \frac{1}{r_{ac}+(r_g+r_T)}\right)^{-1}$ (4)

256 Stomatal resistance (r_{st}) follows:

257 $r_{st} = R_{diff,st}\, \frac{r_i}{f(T_a)\, f(G)}$ (5)

258 The parameter r_i is initial resistance for stomatal uptake (Table S5).

259 Effects of air temperature (T_a) [ºC] (Table 1) follow:

8

260     $f(T_a) = T_a \frac{(40 - T_a)}{400}$ (6)

261   Effects of incoming shortwave radiation (G) [W m^{-2}] (Table 1) follow:

262     $f(G) = \left(1 + \left(\frac{200}{G + 0.1}\right)^2\right)^{-1}$ (7)

263   Mesophyll resistance (r_m) follows:

264     $r_m = \left(\frac{H}{3000} + 100 f_0\right)^{-1}$ (8)

265   Cuticular resistance (r_{cut}) follows:

266     $r_{cut} = \frac{r_{lu} + r_T}{\frac{H}{10^5} + f_0}$ (9)

267   The parameter r_{lu} is initial resistance for cuticular uptake (Table S5). If relative humidity (RH) [fractional] (Table 1) is greater

268   than 0.95 or precipitation rate (P) [mm hr^{-1}] (Table 1) is greater than zero then:

269     $r_{cut} = \left(\frac{1}{W} + \frac{3}{r_{lu} + r_T}\right)^{-1}$ (10)

270   The parameter W equals 3000 if P equals zero whereas W equals 1000 if P is greater than zero.

271   The resistance associated with within-canopy convection (r_{dc}) follows:

272     $r_{dc} = 100 \left(1 + \frac{1000}{G}\right)$ (11)

273   Resistances to the lower canopy (r_{cl}), in-canopy turbulence (r_{ac}), and soil (r_g) are prescribed (Table S5). To consider effects of

274   T_a, resistance r_T (Walmsley and Wesely, 1996) follows:

275     $r_T = 1000 \, e^{-T_a - 4}$ (12)

276   **2.1.2 GEOS-Chem Wesely**
277   GEOS-Chem is based on Wesely (1989). Wang et al. (1998) describe the initial implementation. We examine the scheme from

278   GEOS-Chem v13.3. Parameters in Table S6 are site-specific. If there is snow, then r_c is calculated with the snow parameters in

279   Table S6. If we reference Table S6, then the parameter's value in Table S6.

280   Surface resistance (r_c) follows:

281     $r_c = \left(\frac{1}{r_{st} + r_m} + \frac{1}{r_{cut}} + \frac{1}{r_{dc} + r_{cl}} + \frac{1}{r_{ac} + r_g}\right)^{-1}$ (13)

282   Stomatal resistance (r_{st}) follows:

283     $r_{st} = R_{diff,st} \frac{r_i}{LAI_{eff} \, f(T_a)}$ (14)

284   The parameter r_i is initial resistance to stomatal uptake (Table S6); LAI_{eff} [m^2 m^{-2}] is effective LAI of actively transpiring

285   leaves. The variable LAI_{eff} is calculated using function of LAI, solar zenith angle (θ) [°] (Table 1), and cloud fraction. In GEOS-

286   Chem, if G is zero then LAI_{eff} equals 0.01. For the single-point model, we set G to be zero when θ is greater than 95° so that

287   nighttime r_{st} values in the single-point model more similar to GEOS-Chem. GEOS-Chem almost never has non-zero G at night

288   but measured values are frequently small and non-zero. Here cloud fraction is assumed to be zero.

289   Effects of T_a follows:

290    $$f\,(T_a) = \begin{cases} 0.01, \; T_a \leq 0 \\ T_a \frac{(40 - T_a)}{400}, \; 0 < T_a < 40 \\ 0.01, \; 40 \leq T_a \end{cases} (15)$$

291   Mesophyll resistance (r_m) follows:

292    $r_m = \left(\frac{H}{3000} + 100\, f_0 \right)^{-1} (16)$

293   Cuticular resistance (r_{cut}) follows:

294    $$r_{cut} = \begin{cases} \frac{r_{lu} + \min\{r_T, r_{lu}\}}{LAI} \left(\frac{H}{10^5} + f_0 \right)^{-1}, \frac{r_{lu} + \min\{r_T, r_{lu}\}}{LAI} < 9999 \\ 10^{12}, \frac{r_{lu} + \min\{r_T, r_{lu}\}}{LAI} \geq 9999 \end{cases} (17)$$

295   The parameter r_{lu} is initial resistance for cuticular uptake (Table S6).

296   To consider effects of T_a, resistance r_T follows:

297    $r_T = 1000\, e^{-T_a - 4} (18)$

298   The resistance associated with in-canopy convection (r_{dc}) follows:

299    $r_{dc} = 100 \left(1 + \frac{1000}{G + 10} \right) (19)$

300   The resistance to surfaces in the lower canopy (r_{cl}) follows:

301    $r_{cl} = \left(\frac{H}{10^5 (r_{cl,S} + \min\{r_T, r_{cl,S}\})} + \frac{f_0}{r_{cl,O} + \min\{r_T, r_{cl,O}\}} \right)^{-1} (20)$

302   Parameters $r_{cl,S}$ and $r_{cl,O}$ are initial resistances to the lower canopy (Table S6).

303   The resistance to turbulent transport to the soil (r_{ac}) is constant (Table S6). Resistance to soil (r_g) follows:

304    $r_g = \left(\frac{H}{10^5 (r_{g,S} + \min\{r_T, r_{g,S}\})} + \frac{f_0}{r_{g,O} + \min\{r_T, r_{g,O}\}} \right)^{-1} (21)$

305   Parameters $r_{g,S}$ and $r_{g,O}$ are initial resistances to uptake on soil (Table S6).

306   **2.1.3 IFS**
307   ECMWF IFS uses two schemes based on Wesely (1989): Meteo-France's SUMO (Michou et al., 2004) ("IFS SUMO Wesely")
308   and GEOS-Chem 12.7.2 ("IFS GEOS-Chem Wesely"). First, we describe components that are the same between schemes.
309   Second, we detail components specific to IFS SUMO Wesely and then to IFS GEOS-Chem Wesely. IFS SUMO Wesely
310   parameters in Table S7 are site- and season-specific. Seasons are defined as: 'transitional spring' [March, April, May], 'mid-
311   summer' [June, July, August], 'autumn' [September, October, November] and 'late autumn' [December, January, February].
312   Otherwise, if there is snow then the model employs the 'winter, snow' parameter values. IFS GEOS-Chem Wesely parameters
313   in Table S8 are site-specific. If there is snow, then the model employs the snow type. For snow type, only r_{cl} is defined [1000 s
314   m^{-1}]. If we reference one of the tables, then the parameter's value is in the table.
315   Surface resistance (r_c) follows:

316    $r_c = \left(\frac{1}{r_{st} + r_m} + \frac{1}{r_{cut}} + \frac{1}{r_{dc} + r_{cl}} + \frac{1}{r_{ac} + (r_g + r_T)} \right)^{-1}$ (22)

317   Mesophyll resistance (r_m) follows:

318    $r_m = \left(\frac{H}{3000} + 100 f_0 \right)^{-1}$ (23)

319   The resistance associated with in-canopy convection (r_{dc}) follows:

320    $r_{dc} = 100 \left(1 + \frac{1000}{G} \right)$ (24)

321   Resistances to surfaces in the lower canopy (r_{cl}), in-canopy turbulence (r_{ac}), and soil (r_g) are prescribed (Tables S7 and S8). To

322   consider effects of T_a, resistance r_T follows:

323    $r_T = 1000 \, e^{-T_a - 4}$ (25)

324   For IFS SUMO Wesely, stomatal resistance (r_{st}) follows:

325    $r_{st} = R_{diff,st} \, \frac{r_i}{LAI \, f(G) \, f(VPD) \, f(w_2)}$ (26)

326   The parameter r_i is initial resistance to stomatal uptake (Table S7).

327   Effects of G follow:

328    $f(G) = \min \left\{ \frac{0.004 \, G + 0.5}{0.81 \, (0.004 \, G + 1)}, 1 \right\}$ (27)

329   Effects of vapor pressure deficit (VPD) [kPa] (Table 1) follow:

330    $f(VPD) = e^{0.3 \, VPD}$ (28)

331   Equation (28) is only employed for forests, otherwise $f(VPD)$ equals 1.

332   Effects of root-zone soil water content (w_2) [m^3 m^{-3}] (Table 1) follow:

333    $f(w_2) = \begin{cases} 0, w_2 < w_{wlt} \\ \frac{w_2 - w_{wlt}}{w_{fc} - w_{wlt}}, w_{wlt} < w_2 < w_{fc} \\ 1, \ w_2 > w_{fc} \end{cases}$ (29)

334   Cuticular resistance (r_{cut}) follows:

335    $r_{cut} = (r_{lu} + r_T) \left(\frac{H}{10^5} + f_0 \right)^{-1}$ (30)

336   The parameter r_{lu} is initial resistance for cuticular uptake (Table S7).

337   For IFS GEOS-Chem Wesely, stomatal resistance (r_{st}) follows Wang et al. (1998):

338    $r_{st} = R_{diff,st} \, \frac{r_i}{LAI_{eff} \, f(T_a)}$ (40)

339   The parameter r_i is initial resistance to stomatal uptake (Table S8); LAI_{eff} [m^2 m^{-2}] is effective LAI of actively transpiring

340   leaves. The variable LAI_{eff} is calculated as a function of LAI, θ, and cloud fraction. In GEOS-Chem, if G is zero then LAI_{eff} is

341   equal to 0.01. For the single-point model, we set G to be zero when θ is greater than 95°. GEOS-Chem almost never has non-

342   zero G at night but measured values are frequently small and non-zero. This change makes nighttime r_{st} values in the single-

343   point model more similar GEOS-Chem. Here cloud fraction is assumed to be zero.

344   Effects of T_a follow:

345 $f(T_a) = T_a \frac{40 - T_a}{400}$ (41)

346 Cuticular resistance (r_{cut}) follows:

347 $r_{cut} = \frac{(r_{lu} + r_T)}{LAI} \left(\frac{H}{10^5} + f_0 \right)^{-1}$ (42)

348 The parameter r_{lu} is initial resistance to cuticular uptake (Table S8).

349 **2.1.4 GEM-MACH Wesely**

350 Operationally, GEM-MACH uses a dry deposition scheme based on Wesely (1989) (Makar et al., 2018). Parameters defined in

351 Table S9 are site- and sometimes season-specific. Table S10 describes how seasons are distributed as a function of month and

352 latitude. If we reference Table S9, then the parameter's value is in Table S9.

353 Surface resistance (r_c) follows:

354 $r_c = \left(\frac{1 - W_{st}}{r_{st} + r_m} + \frac{1}{r_{cut}} + \frac{1}{r_{dc} + r_{cl}} + \frac{1}{r_{ac} + r_g} \right)^{-1}$ (43)

355 The variable W_{st} [fractional] is used to account for leaf wetness; W_{st} is 0.5 if P is greater than 1 mm hr^{-1} or RH is greater than

356 0.95 and zero otherwise.

357 Stomatal resistance (r_{st}) is based on Jarvis (1976), Zhang et al. (2002a, 2003) and Baldocchi et al. (1987):

358 $r_{st} = R_{diff,st} \frac{r_i}{LAI \max\{f(G) f(VPD) f(T_a) f(c_a), \ 0.0001\}}$ (44)

359 The parameter r_i is initial resistance to stomatal uptake (Table S9).

360 Curve-fitting of data from Jarvis (1976) and Ellsworth and Reich (1993) was used to infer the following:

361 $f(G) = \max \{0.206 \ln(G) - 0.605, 0\}$ (45)

362 Effects of VPD follow:

363 $f(VPD) = \max \left\{ 0.0, \max \left\{ 1.0, \left(1.0 - 0.03 \left(1 - RH \right) 10^{\frac{0.7859 + 0.03477 T_a}{1 + 0.00412 T_a}} \right) \right\} \right\}$ (46)

364 Effects of T_a follow:

365 $f(T_a) = \left(\frac{(T_a - T_{min}) (T_{max} - T_a)}{(T_{opt} - T_{min}) (T_{max} - T_{opt})} \right)^{0.62}$ (47)

366 Parameters $T_{min}, T_{max},$ and T_{opt} [ºC] are minimum, maximum, and optimum temperature, respectively (Table S9).

367 Effects of ambient carbon dioxide mixing ratio ($[CO_2]$) [ppmv] (Table 1) follow:

368 $f(c_a) = \begin{cases} 1, & [CO_2] \leq 100 \\ 1 - \left(7.35 \ x \ 10^{-4} \ \ln\big(\ln(G)\big) - 8.75 \ x \ 10^{-4} \right) [CO_2], & 100 < [CO_2] < 1000 \\ 0, & [CO_2] \geq 1000 \end{cases}$ (48)

369 Mesophyll resistance (r_m) follows:

370 $r_m = \left(LAI \left(\frac{H}{3000} + 100 f_0 \right) \right)^{-1}$ (49)

371 Cuticular resistance (r_{cut}) follows:

372 $r_{cut} = \frac{r_{lu}}{LAI} \left(\frac{H}{10^5} + f_0 \right)^{-1}$ (50)

373   The parameter r_{lu} is initial resistance to cuticular uptake (Table S9).

374   The resistance associated with in-canopy convection (r_{dc}) follows:

375    $r_{dc} = 100 + \left(1 + \frac{1000}{G + 10}\right)$ (51)

376   The resistance posed by uptake to the lower canopy (r_{cl}) follows:

377    $r_{cl} = \left(\frac{H}{10^5 r_{cl,S}} + \frac{f_0}{r_{cl,O}}\right)^{-1}$ (52)

378   Parameters $r_{cl,S}$ and $r_{cl,O}$ are initial resistances to uptake by surfaces in the lower canopy (Table S9).

379   The parameter r_{ac} is resistance to in-canopy turbulence and r_g is resistance to soil; both are prescribed (Table S9).

380   **2.1.5 GEM-MACH Zhang**

381   GEM-MACH also has an implementation of Zhang et al. (2002b). Parameters in Table S11 are site-specific. If we reference

382   Table S11, then the parameter's value is in Table S11.

383   Surface resistance (r_c) follows:

384    $r_c = \min\left\{10, \left(\frac{1 - W_{st}}{r_{st}} + \frac{1}{r_{cut}} + \frac{1}{r_{ac} + r_g}\right)^{-1}\right\}$ (53)

385   The variable W_{st} [fractional] is used to account for leaf wetness; W_{st} is zero unless precipitation or dew is occurring using the

386   below thresholds, and G is greater than 200 W m^{-2}. If this is the case,

387    $W_{st} = \min\left\{0.5, \frac{G - 200}{800}\right\}$ (54)

388   Precipitation is assumed to occur if T_a is greater than -1ºC and P is greater than 0.20 mm hr^{-1}. Dew is assumed to occur if T_a is

389   greater than -1ºC and P is less than 0.20 mm hr^{-1} and

390    $u^* < c_{dew} \frac{1.5}{\max\left\{1 \times 10^{-4}, \frac{0.622\, e_{sat}\,(1-RH)}{p_a}\right\}}$ (55)

391   The variable e_{sat} [Pa] is saturation vapor pressure (Table 1); p_a [Pa] is air pressure (Table 1); c_{dew} is the dew coefficient [0.3].

392   Stomatal resistance (r_{st}) follows:

393    $r_{st} = R_{diff,st} \frac{r_i(LAI, PAR)}{f(T_a)\, f(VPD)\, f(\psi_{leaf})}$ (56)

394   The variable $r_i(LAI, PAR)$ is initial resistance to stomatal uptake that varies with LAI and PAR, based on Norman (1982) and

395   Zhang et al. (2001):

396    $r_i(LAI, PAR) = \left(\frac{LAI_{sun}}{r_i\left(1 + \frac{b_{rs}}{PAR_{sun}}\right)} + \frac{LAI_{shd}}{r_i\left(1 + \frac{b_{rs}}{PAR_{shd}}\right)}\right)^{-1}$ (57)

397   The parameter r_i is initial resistance to stomatal uptake (Table S11); b_{rs} [W m^{-2}] is empirical (Table S11); LAI_{sun} and LAI_{shd}

398   [m^2 m^{-2}] are sunlit and shaded LAI:

399    $LAI_{sun} = \frac{1 - e^{-K_b LAI}}{K_b}$ (58)

400    $LAI_{shd} = LAI - LAI_{sun}$ (59)

401   The variable K_b is canopy light extinction coefficient [unitless]:

402    $K_b = \frac{0.5}{\cos\left(\frac{\pi}{180}\theta\right)}$ (60)

403   Variables PAR_{sun} and PAR_{shd} [W m^{-2}] are photosynthetically active radiation reaching sunlit and shaded leaves:

404    $PAR_{shd} = PAR_{diff}\, e^{-0.5\, LAI^a} + 0.07\, PAR_{dir}\, (1 - 0.1\, LAI)e^{-\cos\left(\frac{\pi}{180}\theta\right)}$ (61)

405    $PAR_{sun} = PAR_{shd} + \frac{0.5\, PAR_{dir}^b}{\cos\left(\frac{\pi}{180}\theta\right)}$ (62)

406   If LAI is greater than 2.5 m^2 m^{-2} and G is less than 200 W m^{-2}, then empirical parameters a equals 0.8 and b equals 0.8.

407   Otherwise, a equals 0.07 and b equals 1. Calculation of direct and diffuse components of PAR (PAR_{dir} and PAR_{diff}) has been

408   updated from Zhang et al. (2001) to follow Iqbal (1983):

409    $PAR_{dir} = G\, FRAD_V\, FD_V$ (63)

410    $PAR_{diff} = G\, FRAD_V\, (1 - FD_V)$ (64)

411   The variable $FRAD_v$ follows:

412    $FRAD_V = \frac{R_V}{R_V + R_N}$ (65)

413   Variables R_v and R_N follow:

414    $R_N = RD_M + RD_N$ (66)

415    $R_V = RD_U + RD_V$ (67)

416   The variable RD_U follows:

417    $RD_U = 600 \cos\left(\frac{\pi}{180}\theta\right) e^{\frac{-0.185\, p_a}{p_{std} \cos\left(\frac{\pi}{180}\theta\right)}}$ (68)

418   The variable p_{std} is standard air pressure [1.0132 x 10^5 Pa].

419   The variable RD_V follows:

420    $RD_V = 0.42\, (600 - RD_U) \cos\left(\frac{\pi}{180}\theta\right)$ (69)

421   The variable RD_M follows:

422    $RD_M = \cos\left(\frac{\pi}{180}\theta\right)\left(720\, e^{\left(-\frac{0.06\, p_a}{p_{std} \cos\left(\frac{\pi}{180}\theta\right)}\right)} - \left(1320 * 0.077 \left(\frac{2\, p_a}{p_{std} \cos\left(\frac{\pi}{180}\theta\right)}\right)^{0.3}\right)\right)$ (70)

423   The variable RD_N follows:

424    $RD_N = 0.65 \cos\left(\frac{\pi}{180}\theta\right)\left(720 - RD_M - \left(1320 * 0.077 \left(\frac{2\, p_a}{p_{std} \cos\left(\frac{\pi}{180}\theta\right)}\right)^{0.3}\right)\right)$ (71)

425   The variable FD_v follows:

426 $$FD_V = \begin{cases} 0.941124 \, RD_U/R_V & \frac{G}{R_V+R_N} \geq 0.89 \\ \left(1 - \left(\frac{\left(0.9 - \frac{G}{R_V+R_N}\right)}{0.7}\right)^{\frac{2}{3}}\right) RD_U/R_V & 0.21 \geq \frac{G}{R_V+R_N} < 0.89 \\ 0.00955 \, RD_U/R_V & \frac{G}{R_V+R_N} < 0.21 \end{cases} \quad (72)$$

427 Effects of T_a follow:

428 $$f(T_a) = \left(\frac{T_a - T_{min}}{T_{opt} - T_{min}}\right)\left(\frac{T_{max} - T_a}{T_{max} - T_{opt}}\right)^{\frac{T_{max} - T_{opt}}{T_{max} - T_{min}}} \quad (73)$$

429 Parameters T_{min}, T_{max}, and T_{opt} [ºC] are minimum, maximum, and optimum temperature, respectively (Table S11).

430 Effects of VPD follow:

431 $$f(VPD) = \min\{\max\{1 - b_{vpd} \, VPD, 0\}, 1\} \quad (74)$$

432 The parameter b_{vpd} [kPa⁻¹] is empirical (Table S11).

433 Effects of leaf water potential (ψ_{leaf}) [MPa] (Table 1) follow:

434 $$f\left(\psi_{leaf}\right) = \min\left\{\max\left\{\frac{\psi_{leaf} - \psi_{leaf,2}}{\psi_{leaf,1} - \psi_{leaf,2}}, 0\right\}, 1\right\} \quad (75)$$

435 The variable ψ_{leaf} is approximated as:

436 $$\psi_{leaf} = -0.72 - 0.0013 \, G \quad (76)$$

437 Parameters $\psi_{leaf,1}$ and $\psi_{leaf,1}$ [MPa] are empirical (Table S11).

438 If T_a is greater than or equal to -1 ºC and there is neither precipitation nor dew then cuticular resistance (r_{cut}) follows:

439 $$r_{cut} = \max\left\{100, \frac{c_{cut,dry}}{u^* \, LAI^{0.25} \, e^{3 \, RH}}\right\} \quad (77)$$

440 The variable u^* [m s⁻¹] is friction velocity (Table 1); $c_{cut,dry}$ [unitless] is a coefficient related to dry cuticular uptake (Table S11).

441 If T_a is less than -1ºC and there is neither precipitation nor dew then:

442 $$r_{cut} = \max\left\{100, \frac{r_{cut,dry}}{u^* \, LAI^{0.25} \, e^{3 \, RH}} \, \min\{2, e^{0.2 \, (-1 \, - \, T_a)}\}\right\} \quad (78)$$

443 If there is precipitation or dew and T_a is greater than or equal to -1ºC then:

444 $$r_{cut} = \frac{c_{cut,wet}}{u^* \, \sqrt{LAI}} \quad (79)$$

445 The parameter $c_{cut,wet}$ [unitless] is a coefficient related to dry cuticular uptake (Table S11).

446 If the fraction of snow coverage (f_{snow}) is greater than 10^{-4} then a correction is applied:

447 $$r_{cut} = \left(\frac{1 - f_{snow}}{r_{cut}} + \frac{f_{snow}}{2000}\right)^{-1} \quad (80)$$

448 If LAI is less than 2 x 10⁻⁶ m² m⁻² then r_{cut} is very large.

449 The resistance to in-canopy turbulence (r_{ac}) follows:

450 $$r_{ac} = r_{ac0} \frac{LAI^{0.25}}{(u^*)^2} \quad (81)$$

451 The variable r_{ac0} follows:

452 $$r_{ac0} = r_{ac0,min} + \frac{LAI - LAI_{min}}{LAI_{max} - LAI_{min}} \left(r_{ac0,max} - r_{ac0,min} \right) \quad (82)$$

453 Parameters LAI_{min} and LAI_{max} [m^2 m^{-2}] are minimum and maximum LAI across the site's observational record; $r_{ac0,min}$ and

454 $r_{ac0,max}$ are initial resistances (Table S11).

455 Soil resistance (r_g) is prescribed but modified under certain conditions. If T_s is less than -1ºC then:

456 $$r_g = r_g \min\{2, e^{-0.2 \, (T_s + 1)}\} \quad (83)$$

457 The near-surface air temperature (T_s) is approximated from a linear interpolation between T_a and T_g to a height of 1.5 m. If f_{snow}

458 is greater than or equal to 10^{-4} then:

459 $$r_g = \left(\frac{1 - \min\{1, \, 2f_{snow}\}}{r_g} + \frac{\min\{1, \, 2f_{snow}\}}{2000} \right)^{-1} \quad (84)$$

460 The fraction of snow coverage (f_{snow}) follows:

461 $$f_{snow} = \min\left\{1, \frac{SD}{SD_{max}}\right\} \quad (85)$$

462 The variable SD [cm] is snow depth (Table 1); SD_{max} [cm] is maximum snow depth (Table S11).

463 **2.1.6 CMAQ M3Dry**

464 M3Dry (Pleim and Ran, 2011) is designed to couple with the Pleim-Xiu land surface model (PX LSM; Pleim and Xiu, 1995) in

465 the Weather Research and Forecasting (WRF) model and is used operationally in CMAQ. There is also M3Dry-psn, which

466 follows M3Dry but uses a coupled photosynthesis-stomatal conductance model. M3DRY-psn was developed and evaluated with

467 the intention to supplement PX LSM and M3Dry in CMAQ (Ran et al., 2017). To date, however, M3DRY-psn has not been

468 implemented in CMAQ. We first describe M3Dry, and then M3Dry-psn. Parameters in Table S12 are site-specific. If we

469 reference Table S12, then the parameter's value is in Table S12.

470 Surface resistance (r_c) follows:

471 $$r_c = \left(f_{veg} \left(\frac{1}{r_{st} + r_m} + \frac{(1 - f_{wet}) \, LAI}{r_{cut,dry}} + \frac{f_{wet} \, LAI}{r_{cut,wet}} + \frac{1}{r_{ac} + r_g} \right) + \frac{1 - f_{veg}}{r_g} \right)^{-1} \quad (86)$$

472 The parameter f_{veg} is the fraction of the site covered by the vegetation canopy (Table S12); f_{wet} is the fraction of canopy that is

473 wet (Table 1).

474 Mesophyll resistance (r_m) follows:

475 $$r_m = \frac{0.01}{LAI} \quad (87)$$

476 Stomatal resistance (r_{st}) follows Xiu and Pleim (2001):

477 $$r_{st} = R_{diff,st} \frac{r_i}{LAI \, f(PAR) \, f(w_2) \, f(RH_l) \, f(T_a)} \quad (88)$$

478 The parameter r_i is initial resistance to stomatal uptake (Table S12).

479 Effects of photosynthetically active radiation (PAR) [μmol m^{-2} s^{-1}] (Table 1) follow Echer and Rosolem (2015):

480 $$f(PAR) = (1 - a\,LAI)(1 - e^{-0.0017\,PAR}) \quad (89)$$

481 The parameter a [unitless] is empirical (Table S12).

482 Effects of w_2 follow Xiu and Pleim (2001):

483 $$f(w_2) = \left(1 + e^{-5\left(\frac{w_2 - w_{wlt}}{w_{fc} - w_{wlt}} - \left(\frac{w_{fc} - w_{wlt}}{3} + w_{wlt}\right)\right)}\right)^{-1} \quad (90)$$

484 Effects of leaf-level RH (RH_l) [fractional] follow:

485 $$f(RH_l) = RH_l = \frac{q_a\,(r_a + r_{b,v})^{-1} + q_s\,r_{st,v}^{-1}}{\left(r_{st,v}^{-1} + (r_a + r_{b,v})^{-1}\right) q_s} \quad (91)$$

486 The variable q_a is ambient air humidity mixing ratio, q_s is saturation mixing ratio at leaf temperature (T_{leaf}), $r_{b,v}$ is quasi-

487 laminar boundary layer resistance for water vapor and $r_{st,v}$ is stomatal resistance for water vapor. M3Dry assumes: when

488 sensible heat flux (SH) [W m^{-2}] (Table 1) is greater than 0, then T_{leaf} equals $T_a - \frac{SH}{(r_a + r_{b,h})\,\rho\,c_p}$ where $r_{b,h}$ is quasi-laminar

489 boundary layer resistance for heat. Otherwise, T_{leaf} equals T_a. Equation (91) is computed using an implicit quadratic solution as

490 described by Xiu and Pleim (2001).

491 Effects of T_a follow:

492 $$f(T_a) = \begin{cases} \left(1 + e^{-0.41\,(T_a - 8.9)}\right)^{-1}, & T_a \leq 29 \\ \left(1 + e^{0.5\,(T_a - 40.85)}\right)^{-1}, & T_a > 29 \end{cases} \quad (92)$$

493 The variable $r_{cut,wet}$ is the resistance to wet cuticles:

494 $$r_{cut,wet} = \begin{cases} 1250, & T_g > 0 \\ 6667, & T_g < 0 \end{cases} \quad (93)$$

495 The variable T_g [ºC] is ground temperature near surface (Table 1).

496 The variable $r_{cut,dry}$ is resistance to dry cuticles:

497 $$r_{cut,dry} = r_{cut,dry,0}(1 - f(RH)) + r_{cut,wet}\,f(RH) \quad (94)$$

498 The parameter $r_{cut,dry,0}$ equals 2000 s m^{-1}. Effects of RH follow:

499 $$f(RH) = \max\left\{100 * \frac{RH - 0.7}{0.3}, 0\right\} \quad (95)$$

500 The resistance to in-canopy turbulence (r_{ac}) follows Erisman et al. (1994):

501 $$r_{ac} = 14\frac{h\,LAI}{u_*} \quad (96)$$

502 Soil resistance (r_g) follows:

503 $$r_g = \begin{cases} \left(\frac{1 - f_{wet}}{r_{g,dry}} + \frac{f_{wet}}{r_{g,wet}}\right)^{-1}, & no\ snow \\ \left(\frac{1 - X_m}{r_{snow}} + \frac{X_m}{r_{sndiff} + r_{g,wet}}\right)^{-1}, & snow \end{cases} \quad (97)$$

504 $r_{g,wet} = \begin{cases} 500, T_g > 0 \\ 6667, T_g < 0 \end{cases}$ (98)

505 The variable $r_{g,dry}$ follows (Massman, 2004; Mészáros et al., 2009):

506 $r_{g,dry} = 200 + \left(r_{g,wet} - 200\right)\frac{w_g}{w_{fc}}$ (99)

507 If near-surface soil water content (w_g) [m^3 m^{-3}] (Table 1) is greater than soil water content at field capacity (w_{fc}) [m^3 m^{-3}] (Table

508 1) then soil is wet (i.e., $r_{g,dry}$ equals $r_{g,wet}$). The parameter r_{snow} is resistance to snow or ice [6667 s m^{-1}]; r_{sndiff} is resistance to

509 diffusion through snowpack [10 s m^{-1}]. Parallel pathways to frozen snow/ice and diffusion through snowpack to liquid water

510 follow Bales et al. (1987). Snow liquid water mass (X_m) follows:

511 $X_m = \begin{cases} \max\{0.02(T_a + 1)^2, \ 0.5\}, \ T_a > -1 \\ 0, T_a < -1 \end{cases}$ (100)

512 M3Dry-psn simulates r_{st} at leaf level using the Ball-Woodrow-Berry approach (Ball et al., 1987) as described by Collatz et al.

513 (1991, 1992) and Bonan et al. (2011):

514 $r_{st} = \left(g_0 + g_1 \frac{A_n}{\frac{p_{CO_2,l}}{p_a}} RH_l \right)^{-1} \frac{D_{CO_2}}{D_{O_3}} \frac{1000.0 \, \rho}{M_{air}}$ (101)

515 The parameter g_0 equals 0.01 mol CO$_2$ m^{-2} s^{-1} for C$_3$ plants; g_1 equals 9 [unitless]; A_n is leaf-level net photosynthesis [mol CO$_2$

516 m^{-2} s^{-1}]; $p_{CO_2,l}$ is carbon dioxide partial pressure at the leaf surface [Pa]; RH_l is leaf-level RH [fractional], which follows Eq. (91)

517 as described for M3Dry; D_{CO_2} [m^2 s^{-1}] is carbon dioxide diffusivity in air (Table 1); ρ [kg m^{-3}] is air density (Table 1); M_{air} [g

518 mol^{-1}] is molar mass of air (Table 1). Leaf-level A_n is estimated based on Farquhar et al. (1980) as described by Ran et al.

519 (2017), based on co-limitation among three potential assimilation rates, limited by Rubisco, light, and transport of photosynthetic

520 products. The maximum rate of carboxylation of Rubisco (V_{cmax}) [µmol m^2 s^{-1}] is key for A_n and thus we include values at 25°C

521 in Table S12.

522 Leaf-level A_n and r_{st} are calculated separately for sunlit vs. shaded leaves in M3Dry-psn. Sunlit and shaded portions of LAI

523 (LAI_{sun} and LAI_{shd}, respectively) follow Campbell and Norman (1998) and Song et al. (2009). Canopy scale r_{st} follows:

524 $r_{st} = \left(\left(\frac{LAI_{sun}}{r_{st,sun}} + \frac{LAI_{shd}}{r_{st,shd}} \right) f(w_2) \right)^{-1}$ (102)

525 Variables $r_{st,sun}$ and $r_{st,shd}$ are leaf-level stomatal resistances for sunlit and shaded leaves, respectively, calculated via Eq. (101).

526 The function $f(w_2)$ follows Eq. (90).

527 **2.1.7 CMAQ STAGE**
528 The Surface Tiled Aerosol and Gaseous Exchange (STAGE) parameterization is an option in CMAQ. Parameters in Table S13

529 are site-specific. If we reference Table S13, then the parameter's value is in Table S13.

530

531 $$v_d = f_{veg} \left(r_a + \cfrac{1}{r_{b,v} + \cfrac{1}{\cfrac{1}{r_{st} + r_m} + \cfrac{1}{r_{cut}}} + \cfrac{1}{r_{ac} + r_{b,g} + r_g}} \right)^{-1} + (1 - f_{veg})(r_a + r_{b,g} + r_g)^{-1} \quad (103)$$

532 CMAQ STAGE considers separate quasi-laminar boundary layer resistances around vegetation vs. the ground ($r_{b,v}$ and $r_{b,g}$,

533 respectively) (Table S3). The parameter f_{veg} is the vegetated fraction of the site; the M3Dry value is used (Table S12). Stomatal

534 resistance (r_{st}) follows Pleim and Ran (2011):

535 $$r_{st} = R_{diff,st} \frac{r_i}{LAI\, f(PAR)\, f(w_2)\, f(RH_l)\, f(T_a)} \quad (104)$$

536 The parameter r_i is initial resistance to stomatal uptake (Table S13). The functions follow M3Dry (Eqs. (89)-(92)).

537 Mesophyll resistance (r_m) follows Wesely (1989):

538 $$r_m = \left(\frac{H}{3000} + 100\, f_0 \right)^{-1} \quad (105)$$

539 Cuticular resistance (r_{cut}) follows:

540 $$r_{cut} = \left(LAI \left(\frac{f_{wet}}{1250} + \frac{1 - f_{wet}}{2000} \right) \right)^{-1} \quad (106)$$

541 The resistance to in-canopy turbulence (r_{ac}) is similar to Shuttleworth and Wallace (1985):

542 $$r_{ac} = \int_0^h \frac{dz}{K_t} \quad (107)$$

543 The variable K_t is in-canopy eddy diffusivity [m^2 s^{-1}]. By applying the drag coeffiecient ($C_d = \frac{u_*^2}{u^2}$), assuming a uniform vertical

544 distribution of leaves, and using an in-canopy attenuation coefficient of momentum following Yi (2008) [$\frac{LAI}{2}$]:

545 $$r_{ac} = Pr \frac{u}{u_*^2} \left(e^{\frac{LAI}{2}} - 1 \right) = r_a \left(e^{\frac{LAI}{2}} - 1 \right) \quad (108)$$

546 The variable u [m s^{-1}] is wind speed (Table 1).

547 The resistance to soil (r_g) changes whether soil is snow covered, dry or wet (wet is w_g greater than or equal to w_{sat} where w_{sat}

548 [m^3 m^{-3}] is soil water content at saturation (Table 1)). For dry ground, r_g follows Fares et al. (2004) and Fumagalli et al. (2016).

549 An asymptotic function bounds the resistance, following observations reported in Fumagalli et al. (2016):

550 $$r_g = \begin{cases} 250 + 2000\, \text{atan}\left(\cfrac{\left(\frac{w_g - w_{wlt}}{w_{fc}} \right)^B}{\pi} \right), w < w_{sat} \\ \cfrac{62500}{H\, R\, (T_g + 273.15)}, \; w \geq w_{sat} \\ \cfrac{1 - X_m}{r_{snow}} + \cfrac{X_m}{r_{sndiff} + \frac{62500}{H\, R\, (T_g + 273.15)}}, \; snow \end{cases} \quad (109)$$

551 The parameter R [L atm K^{-1} mol^{-1}] is the universal gas constant; B [unitless] is an empirical parameter related to soil moisture

552 (Table 1); r_{snow} is resistance to snow or ice [6667 s m^{-1}]; r_{sndiff} is resistance to diffusion through snowpack [10 s m^{-1}]. The

553 liquid fraction of the quasi-liquid layer in snow (X_m) is modeled as a system dominated by van der Walls forces using the

554 temperature parameterization following Huthwelker et al. (2006), and assuming a maximum of 20% to match gas-liquid

555 partitioning findings in Conklin et al. (1993):

556 $$X_m = \begin{cases} \dfrac{0.025}{(273.15-T_g)^{1/3}}, & 0.002 < 273.15 - T_g < 10 \\ 0.2, & 273.15 - T_g < 0.002 \end{cases} \quad (110)$$

557 **2.1.8 TEMIR**

558 The Terrestrial Ecosystem Model in R (TEMIR) provides two dry deposition schemes (Sun et al., 2022): Wesely and Zhang.

559 Wesely in TEMIR largely follows GEOS-Chem version 12.0.0, while Zhang follows Zhang et al. (2003). In both schemes, the

560 default stomatal resistance is highly empirical. TEMIR can also use two photosynthesis-based stomatal conductance models: the

561 Farquhar-Ball-Berry model (hereinafter, BB; Farquhar et al., 1980; Ball et al., 1987) and the Medlyn et al. (2011) model

562 (hereinafter, Medlyn). Thus, for TEMIR Wesely and Zhang, three stomatal conductance models are used each. We first describe

563 Wesely, then Zhang, and then photosynthesis-based approaches (hereinafter, psn). TEMIR Zhang parameters in Table S14 and

564 TEMIR psn parameters in Table S15 are site-specific. If we reference one of the tables, then the parameter's value is in the table.

565 For Wesely, surface resistance (r_c) follows:

566 $$r_c = \left(\frac{1}{r_{st}} + \frac{1}{r_{cut}} + \frac{1}{r_{dc} + r_{cl}} + \frac{1}{r_{ac} + r_g} \right)^{-1} \quad (111)$$

567 Stomatal resistance (r_{st}) follows Wang et al. (1998):

568 $$r_{st} = R_{diff,st} \frac{r_i}{LAI_{eff}\, f(T_a)} \quad (112)$$

569 The parameter r_i is initial resistance to stomatal uptake (same for GEOS-Chem Wesely; Table S6); LAI_{eff} [m^2 m^{-2}] is effective

570 LAI of actively transpiring leaves. The variable LAI_{eff} is calculated using function of LAI, θ, and cloud fraction. In GEOS-

571 Chem, if G is zero then LAI_{eff} equals 0.01. For the single-point model, we set G to be zero when θ is greater than 95° so that

572 nighttime r_{st} values in the single-point model more similar GEOS-Chem. GEOS-Chem almost never has non-zero G at night but

573 measured values are frequently small and non-zero. Here cloud fraction is assumed to be zero.

574 Effects of T_a follow:

575 $$f(T_a) = \begin{cases} 0.01, & T_a \leq 0 \\ T_a \frac{(40-T_a)}{400}, & 0 < T_a < 40 \\ 0.01, & 40 \leq T_a \end{cases} \quad (113)$$

576 Cuticular resistance (r_{cut}) follows:

577 $$r_{cut} = \begin{cases} r_{lu} \min\{2, e^{0.2(-1-T_a)}\} \left(\frac{H}{10^5} + f_0 \right)^{-1}, & T_a < -1 \\ \left(\frac{r_{lu}}{LAI} + 1000\, e^{-T_a - 4} \right) \left(\frac{H}{10^5} + f_0 \right)^{-1}, & T_a \geq -1 \end{cases} \quad (114)$$

578 The parameter r_{lu} is initial resistance for cuticular uptake. Values follow GEOS-Chem Wesely (Table S6).

579 The resistance associated with in-canopy convection (r_{dc}) follows:

580 $$r_{dc} = 100 \left(1 + \frac{1000}{G+10} \right) \quad (115)$$

581 The resistance to the lower canopy (r_{cl}) follows:

582 $\quad r_{cl} = \left(\frac{H}{10^5 r_{cl,S}} + \frac{f_0}{r_{cl,O}}\right)^{-1}$ (116)

583 Parameters $r_{cl,S}$ and $r_{cl,O}$ are initial resistances to uptake to the lower canopy and follow GEOS-Chem Wesely (Table S6).

584 Resistance to soil (r_g) follows:

585 $\quad r_g = \left(\frac{H}{10^5 r_{g,S}} + \frac{f_0}{r_{g,O}}\right)^{-1}$ (117)

586 Parameters $r_{g,S}$ and $r_{g,O}$ are initial resistances to soil and follow GEOS-Chem Wesely (Table S6). The resistance to turbulent

587 transport to the ground (r_{ac}) follows GEOS-Chem Wesely (Table S6).

588 The changes in resistances when there is snow follow GEOS-Chem Wesely (Table S6).

589 For Zhang, surface resistance (r_c) follows:

590 $\quad r_c = \left(\frac{1-W_{st}}{r_{st}} + \frac{1}{r_{cut}} + \frac{1}{r_{ac}+r_g}\right)^{-1}$ (118)

591 The variable W_{st} [fractional] is used to account for leaf wetness. If P is greater than 0.2 mm hr^{-1} then:

592 $\quad W_{st} = \begin{cases} 0, & G \leq 200 \\ \frac{G-200}{800}, & 200 \leq G \leq 600 \\ 0.5, & G > 600 \end{cases}$ (119)

593 Stomatal resistance (r_{st}) follows:

594 $\quad r_{st} = R_{diff,st}\, \frac{r_i(LAI,PAR)}{f(T_a)\,f(VPD)\,f(\psi_{leaf})}$ (120)

595 Dependencies on T_a, VPD, and ψ_{leaf} are as described in Brook et al. (1999).

596 The variable $r_i(LAI,PAR)$ follows:

597 $\quad r_i(LAI,PAR) = \left(\frac{LAI_{sun}}{r_i\left(1+\frac{b_{rs}}{PAR_{sun}}\right)} + \frac{LAI_{shd}}{r_i\left(1+\frac{b_{rs}}{PAR_{shd}}\right)}\right)^{-1}$ (121)

598 The parameter r_i is initial resistance to stomatal uptake (Table S14); b_{rs} [W m^{-2}] is empirical (Table S14); LAI_{sun} and LAI_{shd}

599 [m^2 m^{-2}] are sunlit and shaded LAI:

600 $\quad LAI_{sun} = \frac{1-e^{-K_b\,LAI}}{K_b}$ (122)

601 $\quad LAI_{shd} = LAI - LAI_{sun}$ (123)

602 The variable K_b is canopy light extinction coefficient [unitless]:

603 $\quad K_b = \frac{0.5}{\cos\left(\frac{\pi}{180}\theta\right)}$ (124)

604 The variables PAR_{sun} and PAR_{shd} [W m^{-2}] are PAR reaching sunlit and shaded leaves:

605 $\quad PAR_{shd} = R_{diff}\, e^{-0.5\,LAI^a} + 0.07\,R_{dir}\,(1.1 - 0.1\,LAI)\,e^{-\cos\left(\frac{\pi}{180}\theta\right)}$ (125)

606 $\quad PAR_{sun} = PAR_{shd} + \frac{R_{dir}^b\,\cos\left(\frac{\pi}{180}\alpha\right)}{\cos\left(\frac{\pi}{180}\theta\right)}$ (126)

607   The parameter α is the angle between the leaf and the sun [60º]; R_{diff} and R_{dir} are downward visible radiation fluxes from

608   diffuse and direct-beam radiation above the canopy. Here we use diffuse fraction from the reanalysis product Modern-Era

609   Retrospective analysis for Research and Applications, Version 2 (MERRA-2) (GMAO, 2015) to separate R_{diff} and R_{dir} from

610   observed PAR. If LAI is less than 2.5 m² m⁻² or G is less than 200 W m⁻² then a equals 0.7 and b equals 1. Otherwise, a equals

611   0.8 and b equals 0.8.

612   Effects of T_a follow:

613    $f(T_a) = \left(\frac{T_a - T_{min}}{T_{opt} - T_{min}}\right)\left(\frac{T_{max} - T_a}{T_{max} - T_{opt}}\right)^{\frac{T_{max} - T_{opt}}{T_{opt} - T_{min}}}$ (127)

614   Parameters T_{min}, T_{max}, and T_{opt} [ºC] are minimum, maximum, and optimum temperature, respectively (Table S14).

615   Effects of VPD follow:

616    $f(VPD) = 1 - b_{VPD}\, VPD$ (128)

617   The parameter b_{VPD} [kPa⁻¹] is empirical (Table S14).

618   Effects of ψ_{leaf} follow:

619    $f(\psi_{leaf}) = \frac{\psi_{leaf} - \psi_{leaf,2}}{\psi_{leaf,1} - \psi_{leaf,2}}$ (129)

620   Parameters $\psi_{leaf,1}$ and $\psi_{leaf,2}$ [MPa] are empirical (Table S14); ψ_{leaf} is parameterized as:

621    $\psi_{leaf} = -0.72 - 0.0013\, G$ (130)

622   Cuticular resistance (r_{cut}) follows:

623    $r_{cut} = \begin{cases} \frac{c_{cut,dry}}{u^* LAI^{0.25}\, e^{3\,RH}}, dry \\ \frac{c_{cut,wet}}{u^* LAI^{0.5}}, wet \end{cases}$ (131)

624   Parameters $c_{cut,dry}$ and $c_{cut,wet}$ [unitless] are empirical coefficients related to dry and wet cuticular uptake (Table S14). If P is

625   greater than 0.2 mm hr⁻¹ then cuticles are wet; otherwise, cuticles are dry.

626   The variable r_{cut} is adjusted for snow:

627    $r_{cut} = \left(\frac{1 - f_{snow}}{r_{cut}} + \frac{2 f_{snow}}{2000}\right)^{-1}$ (132)

628   In-canopy aerodynamic resistance (r_{ac}) follows:

629    $r_{ac} = r_{ac0} \frac{LAI^{0.25}}{(u^*)^2}$ (133)

630   The variable r_{ac0} follows:

631    $r_{ac0} = r_{ac0,min} + \frac{LAI - LAI_{min}}{LAI_{max} - LAI_{min}}\left(r_{ac0,max} - r_{ac0,min}\right)$ (134)

632   Variables LAI_{min} and LAI_{max} [m² m⁻²] are minimum and maximum observed LAI during a specific year; $r_{ac0,min}$ and $r_{ac0,max}$

633   are initial resistances (Table S14).

634   Resistance to soil (r_g) follows:

635    $r_g = \left(\frac{1 - \min\{1, 2 f_{snow}\}}{200} + \frac{\min\{1, 2 f_{snow}\}}{2000}\right)^{-1}$ (135)

636   The variable f_{snow} is the fraction of the surface covered by snow [unitless]:

637     $f_{snow} = \min\left\{1, \frac{SD}{SD_{max}}\right\}$ (136)

638   The parameter SD_{max} is maximum snow depth [cm] (Table S14).

639

640   We now discuss psn options for TEMIR Wesely and TEMIR Zhang. For BB (Ball et al., 1987; Farquhar et al., 1980; von

641   Caemmerer and Farquhar, 1981; Collatz et al., 1991, 1992),

642     $r_{st} = \left(\beta_t\, g_0 + g_1 \frac{A_n\, RH}{\frac{p_{CO_2,l}}{p_a}} \right)^{-1} \frac{p_a}{R\, \theta_a}$ (137)

643   The parameter g_0 equals 0.01 mol m^{-2} s^{-1}; g_1 equals 9; A_n is net photosynthesis [mol m^{-2} s^{-1}]; β_t is a soil water stress factor

644   [unitless]; $p_{CO_2,l}$ is carbon dioxide partial pressure at leaf surface [Pa]; R is the universal gas constant [J mol^{-1} K^{-1}]; θ_a is

645   potential air temperature [K].

646   For Medlyn (Medlyn et al., 2011),

647     $r_{st} = \left(\beta_t\, g_0 + \frac{D_w}{D_{CO_2}} \left(1 + \frac{g_{1M}}{\sqrt{VPD}}\right) \frac{A_n}{\frac{p_{CO_2,l}}{p_a}} \right)^{-1} \frac{p_a}{R\, \theta_a}$ (138)

648   The parameter g_{1M} [kPa$^{0.5}$] is empirical (Table S15); g_0 equals 0.0001 mol m^{-2} s^{-1}; D_w [m^2 s^{-1}] is the diffusivity of water vapor

649   in air (Table 1); the ratio of diffusivities is 1.6.

650   A single-layer bulk soil formulation considering the root zone (0-100 cm) is used to calculate β_t:

651     $\beta_t = \begin{cases} 1, & \psi_{soil} > \psi_{soil,fc} \\ \frac{\psi_{soil,wlt} - \psi_{soil}}{\psi_{soil,wlt} - \psi_{soil,fc}}, & \psi_{soil,wlt} \le \psi_{soil} \le \psi_{soil,fc} \\ 0, & \psi_{soil} < \psi_{soil,fc} \end{cases}$ (139)

652   The variable ψ_{soil} [kPa] is soil matric potential (Table 1):

653     $\psi_{soil} = \psi_{soil,sat}\, w_2^{-B}$ (140)

654

655   For both Medlyn and BB, leaf-level r_{st} is calculated individually for sunlit and shaded leaves, and then scaled up:

656     $r_{st} = R_{diff,st} \left(\frac{LAI_{sun}}{r_{b,leaf} + r_{st,sun}} + \frac{LAI_{shd}}{r_{b,leaf} + r_{st,shd}} \right)^{-1}$ (141)

657   Variables $r_{st,sun}$ and $r_{st,shd}$ are leaf-level stomatal resistances for sunlit and shaded leaves, respectively; LAI_{sun} and LAI_{shd} are

658   sunlit and shaded LAI, respectively; $r_{b,leaf}$ is leaf boundary layer resistance:

659     $r_{b,leaf} = \frac{1}{c_v} \sqrt{\frac{u_*}{l}}$ (142)

660   The parameter c_v [0.01 m s$^{-0.5}$] is the turbulent transfer coefficient; l [0.04 m] is the characteristic dimension of leaves.

661   Variables LAI_{sun} and LAI_{shd} follow:

662     $LAI_{sun} = PAI_{sun} \frac{LAI}{LAI + SAI}$ (143)

663    $LAI_{shd} = PAI_{shd} \frac{LAI}{LAI+SAI}$ (144)

664   The variable SAI [m² m⁻²] is stem area index; PAI_{sun} and PAI_{shd} [m² m⁻²] are sunlit and shaded plant area index, respectively:

665    $PAI_{sun} = \frac{1-e^{-K_b(LAI+SAI)}}{K_b}$ (145)

666    $PAI_{shd} = LAI + SAI - PAI_{sun}$ (146)

667   The variable SAI follows Zeng et al. (2002):

668    $SAI_n = \max\{0.5\, SAI_{n-1} + \max\{LAI_{n-1} - LAI_n, 0\}, 1\}$ (147)

669   The parameter n is nth month of the year.

670   Leaf-level photosynthesis of C₃ plants is represented by the formulation that relates to Michaelis–Menten enzyme kinetics and

671   photosynthetic biochemical pathways, as in Community Land Model 4.5 (CLM4.5) (Oleson et al., 2013) and following Collatz et

672   al. (1992):

673    $A_n = \min\{A_c, A_j, A_p\} - R_d$ (148)

674   The Rubisco-limited photosynthetic rate (A_c) [mol m⁻² s⁻¹] follows:

675    $A_c = V_{cmax} \frac{c_i - \Gamma_*}{c_i + K_c \left(1 + \frac{o_i}{K_o}\right)}$ (149)

676   The variable c_i is intercellular carbon dioxide partial pressure [Pa]; K_c and K_o are Michaelis–Menten constants for carboxylation

677   and oxygenation [Pa]; o_i is intercellular oxygen partial pressure [0.029 p_a Pa]; Γ_* is carbon dioxide compensation point [Pa];

678   V_{cmax} is maximum rate of carboxylation [mol m⁻² s⁻¹] adjusted for leaf temperature:

679    $V_{cmax} = V_{cmax,25}\, f(T_l)\, f_H(T_l)\, \beta_t$ (150)

680   The parameter $V_{cmax,25}$ is the value of V_{cmax} at 25ºC (Table S15).

681   The function of leaf temperature (T_l) [K] follows:

682    $f(T_l) = e^{\frac{\Delta H_a}{298.15 * 0.001R}\left(1 - \frac{298.15}{T_l}\right)}$ (151)

683   The parameter R is the universal gas constant [J kg⁻¹ K⁻¹]. The high temperature function of T_l follows:

684    $f_H(T_l) = \frac{1 + e^{\frac{298.15\,\Delta S - \Delta H_d}{298.15 * 0.001\,R}}}{1 + e^{\frac{\Delta S T_v - \Delta H_d}{0.001\,R\,T_l}}}$ (152)

685   The variables ΔH_a [J mol⁻¹], ΔS [J mol⁻¹ K⁻¹], and ΔH_d [J mol⁻¹] are temperature dependent and follow definitions in CLM4.5

686   (see Table S15 for the CLM4.5 PFTs for each site).

687   The ribulose-1,5-bisphosphate (RuBP)-limited photosynthetic rate (A_j) [mol m⁻² s⁻¹] follows:

688    $A_j = \frac{J}{4} \frac{c_i - \Gamma_*}{c_i + 2\Gamma_*}$ (153)

689   The parameter J is the electron transport rate [mol m⁻² s⁻¹], taken as the smaller of the two roots of the equation below:

690    $\theta_{PSII} J^2 - (I_{PSII} + J_{max}) J + I_{PSII} J_{max} = 0$ (154)

691    $J_{max} = 1.97\, V_{cmax,25}\, f(T_l)\, f_H(T_l)$ (155)

692    $I_{PSII} = 0.5\, \Phi_{PSII}\, 4.6\, x\, 10^{-6}\, \phi$ (156)

693   The parameter θ_{PSII} [unitless] represents curvature; I_{PSII} [mol m^{-2} s^{-1}] is light utilization in electron transport by photosystem II;

694   J_{max} [mol m^{-2} s^{-1}] is potential maximum electron transport rate; Φ_{PSII} [unitless] is quantum yield of photosystem II; ϕ [W m^{-2}]

695   is photosynthetically active radiation absorbed by leaves, converted to photosynthetic photon flux density with 4.6 x 10^{-6} mol J^{-1}.

696   The product-limited photosynthetic rate (A_p) [mol m^{-2} s^{-1}] follows:

697    $A_p = 3\, T_p$ (157)

698   The parameter T_p is the triose phosphate utilization rate [mol m^{-2} s^{-1}].

699    $T_p = 0.167\, V_{cmax,25}\, f(T_l)\, f_H(T_l)$ (158)

700   Dark respiration (R_d) [mol m^{-2} s^{-1}] follows:

701    $R_d = 0.015\, V_{cmax,25}\, f(T_l)\, f_H(T_l)\, \beta_t$ (159)

702   Calculation for A_n and r_{st} involves a coupled set of equations that are solved iteratively at each time step until c_i converges (see

703   Sect. 8.5 of Oleson et al., 2013):

704    $A_n = \dfrac{p_{CO_2,a} - p_{CO_2,i}}{\left(1.4\, r_{b,leaf} + \frac{D_w}{D_{CO_2}} r_{st}\right) p_a} = \dfrac{p_{CO_2,a} - p_{CO_2,l}}{1.4\, r_{b,leaf}\, p_a} = \dfrac{p_{CO_2,l} - p_{CO_2,i}}{\frac{D_w}{D_{CO_2}} r_{st}\, p_a}$ (160)

705   Variables $p_{CO_2,a}$ and $p_{CO_2,i}$ are carbon dioxide partial pressure [Pa] in air and intercellular space, respectively.

706   **2.1.9 DO$_3$SE**
707   DO$_3$SE as described below is consistent with the parameterization in the EMEP model (Simpson et al., 2012). DO$_3$SE uses two

708   methods to estimate r_{st}: the multiplicative method based on Jarvis (1976) ("DO$_3$SE multi") and the coupled photosynthesis-

709   stomatal conductance method based on Leuning (1995) ("DO$_3$SE psn"). First, we describe components that are the same between

710   DO$_3$SE multi and DO$_3$SE psn. Second, we describe the components unique to DO$_3$SE multi and then to DO$_3$SE psn. Parameters

711   in Table S16 are site-specific. If we reference Table S16, then the parameter's value is in the table.

712   Surface resistance (r_c) follows:

713    $r_c = \left(\dfrac{LAI}{r_{st}} + \dfrac{StAI}{r_{cut}} + \dfrac{1}{r_{ac} + r_g}\right)^{-1}$ (161)

714   The parameter r_{cut} is resistance to cuticular uptake [2500 s m^{-1}]; $StAI$ is the stand area index [m^2 m^{-2}].

715   For forests,

716    $StAI = LAI + 1$ (162)

717   For the other LULC types examined here,

718    $StAI = LAI$ (163)

719   The resistance to in-canopy turbulence (r_{ac}) follows Erisman et al. (1994):

720    $r_{ac} = 14 \dfrac{h\, StAI}{u_*}$ (164)

721   Resistance to soil (r_g) follows:

722    $r_g = 200 + 1000\, e^{-T_a - 4} + 2000\, \delta_{snow}$ (165)

723   The parameter δ_{snow} equals 1 when snow is present and 0 when snow is absent.

724   For DO₃SE multi, according to Simpson et al. (2012), stomatal resistance (r_{st}) follows:

725   $r_{st} = \left(g_{max} \max\{f_{min}, f(T_a)\, f(VPD)\, f(w_2)\}\, a_{phen}\, a_{light} \right)^{-1}$ (166)

726   The parameter g_{max} is maximum stomatal conductance [m s⁻¹] (Table S16); f_{min} is the minimum factor [unitless] (Table S16).

727   Effects of T_a follow:

728   $f(T_a) = \frac{T_a - T_{min}}{T_{opt} - T_{min}} \left(\frac{T_{max} - T_a}{T_{max} - T_{opt}} \right)^{\frac{T_{max} - T_{opt}}{T_{opt} - T_{min}}}$ (167)

729   The function $f(T_a)$ equals 0.01 when T_a is outside T_{min} to T_{max}; T_{min}, T_{max}, and T_{opt} [ºC] are minimum, maximum, and

730   optimum temperature, respectively (Table S16).

731   Effects of VPD follow:

732   $f(VPD) = \min\{1, \max\{f_{min}, f_{min} + (1 - f_{min})\frac{VPD_{min} - VPD}{VPD_{min} - VPD_{max}}\}$ (168)

733   Parameters VPD_{min} and VPD_{max} [kPa] are minimum and maximum VPD, respectively (Table S16).

734   Effects of w_2 follow:

735   $f(w_2) = \min\{1, \max\{f_{min}, f_{min} + (1 - f_{min})\frac{w_{wlt} - w_2}{w_{max} - 0.5\,(w_{fc} - w_{wlt})}\}$ (169)

736   The variable a_{phen} follows:

737   $a_{phen} = \begin{cases} 0, d_y \leq d_{SGS}\ or\ d_y > d_{EGS} \\ \emptyset_a + \left(\frac{d_y - d_{SGS}}{(d_{SGS} + \emptyset_d) - d_{SGS}}\right)(\emptyset_b - \emptyset_a), d_{SGS} \leq d_y < d_{SGS} + \emptyset_d \\ \emptyset_b, d_{SGS} + \emptyset_d < d_y \leq d_{EGS} - \emptyset_e \\ \emptyset_b - \left(\frac{d_y - (d_{EGS} - \emptyset_e)}{d_{EGS} - \emptyset_e}\right)(\emptyset_b - \emptyset_c), d_{EGS} - \emptyset_e < d_y \leq d_{EGS} \end{cases}$ (170)

738   The variable d_y is the day of the year; d_{SGS} is day of the year that corresponds to the start of the growing season; d_{EGS} is the day

739   of the year that corresponds to the end of the growing season. For forests, d_{SGS} and d_{EGS} are estimated whereby d_{SGS} equals 105

740   at 50ºN and alters by 1.5 day per degree latitude earlier on moving south and later on moving north, and d_{EGS} equals 297 at 50ºN

741   and alters by 2 days per degree latitude earlier on moving north and later on moving south. The values of $\emptyset_a$, $\emptyset_b$, $\emptyset_c$, $\emptyset_d$, and $\emptyset_e$

742   are given in Table S16. For other LULC, we assume a year-long growing season.

743   The variable a_{light} follows:

744   $a_{light} = \frac{LAI_{sun}}{LAI}\left(1 - e^{-\alpha\, I_{PAR}^{sun}}\right) + \frac{LAI_{shd}}{LAI}\left(1 - e^{-\alpha\, I_{PAR}^{shd}}\right)$ (171)

745   The parameter α is empirical (Table S16); sunlit and shaded portions of LAI (LAI_{sun} and LAI_{shd}, respectively) follow Norman

746   (1979, 1982):

747   $LAI_{sun} = \left(1 - e^{-0.5\frac{LAI}{\cos\theta}}\right) 2\cos\theta$ (172)

748   $LAI_{shd} = LAI - LAI_{sun}$ (173)

749   The variables I_{PAR}^{sun} and I_{PAR}^{shade} [W m⁻²] follow:

750   $I_{PAR}^{shd} = I_{diff}e^{-0.5\,LAI^{0.7}} + 0.07\,I_{dir}(1.1 - 0.1\,LAI)\,e^{-\cos\theta}$ (174)

751 $I_{PAR}^{sun} = \frac{I_{dir} \cos \alpha_1}{\cos \theta} + I_{PAR}^{shd}$ (175)

752 The parameter α_1 is the average inclination of leaves [°60]; I_{diff} and I_{dir} are diffuse and direct radiation [W m^{-2}] estimated as a

753 function of the potential to actual PAR. Potential PAR is estimated using standard solar geometry methods assuming no cloud

754 cover and a sky transmissivity of 0.9.

755

756 For DO$_3$SE psn (Leuning, 1990; 1995), which requires an estimate of net photosynthesis (A_n) [mol CO$_2$ m^{-2} s^{-1}] (Farquhar et al.,

757 1980), stomatal resistance (r_{st}) follows:

758 $r_{st} = \left(g_0 + g_1 \frac{A_n}{([CO_2]_l - \Gamma_*)\left(1 + \left(\frac{VPD}{D_0}\right)^8\right)} \right)^{-1} \frac{D_{CO_2}}{D_{O_3}} \frac{1000.0 \, \rho}{M_{air}}$ (176)

759 The parameter g_0 is minimum conductance [mol air m^{-2} s^{-1}] (Leuning, 1990); g_1 is empirical [unitless]; D_0 is a parameter related

760 to VPD [kPa] (Leuning et al., 1998) (Table S16); $[CO_2]_l$ is the leaf surface carbon dioxide mixing ratio [mol CO$_2$ mol air^{-1}]; Γ_* is

761 carbon dioxide compensation point [mol CO$_2$ mol air^{-1}]. We assume the diffusivity ratio is 0.96. The variable $[CO_2]_l$ is

762 calculated from $[CO_2]$ and leaf boundary layer resistance ($r_{b,leaf}$):

763 $r_{b,leaf} = 186 \sqrt{\frac{u}{l}}$ (177)

764 The parameter l is the characteristic dimension of leaves [m].

765 The variable A_n follows Sharkey et al. (2007):

766 $A_n = \min\{A_c, A_j, A_p\} - R_d$ (178)

767 The parameter R_d is dark respiration [0.015 x 10^{-6} mol m^{-2} s^{-1}].

768 The Rubisco-limited rate (A_c) [mol m^{-2} s^{-1}] follows:

769 $A_c = a_{phen} \, f(w_2) \, V_{cmax,25} \frac{[CO_2]_i - \Gamma_*}{[CO_2]_i + K_c\left(1 + \frac{o_i}{K_o}\right)}$ (179)

770 The variable c_i is intercellular carbon dioxide partial pressure [Pa]; K_c and K_o are Michaelis–Menten constants for carboxylation

771 and oxygenation [Pa]; o_i is intercellular oxygen partial pressure [Pa]; Γ_* is CO$_2$ compensation point [Pa]; $V_{cmax,25}$ is maximum

772 rate of carboxylation at 25°C [mol m^{-2} s^{-1}] (Table S16); a_{phen} follows Eq. (170); $f(w_2)$ follows Eq. (169).

773 The ribulose-1,5-bisphosphate (RuBP)-limited rate (A_j) [mol m^{-2} s^{-1}] follows:

774 $A_j = J \frac{c_i - \Gamma_*}{a \, c_i + b \, \Gamma_*}$ (180)

775 The variable J is electron transport rate [mol m^{-2} s^{-1}]; a and b denote electron requirements for formation of NADPH and ATP,

776 respectively. We use a equals 4 and b equals 8 (Sharkey et al., 2007).

777 The product-limited photosynthetic rate (A_p) [mol m^{-2} s^{-1}] follows:

778 $A_p = 0.5 \, V_{cmax,25}$ (181)

779   **2.1.10 MLC-CHEM**

780   The Multi-layer Canopy and Chemistry Exchange Model (MLC-CHEM) has been applied to evaluate the role of in-canopy

781   interactions on atmosphere-biosphere exchanges and atmospheric composition at field sites (e.g., Visser et al., 2021) and the

782   global scale (e.g., Ganzeveld et al., 2010). MLC-CHEM requires a minimum h of 0.5 m so has not been configured for all sites.

783   The canopy environment is represented by an understory and crown layer. However, radiation dependent processes such as

784   biogenic emissions, photolysis, and stomatal conductance are estimated at four canopy layers to consider observed large gradients in in-

785   canopy radiation as a function of the vertical distribution of biomass. For the single-point model, ~75% and ~25% of the total LAI is

786   present in the crown layer and understory, respectively. These canopy structure settings are used to calculate in-canopy profiles of direct

787   and diffusive radiation as well as the fraction of sunlit leaves from the surface incoming solar radiation (Norman, 1979). Simulated

788   radiation-dependent processes for the four layers are then scaled-up to two layers for in-canopy and canopy-top fluxes and

789   concentrations using the vertical LAI distribution.

790   MLC-CHEM diagnoses canopy-scale v_d from simulated canopy-top ozone fluxes divided by $[O_3]$, which is ambient ozone

791   mixing ratio at z_r [ppbv] (Table 1). Turbulent exchanges of ozone between the crown layer and understory and between the

792   surface and crown layer are calculated from assumed linear $[O_3]$ gradients between heights, and eddy diffusivities. The eddy

793   diffusivity ($K_{sl \to cl}$) [m^2 s^{-1}] follows (Ganzeveld and Lelieveld, 1995):

794    $$K_{sl \to cl} = \frac{(z_{sl} - z_{cl})}{r_a} \quad (182)$$

795   The eddy diffusivity between the crown layer and understory ($K_{cl \to us}$) [m^2 s^{-1}] follows:

796    $$K_{cl \to us} = K_{sl \to cl} \frac{u_{cl \to us}}{u} \quad (183)$$

797   The variable $u_{cl \to us}$ is wind speed at the crown layer-understory interface [m s^{-1}] calculated as a function of u and canopy

798   structure (Cionco, 1978).

799   Resistance to leaf-level uptake per layer ($r_{l,layer}$) follows:

800    $$r_{l,layer} = \frac{r_{b,leaf} + \left(\frac{1}{r_{st}} + \frac{1}{r_{cut}}\right)^{-1}}{\max\{LAI_{layer}, 10^{-5}\}} (184)$$

801   Leaf-level stomatal resistance (r_{st}) is calculated using a photosynthesis-stomatal conductance model (Ronda et al., 2001):

802    $$r_{st} = f(w_2) \, R_{diff,st} \left(\frac{D_w}{D_{CO_2}} \left(g_0 + g_1 \frac{A_n}{([CO_2] - \Gamma_*)\left(1 + 8.09 \frac{VPD}{D_0}\right)} \frac{M_{air}}{1000 \, \rho} \right) \right)^{-1} (185)$$

803   The ratio of diffusivities of water vapor to carbon dioxide is 1.6; g_0 is set to 0.025 x 10^{-3} m s^{-1} (Leuning, 1990); g_1 is set to 9.09;

804   A_n is net photosynthesis [μmol CO$_2$ m^{-2} s^{-1}], calculated as a function of G, leaf temperature, $[CO_2]$, and soil moisture (Ronda et

805   al., 2001); Γ_* is CO$_2$ compensation point [45 ppmv]; D_0 [kPa] is VPD at which stomata close (this term is calculated each

806   timestep from vegetation-specific constants; Ronda et al., 2001). The soil moisture effect follows:

807    $$f(w_2) = 2 \max\{\min\left\{10^{-3}, \frac{w_s - w_{wlt}}{0.75 w_{fc} - w_{wlt}}\right\}, 1\} - \left(\max\{\min\left\{10^{-3}, \frac{w_s - w_{wlt}}{0.75 \, w_{fc} - w_{wlt}}\right\}, 1\}\right)^2 (186)$$

808   Leaf-level cuticular resistance (r_{cut}) follows (Wesely, 1989; Ganzeveld and Lelieveld, 1995; Ganzeveld et al., 1998):

809    $r_{cut} = \left(\frac{1-f_{wet}}{5 \times 10^5} + \frac{f_{wet}}{1000} \right)^{-1}$ (187)

810   In-canopy aerodynamic resistance (r_{ac}) considers turbulent transport through the understory to the ground:

811    $r_{ac} = 14 \frac{0.25\,h\,LAI}{u^*}$ (188)

812   To estimate dry deposition to the ground, r_{ac} is added in series with r_g, resistance to soil [400 s m^{-1}] (Wesely, 1989; Ganzeveld and

813   Lelieveld, 1995; Ganzeveld et al., 1998). If there is snow, then r_g is 2000 s m^{-1}. Resistances are combined with the lower most

814   understory leaf resistance ($r_{l,layer,1}$) to create a lower most understory canopy resistance ($r_{c,layer,1}$):

815    $r_{c,layer,1} = \left(\frac{1}{r_{l,layer,1}} + \frac{1}{r_{ac} + r_g} \right)^{-1}$ (189)

816   In contrast to big-leaf schemes, effective conductances for MLC-CHEM do not add up exactly to v_d because there is an in-

817   canopy [O_3] gradient due to sources and sinks and transport.

818   **3 Measurements for driving and evaluating single-point models**

819   **3.1 Turbulent fluxes of ozone**

820   Our best observational constraints on dry deposition are vertical turbulent fluxes, but fluxes integrate the influence of many

821   processes and are not necessarily only reflective of dry deposition. For example, ambient chemical loss of ozone can influence

822   ozone fluxes when the chemistry occurs on the timescale of turbulence. Relevant reactions for ozone fluxes are ozone reacting

823   with highly reactive biogenic volatile organic compounds (BVOCs) or nitrogen oxide (NO). When there are no other sources and

824   sinks aside from dry deposition below the measurement height, dividing the observed turbulent flux by ambient concentration at

825   the same height can give a measure of efficiency of dry deposition ('the deposition velocity'). While fluxes provide key

826   constraints on the amount of gas removed by the surface, deposition velocities aid in building predictive ability given that they

827   indicate how the strength of the removal changes with meteorology and environmental conditions. Turbulent fluxes are mostly

828   measured at individual sites, representing the 'ecosystem' scale where the measurement footprint typically extends from the

829   order of 100 m to 1 km. Turbulent fluxes can also be measured from airplanes (e.g., Lenschow et al., 1981; Godowitch, 1990;

830   Mahrt et al., 1995; Wolfe et al., 2015). Turbulent flux observations typically record changes on hourly or half hourly timescales,

831   which is important because there is strong sub-daily variability in dry deposition.

832

833   Here we leverage existing long-term and short-term ozone flux datasets over a variety of LULC types to develop current

834   understanding of model performance and the spread across current dry deposition parameterizations. Strong observed interannual

835   variability in ozone deposition velocities (Rannik et al., 2012; Clifton et al., 2017; Gerosa et al., 2022), as well as development of

836   dry deposition schemes based on short-term data (e.g., days to months), motivates our multiyear evaluation approach. Although

837   our evaluation effort would ideally include fluxes of many reactive gases (as well as aerosols), there are not long-term flux

838   measurements of most compounds for which the fluxes primarily represent dry deposition. Generally, flux observations of dry

839   depositing air pollutants and their precursors are oftentimes few and far between and/or challenging to access (Guenther et al.,

840   2011; Fares et al., 2017; Clifton et al., 2020a; Farmer et al., 2021; He et al., 2021). A key reason is that obtaining high-frequency

841   concentration measurements of some compounds can be challenging. Ozone fluxes are the most measured fluxes of any dry

842   depositing reactive gas, and they can be measured over seasonal to multiyear timescales. While the model evaluation component

843   of Activity 2 is only for ozone, the model comparison can be performed for other gases.

844

845   Ozone fluxes are measured either via eddy covariance or the gradient method. Eddy covariance is the most fundamental and

846   direct method for measuring turbulent exchange (e.g., Hicks et al., 1989; Dabberdt et al., 1993). Eddy covariance fluxes require

847   concentration analyzers with high measurement frequency to capture the transport of material via turbulent eddies. While fast

848   analyzers are available for ozone, they are resource intensive to operate. Gradient techniques are more practical because slow

849   analyzers can be used. However, gradient techniques assume transport only occurs down the local mean concentration gradient

850   while in reality organized turbulent motions can transport material up-gradient (e.g., Raupach, 1979; Gao et al., 1989; Collineau

851   and Brunet, 1993; Thomas and Foken, 2007; Steiner et al., 2011; Patton and Finnigan, 2013). We use some gradient ozone flux

852   datasets, but caution that they may be particularly uncertain, especially for tall vegetation.

853   **3.2 Site-specific datasets**

854   We simulate ozone deposition velocities by driving single-point models with site-level meteorological and environmental

855   variables measured or inferred from measurements at eight sites with ozone flux measurements. Table 2 summarizes site

856   locations, LULC types, vegetation composition, and soil types. The set of sites represents a variety of LULC types and climates.

857   The sites include deciduous, evergreen, and mixed forests, shrubs, grasses, and a peat bog. Climate types include Mediterranean,

858   temperate, and boreal, as well as maritime and continental. Dry deposition parameterizations strongly rely on the concept that

859   key processes and parameters are specific to LULC type. While we examine several LULC types here, we note that our

860   measurement testbed is likely insufficient to generalize the results of our study to specific LULC types, and thus we focus our

861   discussion on individual sites.

862

863   Table S17 summarizes details about ozone flux measurements, time periods examined, and post-processing of data. Five of eight

864   sites selected have at least three and up to twelve years of ozone flux data. The rest have fewer than three years of ozone flux

865   data (Auchencorth Moss, Bugacpuszta, Ramat Hanadiv) but were included to diversify climate and LULC types examined. The

866   eddy covariance technique is used for Auchencorth Moss, Bugacpuszta, Harvard Forest, Hyytiälä, Ispra, and Ramat Hanadiv.

867   The gradient technique is used for Borden Forest and Easter Bush.

868

869   The gradient technique used at Borden Forest is described in Wu et al. (2015, 2016) and was developed for Harvard Forest by

870   comparing gradient and eddy covariance fluxes. Wu et al. (2015) shows that the gradient technique used at Borden Forest

871   strongly overestimates ozone deposition velocities at night and during winter at Harvard Forest, as compared to eddy covariance.

872   Wu et al. (2015) also show that parameter choice can strongly influence deposition velocities inferred from the gradient

873   technique. Thus, seasonal and diel cycle amplitudes as well as the magnitude of observed ozone deposition velocities at Borden

874   Forest are uncertain.

875   **Table 2: Summary of ozone flux tower sites.**

Site	Location	Land use/land cover Type	More complete description of vegetation	Soil properties
Auchencorth Moss, Scotland	55.79ºN, 3.24ºW	Peat bog	Covered with heather, moss, and grass; vegetation primarily *Calluna vulgaris*, *Juncus effusus*, grassy hummocks, and hollows; drained and cut over 100 years ago but rewetted over many decades (Leith et al., 2014); low intensity grazing by sheep	85% Histosols
Borden Forest, Canada	44.32ºN, 79.93ºW	Temperate mixed forest	Boreal-temperate transition forest with mostly *Acer rubrum L.* but also *Pinus strobes L.*, *Populus grandidentata Michx.*, *Fraxinus americana L.,* and *Fagus grandifolia*; regrowing on farmland abandoned about a century ago (Froelich et al., 2015; Wu et al., 2016)	Tioga sand/sandy loam
Bugacpuszta, Hungary	46.69ºN, 19.60ºE	Grass	Semi-natural and semi-arid; primarily *Festuca pseudovina*, *Carex stenophylla*, and *Cynodon dactylon* (Koncz et al., 2014); grazing during most of the year (Machon et al., 2015)	Chernozem with 79% sand and 13% clay in upper soil layer (10 cm) (Horváth et al., 2018)
Easter Bush, Scotland	55.87ºN, 03.03ºW	Grass	On the boundary between two fields that have been managed for silage harvest and intensive grazing by sheep and cattle (Coyle, 2006); greater than 90% *Lolium perenne* (Coyle, 2006; Jones et al., 2017)	Imperfectly drained Macmerry with Rowanhill soil association (Eutric Cambisol) and with 20-26% clay (Jones et al., 2017)
Ispra, Italy	45.81°N, 8.63°E	Deciduous broadleaf forest	Grassland and meadowland prior to 1960s but has since regrown undisturbed; mainly *Quercus robur*, *Robinia pseudoacacia*, *Alnus glutinosa*, and *Pinus rigida* (Ferréa et al., 2012; Putaud et al., 2014); *Q. robur* (~80%) dominates except to the southeast of the flux tower	Mostly umbrisols with sandy-loam or loamy-sand texture for top 50 cm below which soil is mainly sandy (Ferréa et al., 2012)

			where *A. glutinosa* dominates due to a higher water table	
Harvard Forest, USA	42.54ºN, 72.17ºW	Temperate mixed forest	Regrowing on farmland abandoned over 100 years ago; dominated by *Quercus rubra* and *Acer rubrum*, with scattered individual and patches of *Tsuga canadensis*, *Pinus resinosa*, and *Pinus strobus* particularly to the northwest of the tower where *T. canadensis* are most common (Munger and Wofsy, 2021)	Canton fine sandy loam, Scituate fine sandy loam, and hardwood peat swamp (Savage and Davidson, 2001)
Hyytiälä, Finland	61.85°N, 24.29°E	Evergreen needleleaf forest	Boreal forest; predominately *Pinus sylvestris*; shrubs underneath the canopy are *Vaccinium vitis-idaea* and *Vaccinium myrtillus*, and dense moss covers forest floor (Launiainen et al., 2013); *P. sylvestris* stand established in 1962 and thinned by 25% between January and March 2002 (Vesala et al., 2005)	Haplic podzol formed on glacial kill with 5-cm average organic layer thickness (Kolari et al., 2006)
Ramat Hanadiv, Israel	32.55°N, 34.93°E	Shrub	Near eastern Mediterranean coast; mostly *Quercus calliprinos* and *Pistacia lentiscus*, but also include *Phillyrea latifolia*, *Cupressus*, *Sarcopoterium spinosum*, *Rhamnus lycioides*, and *Calicotome villosa*; west of the measurement tower are scattered *Pinus halepensis* (~5%) (Li et al., 2018)	Xerochrept (Li et al., 2018) and clay to silty clay (Kaplan, 1989)

876

877 For this effort, we selected sites without known influences of highly reactive BVOCs on ozone fluxes. However, there may be

878 unknown influences, especially at coniferous or mixed forests (Kurpius and Goldstein, 2003; Goldstein et al., 2004; Clifton et al.,

879 2019; Vermeuel et al., 2021), and generally the magnitude of the contribution and how it changes with time are uncertain (Wolfe

880 et al., 2011; Vermeuel et al., 2022). Most sites are expected to have very low NO. There may be some influences of NO on ozone

881 fluxes at Ramat Hanadiv (Li et al., 2018) and Ispra, but the magnitude and timing of the contribution is uncertain. Constraining

882 contributions of highly reactive BVOCs and NO to ozone fluxes is beyond the scope of our work here.

883

884 Removal of observed hourly or half-hourly ozone deposition velocity outliers for all sites leverages a univariate adjusted boxplot

885 approach following Hubert and Vandervieren (2008), which explicitly accounts for skewness in distributions and identifies the

886   most extreme ozone deposition velocities at each site. Non-Gaussian univariate distributions, or skewness, are present to some
887   degree in each observational dataset used here. This method designates the most extreme 0.7% of a normal unimodal distribution
888   as outliers, but the exact percentage depends on the degree of skewness. For datasets used here, which can be highly skewed, we
889   filter 1–6% of ozone deposition velocities across sites. Table S17 describes any antecedent post-processing of ozone deposition
890   velocities performed for this effort.

891

892   Many dry deposition schemes include adjustments for snow. Table S18 identifies sites with snow depth (SD) measurements.
893   Unless the single-point model directly takes SD input to infer fractional snow coverage of the surface, we define the presence of
894   snow as SD greater than 1 cm. Models assume no snow if SD less than or equal to 1 cm or missing.

895

896   Canopy wetness is an input to several single-point models. Others do not ingest canopy wetness explicitly as an input variable,
897   but rather indicate canopy wetness using a precipitation and/or dew indicator. For the latter type, the fraction of canopy wetness
898   (f_{wet}) from datasets is not used, and models' indicators are used. Table S18 details canopy wetness measurements at each site.
899   For sites where f_{wet} data are not available, f_{wet} values are approximated using an approach used in CMAQ (Table S18).

900

901   Soil moisture and soil properties and hydraulic variables are important for stomatal conductance as well as soil deposition
902   processes (Fares et al., 2014; Fumagalli et al., 2016; Stella et al., 2011, 2019). Site-specific details of variables used for near-
903   surface and root-zone volumetric soil water content are described in Table S19. A set of soil hydraulic properties (Table S20) are
904   estimated for each site from soil texture and used across models employing these parameters.

905

906   Overall, the core description for each site includes key information needed to drive the single-point models: LULC type,
907   vegetation composition, soil type, and measurement height for ozone fluxes (Tables 2 and S17). We also describe inputs for
908   snow, canopy wetness, h, and LAI (Table S18). Outside of the core description, other meteorological variables are measured with
909   standard techniques, which are not discussed here. When an input variable is inferred, we detail assumptions involved in the
910   inference because variability in inferred input variables may not be accurately represented and this may need to be accounted for
911   in comparing simulated vs. observed ozone deposition velocities (Tables S17 and S19).

912

913   We note that in addition to data screening conducted by data providers, driving datasets were visually inspected and clearly
914   erroneous values were set to missing (e.g., in one case T_a less than -50ºC). Driving datasets are not gap-filled (unless explicitly
915   stated otherwise) so simulated ozone deposition velocities have gaps whenever one or more of a model's input variables is missing.
916   Single-point models require different sets of input variables. Thus, output from different models may have different data gaps at
917   a given site. Additionally, because data capture for observed deposition velocities is based on availability of ozone flux
918   measurements, and data gaps in input variables may be different from data gaps in the ozone flux measurements, simulated
919   deposition velocities can have different data gaps from observed deposition velocities. We address data coverage discrepancies

920   across models and observed deposition velocities in two ways. First, we identify time-averaged observed and simulated

921   deposition velocities with suboptimal coverage in our results (e.g., see Figure 1). Second, we account for diel imbalances in our

922   analysis. Both approaches are described more fully in Section 4.

923   **4 Creation of monthly and seasonal average observed and simulated quantities**

924   We examine averages across 24 hours, except for Ramat Hanadiv. For Ramat Hanadiv, many months have missing values during

925   night and morning and thus we limit our analysis to 11am–5pm. Across sites and analyses, we use a weighted averaging

926   approach for daily averages that considers the number of observations for a given hour to avoid over-representation of any given

927   hour due to sampling imbalances across the diel cycle (e.g., more valid observations during daylit hours).

928

929   There are sometimes periods of missing ozone fluxes in the datasets. We indicate year-specific monthly averages with low data

930   capture for observed ozone deposition velocities (v_d) on Figure 1. Low data capture is defined as less than or equal to 25% data

931   capture averaged across 24 hours (or 11am–5pm for Ramat Hanadiv). In other words, we first compute data capture for each

932   hour of a given month (or season), and then average across hour-specific data capture rates to compare against the 25%

933   threshold. We indicate multiyear monthly averages with low data capture for observations and models on Figures 2 and 3. Note

934   that the number of data points used in constructing monthly averages differs between models and observations, and across

935   models. Data capture for each model depends on availability of the specific measured input data required for driving that model.

936   Data capture for observed v_d is based on availability of ozone flux measurements

937

938   When we examine multiyear averages, we do not consider sampling biases across years (e.g., more valid observations in one

939   year over the other). Thus, more data in one year may skew multiyear averages towards values for that year (Fig. 1). However,

940   results are generally similar if we include weighting by years, except when there are only a few years contributing to multiyear

941   averages, and one or some of those years have low data coverage. For seasonal averages, months are not given equal weight

942   unless stated otherwise. For example, all non-missing data for a given hour across months of the season are considered equally

943   (e.g., that there may be more data at noon in July than August is not considered in a summertime average).

944   **5 Results**

945   Figure 1 shows monthly mean observed ozone deposition velocities (v_d) across years, as well as multiyear averages, at all sites.

946   There are a variety of seasonal patterns and magnitudes of observed v_d across sites. Interannual variability is strong in terms of

947   the standard deviation across yearly annual averages normalized by the multiyear average (range of 10% to 60% across sites). In

948   some cases, periods with low data coverage contribute to apparent interannual variability and/or seasonality. However, more

949   complete ozone flux records also show strong variability from year to year and month to month. The following focuses on

950   multiyear averages, but we briefly examine summertime (June-August) interannual variability at sites with three or more years of

951   data to establish whether models capture the range of interannual variability and/or ranking among different summers.

952

953   Figure 2 shows multiyear monthly mean v_d from observations and the spread across models, whereas Figure 3 shows multiyear

954   monthly mean values from each model and observations. We first consider model ensembles. Across models, minimum and

955   maximum averages bracket observations across sites except Auchencorth Moss (all months except July), Borden Forest (October-

956   November only), and Ispra (October-February only). In some cases, model outliers allow the full set of models to bracket observations

957   (Fig. 3). If we instead consider the interquartile range across models (hereinafter, 'the central models'), then there are at least a few

958   months at every site when observations fall out of range. At the same time, at every site except Auchencorth Moss, there are also at least a

959   few months when the observations are within the range, indicating that failure of central models to capture observations consistently

960   across the seasonal cycle does not suggest a complete lack of skill from the model ensemble that de-emphasizes outliers. Further, central

961   models are very close to bracketing observations across months at Easter Bush, Hyytiälä, and Harvard Forest.

962

963
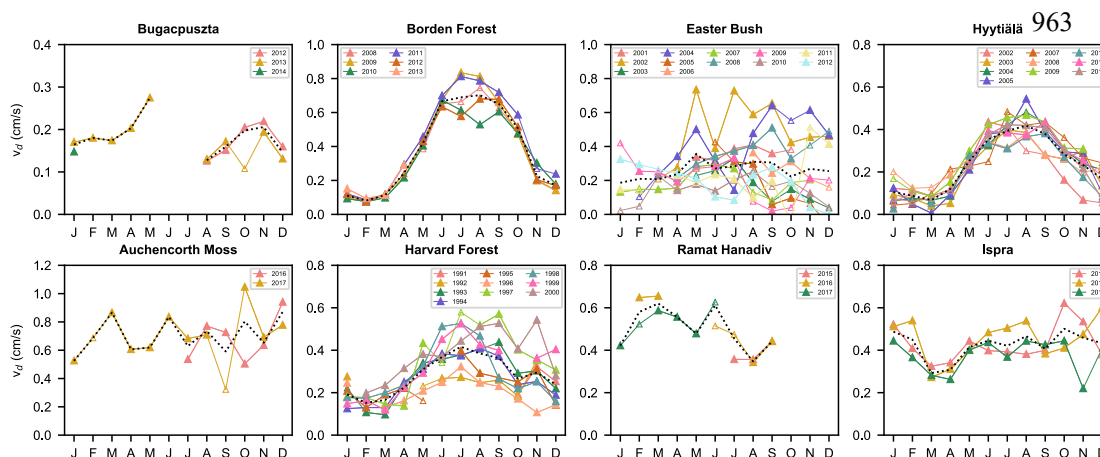
964   Figure 1 Monthly mean ozone deposition velocities (v_d) from the ozone flux observations. Multiyear average is in black. Open
965   symbols indicate months for a given year with low data capture. Note different y-axis ranges among panels.

966   The model spread in multiyear mean v_d across months and sites is large (Fig. 2). The spread in terms of the model with the highest

967   annual average divided by the model with the lowest ranges from 1.8 to 2.3 except Hyytiälä (2.7) and Auchencorth Moss (5). The spread

968   in wintertime (December-February) averages is very high at some sites: Borden (10), Hyytiälä (21), Auchencorth Moss (9.1), and

969   Harvard Forest (6.3). The spread in wintertime averages is 2 to 3.3 at other sites. The spread is typically lower during summer (June-

970   August) than winter, on par with annual values. We also use the 75th percentile divided by the 25th percentile as a metric of the spread.

971   This metric for the annual average is 1.2–1.8. For winter, the metric is also lower for sites with high spreads based on all models: 3 for

972   Borden Forest, 2.4 for Hyytiälä, 3 for Auchencorth Moss, and 2.7 for Harvard Forest.
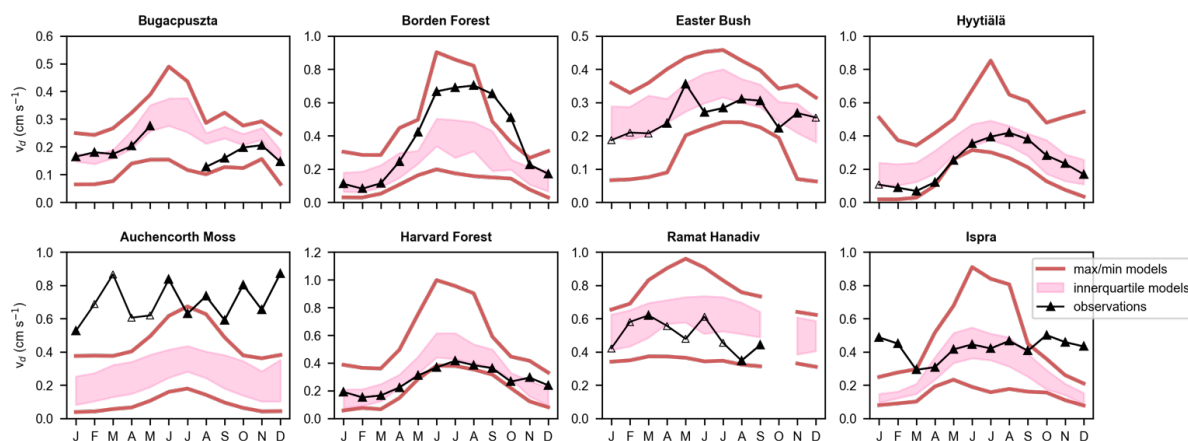
Figure 2 Multiyear monthly mean ozone deposition velocities (v_d) from ozone flux observations and the spread across the single-point models. Pink shading denotes the interquartile range across models. Red lines denote the minimum and maximum across monthly simulated values. Open symbols on observations indicate months with low data capture. Note different y-axis ranges among panels.
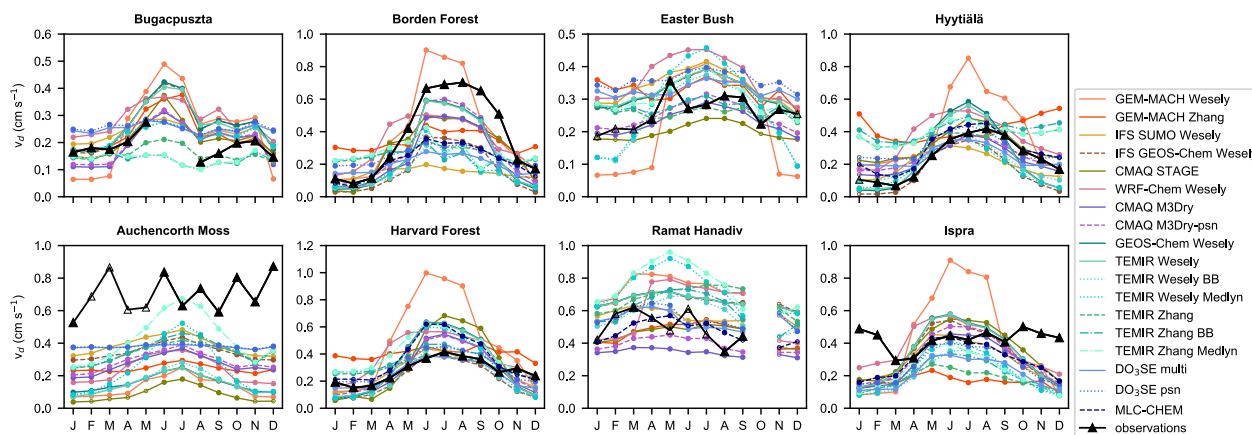

Figure 3 Multiyear monthly mean ozone deposition velocities (v_d) from ozone flux observations and individual single-point models. Open symbols indicate months with low data capture. Note different y-axis ranges among panels.

If we consider individual model performance, then we find that no model is always within 50% of observed multiyear averages across sites and seasons (Fig. 4). Models are very low against observations at Auchencorth Moss, but the previous statement holds even excluding this site. In general, a key finding is that model performance varies strongly by model, season, and site. Below, we first discuss mean absolute biases across sites, and then drivers of seasonality across models and sites. Then, in subsections, we discuss each site, starting with short vegetation, and then forests.

983

984 The mean absolute bias (simulated minus observed) across multiyear seasonal averages and sites is highest for GEM-MACH

985 Wesely (0.22 cm s^{-1}) and lowest for CMAQ M3Dry-psn (0.12 cm s^{-1}). GEM-MACH Zhang, WRF-Chem Wesely, GEOS-Chem

986 Wesely, TEMIR Wesely, TEMIR Wesely BB, and TEMIR Wesely Medlyn are on the higher end of the spread in mean absolute

987 bias across seasons and sites (0.17–0.18 cm s^{-1}), while DO₃SE multi, DO₃SE psn, and IFS SUMO Wesely (0.13 cm s^{-1}) and

988 CMAQ M3Dry (0.14 cm s^{-1}) are on the lower end, with the rest in between (0.15–0.16 cm s^{-1}). (MLC-CHEM does not simulate

989 three sites so we exclude it here).

990

991 Annual mean absolute biases may overemphasize model performance when v_d are high. Given that wintertime v_d tends to be lower in

992 magnitude than during other seasons, we also examine wintertime mean absolute biases across sites. Values are highest for GEM-

993 MACH Zhang (0.22 cm s^{-1}), GEM-MACH Wesely (0.20 cm s^{-1}), TEMIR Wesely (0.20 cm s^{-1}), and TEMIR Wesely Medlyn

994 (0.19 cm s^{-1}). Otherwise, model biases are below 0.16 cm s^{-1}.

995

996 Figure 5 shows simulated multiyear wintertime and summertime mean effective conductances, as well as the observed multiyear seasonal

997 average v_d (recall that simulated effective conductances sum to simulated v_d). The three main pathways are stomata, cuticles, and soil;

998 even when models simulate lower canopy uptake, uptake via this pathway tends to be low. We thus focus on stomatal, cuticular, and soil

999 pathways. There are three important takeaways from Figure 5. First, models can disagree in terms of relative contributions from

000 pathways, even when they predict similar v_d. Conversely, models can agree in terms of relative contributions of pathways but

001 predict different v_d. Second, both stomatal and nonstomatal pathways are important for v_d across models, as well as key drivers

002 of variability across models. Third, models tend to disagree on cuticular vs. soil contributions to nonstomatal uptake at some sites, while

003 agreeing at others.

004

005 Figure 6 shows how multiyear mean seasonality of effective conductances contributes to the multiyear mean seasonality of simulated v_d

006 across models. Specifically, the variance in each pathway across months is shown, as well as twice the covariance between individual

007 pathways. Negative covariances imply offsetting seasonality between the two pathways (i.e., an anticorrelation in seasonal cycles of two

008 pathways, and this acts to dampen the total seasonality). Positive covariances mean that a positive correlation in seasonal cycles of the

009 two pathways acts to amplify total seasonality. Values are normalized by the absolute sum of the variance and twice the covariances so

010 that Figure 6 does not emphasize differences in the seasonal amplitude, rather what pathways control the seasonality.

011

012 The key finding from Figure 6 is that stomatal uptake is the most important driver of multiyear mean v_d seasonality for most models and

013 sites. For some models and sites, cuticular uptake also plays a role, albeit mostly just via correlations with stomatal uptake. Correlations

014 between stomatal and cuticular pathways are mostly positive, and thus tend to amplify v_d seasonality. Exceptions are Hyytiälä and

015 Easter Bush where some models show anticorrelations between stomatal and cuticular uptake seasonal cycles. With a few exceptions

016 (e.g., at Easter Bush and for GEM-MACH Wesely and DO₃SE models), soil uptake tends to play a more minor role.

37

017

018   In general, parameters and dependencies driving simulated v_d seasonality are model dependent. Expected dominant influences include

019   changes in initial resistances with season, cuticular and stomatal dependencies on LAI, stomatal dependencies on soil moisture,

020   temperature response functions (used in Wesely (1989) to decrease nonstomatal deposition pathways at cold temperatures), and

021   changes with snow. Multiyear monthly mean observed and simulated v_d generally increases with LAI across sites during at least some

022   time periods of plant growth (Fig. 7). In general, however, the relationship between v_d and LAI on monthly timescales is nonlinear for

023   both observations and models, distinct between observations vs. models, and distinct across models. Many models show a strong

024   sensitivity to LAI, which has been pointed out in previous work (Cooter and Schwede, 2000; Charusombat et al., 2010; Schwede

025   et al., 2011; Silva and Heald, 2018). Our analysis here, combined with past work, suggests that predictive ability hinges on better

026   understanding of observed v_d-LAI relationships in terms of seasonality and site-to-site differences.

027

028   Figure 8 shows snow's impact on multiyear mean v_d at sites with snow depth records and sufficient snowy periods. Observations suggest

029   modest reductions with snow at Bugacpuszta and Hyytiälä, but not much change at Borden Forest. At Borden Forest, some models show

030   decreases, while others show little change. At Hyytiälä and Bugacpuszta, some models capture decreases with snow despite biases

031   whereas other models understate or exaggerate decreases. Observed reductions with snow are larger at Bugacpuszta than Hyytiälä, and

032   many models capture this. Findings with respect to Borden Forest may reflect that snow is not measured there, rather 15 km away, and

033   thus this not reflect local conditions exactly. Even though some models do not capture the magnitude of observed v_d decreases with

034   snow, Figure 8 shows that models' inability to capture the magnitude of wintertime values (snow or snow-free) at a given site is a much

035   larger problem than models' inability to capturing responses to snow, at least at these three sites. The relative model spread (based on the

036   standard deviation across models divided by the average) does not change substantially under snowy vs. all conditions, except at

037   Bugacpuszta (27% vs. 70%), further underscoring the need to better understand wintertime v_d in a more general sense.

038

039   The relatively low magnitude of snow-induced observed v_d changes indicates that snow-induced changes are not the main driver of

040   observed v_d seasonality (Fig. 8). For example, observed changes with snow are a small fraction of the observed absolute seasonal

041   amplitude of multiyear monthly averages at these sites, at least for Hyytiälä and Borden Forest. We also note that models simulate v_d

042   reductions with snow at Hyytiälä and Bugacpuszta even when snow is not model input, suggesting that other model dependencies (e.g.,

043   temperature response functions) may lead to changes coincident with snow. Recent papers suggest that better snow cover representation

044   may be key for v_d spatial variability at regional scales and seasonal cycles as well as changes with climate change (Helmig et al., 2007;

045   Andersson and Engardt, 2010; Matichuk et al., 2017; Clifton et al., 2020b). Despite insufficient data to examine spatial variability or

046   responses to climate change, our analysis suggests drivers of wintertime v_d other than snow are important to understand.
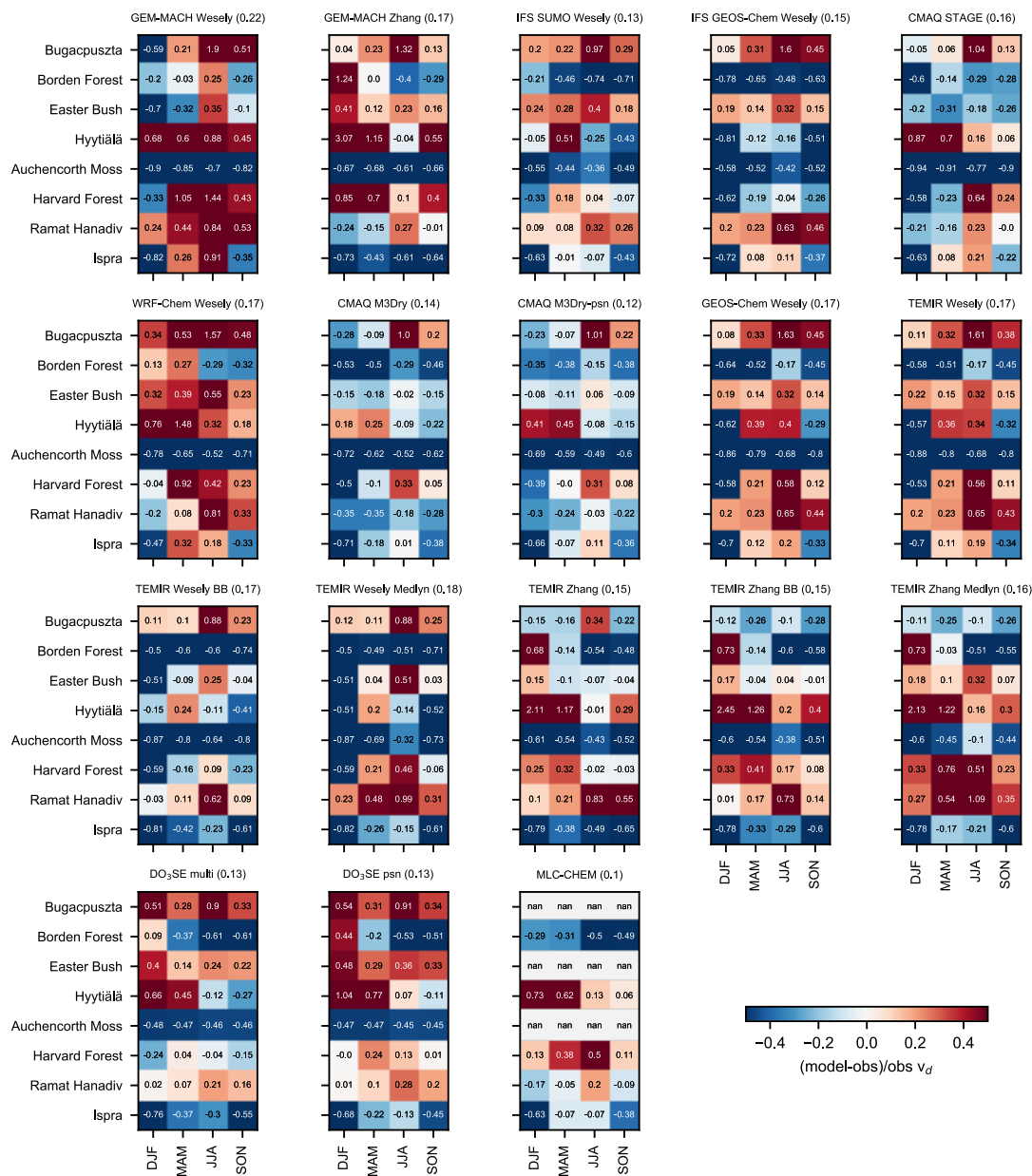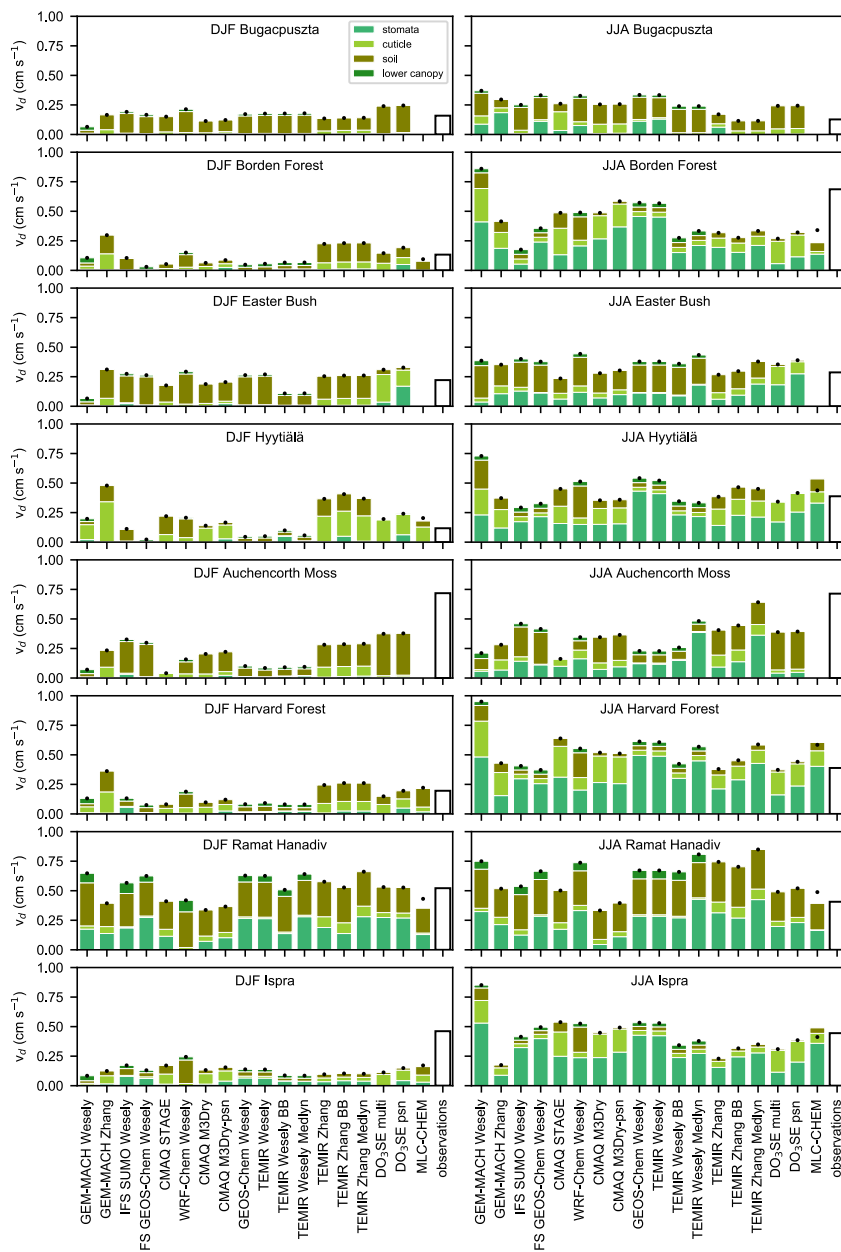
Figure 2 Relative biases (simulated minus observed divided by observed) across models, sites, and seasons for ozone deposition velocities (v_d), expressed in fractions. Numbers next to model names in the subpanel titles are mean absolute biases across seasons and sites in cm s^{-1}.
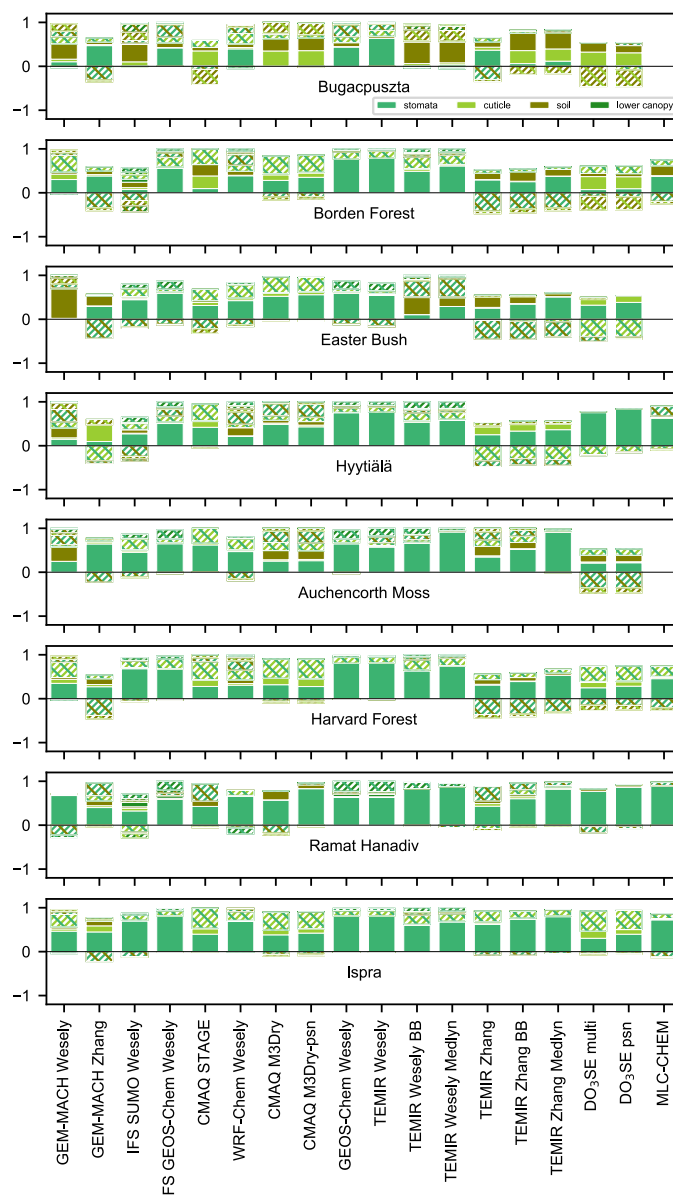
Figure 3 Multiyear seasonal mean simulated effective conductances and observed ozone deposition velocities (v_d). Black dots are simulated v_d (black dots should equal the top of the bars). DJF is December, January, and February. JJA is June, July, and August.

055
Figure 4 Pathways contributing to variability across simulated multiyear monthly mean ozone deposition velocities. The variance
056 for each effective conductance is solid. Twice the covariance between effective conductances is hatched (the colors of hatch
057 correspond to pathways examined). Each value is normalized by the absolute value of the sum of the variances and twice the
058 covariances so that we are comparing the pathways that drive seasonality across models in a relative sense (rather than the
059 seasonal amplitude as well).
060
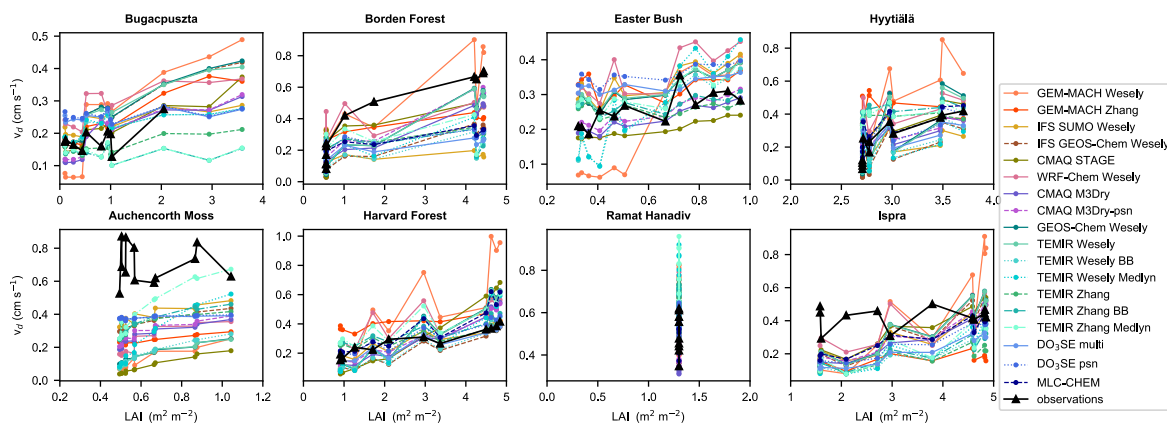
Figure 5 Multiyear monthly mean ozone deposition velocities (v_d) versus leaf area index (LAI).

5.1 Bugacpuszta

Bugacpuszta is a semi-arid and semi-natural grassland in Hungary. In terms of variability across models, the model spread based on the model with the highest annual average v_d divided by the model with the lowest is 2.1 (2.8 during summer and 2.2 during winter) but based on the interquartile range is 1.3 (1.2 during summer and 1.3 during winter). The model spread at Bugacpuszta is on the lower end of the estimates across sites examined.

A longer ozone flux record data is needed to assess interannual variability at Bugacpuszta. This site has only a single year of data during February–May (2013), two years of data during August–December (2012 and 2013), and two years of data during January (2013 and 2014) (Fig. 1). Data is always missing during June and July. For time periods with two years of data, observed monthly mean v_d are very close in magnitude between years. The exception is October when 2013 values are half of the 2012 values. However, October 2013 has very low data coverage (only ~2–3 days of coverage), and hourly values show high uncertainty compared to other months (not shown). We thus focus below on 'multiyear averages', acknowledging that there are only two years of data during six months of the year (with ten months total with data).

Without June and July observations, we cannot fully assess seasonality at Bugacpuszta. Instead, we evaluate seasonality across other months. Thus, the observed seasonal cycle is: v_d maximizes during May, following an increase from March, and minimizes during August, after which v_d increases to November and levels off from December–February (Fig. 1). Seasonal patterns are similar across many models, with mid-summer peaks after slow increases from winter and similar values from August–November (Fig. 3). Despite similar seasonal patterns across models as well as fair agreement in the relative seasonal amplitude (Fig. 9), models disagree with respect to pathways dominating the seasonal cycle (Fig. 6). Notably, models disagree most in terms of pathway(s) driving seasonality at Bugacpuszta relative to other sites, suggesting that changes in individual pathways on seasonal timescales at this location may be a key uncertainty.

085

086
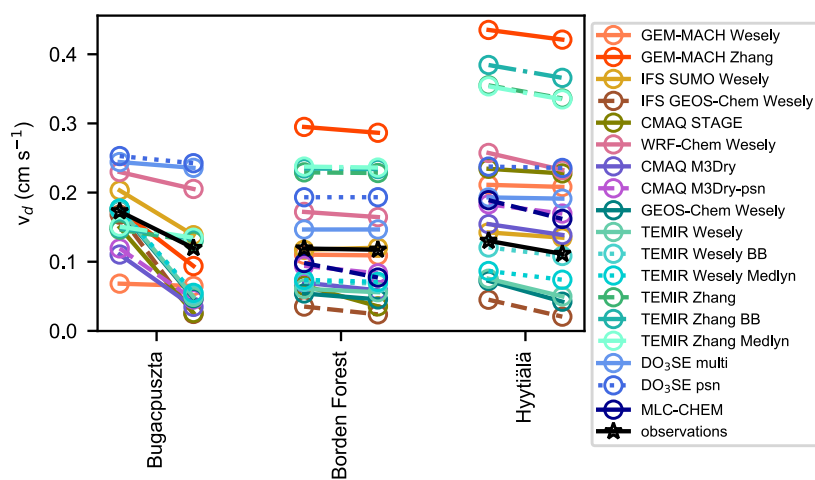
Figure 6 Multiyear mean ozone deposition velocity (v_d) for all conditions versus when snow depth greater than or equal to 1 cm for sites with snow depth records and sufficient time with snow (25% averaged across hours per month). Months considered are December-February for Bugacpuszta, December-February for Borden Forest, and November-March for Hyytiälä. Months are given equal weight in averages.

Central models bracket observed v_d during December–May but are too high during August and September (and only slightly too high during October and November) (Fig. 2). Two clear model outliers during warm months are TEMIR Zhang models (Fig. 3), which show relatively low soil and cuticular uptake (Fig. 5). TEMIR psn also show no stomatal uptake, following very low input root-zone soil moisture (below prescribed wilting point). At the same time as TEMIR Zhang models are clear model outliers during warm months, they allow the complete set of models to bracket observations during August-November, as others are mostly too high (or in a few cases just right). Without June and July ozone fluxes, however, it is unclear how TEMIR Zhang models alter summertime performance of the model spread.

Only eight models show substantial summertime stomatal uptake at Bugacpuszta (Fig. 5). There is no summertime stomatal uptake simulated by TEMIR psn, IFS SUMO Wesely, and DO₃SE models, and very little by CMAQ M3Dry and CMAQ M3Dry-psn. Only these models simulate dry deposition at this site and employ soil moisture dependencies on stomatal conductance. They simulate little-to-no stomatal uptake at Bugacpuszta because input soil moisture is below prescribed wilting point. We emphasize that wilting point, which is not measurable, is uncertain across sites. Models with substantial summertime stomatal uptake show a large spread in stomatal fractions of v_d – from 12.5% to 40% with one model simulating 60% (Fig. 12) – and produce distinct stomatal uptake seasonal cycles (Fig. 10). Many models show similar v_d seasonal cycle shapes (Fig. 3) but dissimilar stomatal uptake seasonal cycle shapes, suggesting that nonstomatal uptake seasonality plays a role in normalizing differences in v_d seasonal cycles across models.

108

109   Bugacpuszta has the most similar summertime model spreads for the top three pathways as compared to other sites (except

110   Hyytiälä) (Fig. 11), suggesting a high degree of uncertainty in the magnitude of all pathways during warm months. Most models

111   show substantial summertime contributions from soil uptake, but the magnitude of soil uptake varies across models (Fig. 5). In

112   contrast, for summertime cuticular and stomatal pathways, models disagree as to whether contributions are substantial in addition

113   to the magnitude of uptake. For example, like how some models show very low stomatal uptake (as discussed above), some

114   models show negligible cuticular uptake. Establishing whether there should be summertime stomatal and/or cuticular uptake at

115   Bugacpuszta would be a first step towards further constraining models.

116

117   Multiyear monthly mean LAI shows a sharp summer peak, maximizing during June ($\sim$3.6 m^2 m^{-2}) (Fig. 10). Values are similar

118   during August to November, and then decreases from November to March, with a minimum during March. Observed v_d is

119   missing for LAI greater than 2 m^2 m^{-2} (corresponding to June and July). There is no discernable observed v_d-LAI relationship for

120   LAI below 1 m^2 m^{-2}, and models capture this (Fig. 7). Observations show a strong v_d increase from 1 to 2 m^2 m^{-2}. Models show

121   an increase, but most do not capture the large observed slope. This is especially true for models with soil moisture dependencies

122   on stomatal conductance, implying that during at least some periods of high vegetation density, there should not be soil moisture

123   stress, or as strong of soil moisture stress as simulated by some models.

124

125   Models simulate that soil uptake dominates wintertime v_d (Fig. 5). The exception is GEM-MACH Wesely, which

126   underestimates wintertime v_d. Wintertime stomatal fractions can be up to 10% due to low v_d but are mostly within 0–5%.

127   Because central models capture wintertime v_d (Fig. 2), and models agree that soil uptake dominates, some models may have

128   some skill during cooler months at Bugacpuszta. There is variability in soil uptake across models (Fig. 11), however. Models

129   largely capture observed wintertime v_d decreases with snow, with most slightly overestimating the change but a few (DO$_3$SE models,

130   WRF-Chem Wesely, TEMIR Zhang, GEM-MACH Wesely) underestimating it (Fig. 8). Future attention to non-central models should

131   focus on capturing wintertime nonstomatal uptake generally, rather than changes with snow.

132

133   A key outstanding question at Bugacpuszta is: should models simulate low stomatal uptake throughout summer, or only during

134   late summer? Most models are too high against observations during August and September. This includes models employing soil

135   moisture dependencies on stomatal conductance (and thus simulate very-low-to-no stomatal uptake), implying too-high

136   simulated nonstomatal uptake. Continuous year-round ozone flux observations, especially during periods of the growing season

137   with and without moisture stress, are needed to better assess model performance at Bugacpuszta. Independent measures of

138   stomatal conductance during periods of missing ozone fluxes would be useful in constraining the absolute stomatal portion of dry

139   deposition, but further constraining nonstomatal uptake, which models indicate is an important fraction of summertime v_d

140   (despite disagreeing on the exact pathway), requires additional ozone flux measurements.

141
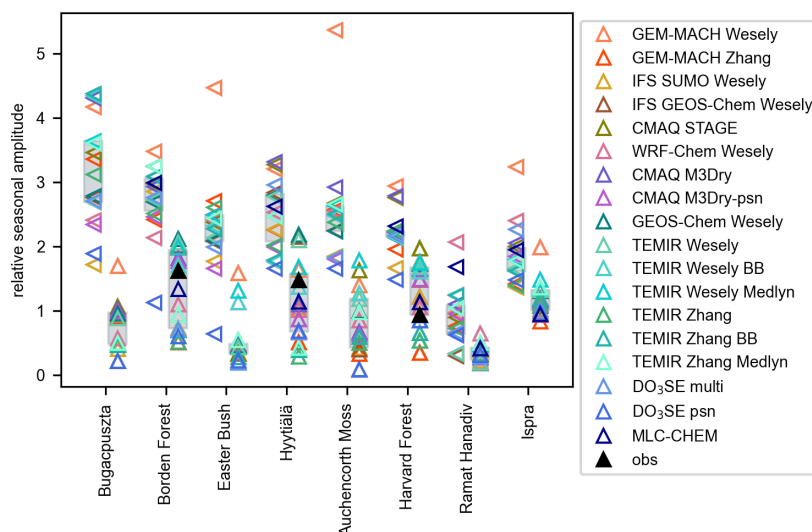
Figure 7 Relative seasonal amplitudes of multiyear monthly mean stomatal uptake (sideways triangles) and ozone deposition velocities (upwards triangles) across models, defined as the maximum across months of multiyear monthly averages minus the minimum, divided by the average. Black triangles denote the relative seasonal amplitude of observations for sites with wintertime minima and summertime maxima. Grey shading denotes the interquartile range across models.

5.2 Auchencorth Moss

Auchencorth Moss is a peat bog covered with heather, moss, and grass in Scotland. The model spread in terms of the model with the highest annual average v_d divided by the model with the lowest is 5 (4.3 during summer and 9.1 during winter) but based on the interquartile range is 1.6 (1.5 during summer and 3 during winter). Across sites, for the annual metrics, Auchencorth Moss has the largest spread for the maximum/minimum metric and the second largest for the interquartile range.

There is no clear shape of the observed v_d seasonal cycle at Auchencorth Moss (Fig. 1). Whether this is true on a climatological basis is unclear due to data incompleteness – observed values during February–May have low data capture mostly because data are missing during 2016 – as well as strong interannual variability and only two years of data. A longer and more complete ozone flux data is needed to fully assess interannual variability as well as seasonality at Auchencorth Moss. We focus below on 'multiyear averages', acknowledging that only half the months of the year have two years of data.

A key finding for Auchencorth Moss is that models do not capture high observed v_d year-round (Fig. 2). The exception is TEMIR Zhang Medlyn during July. This is the only site examined with negative biases (> 30% of observed multiyear seasonal averages) across seasons and models (except for TEMIR Zhang Medlyn during July) (Fig. 4). Biases tend to be smallest during summer and largest during winter because many models simulate peak v_d during warm months (Fig. 3). Notably, models differ

45

163   substantially in their relative seasonal amplitudes, with a very even and wide distribution across models (Fig. 9), especially

164   relative to other short vegetation sites.
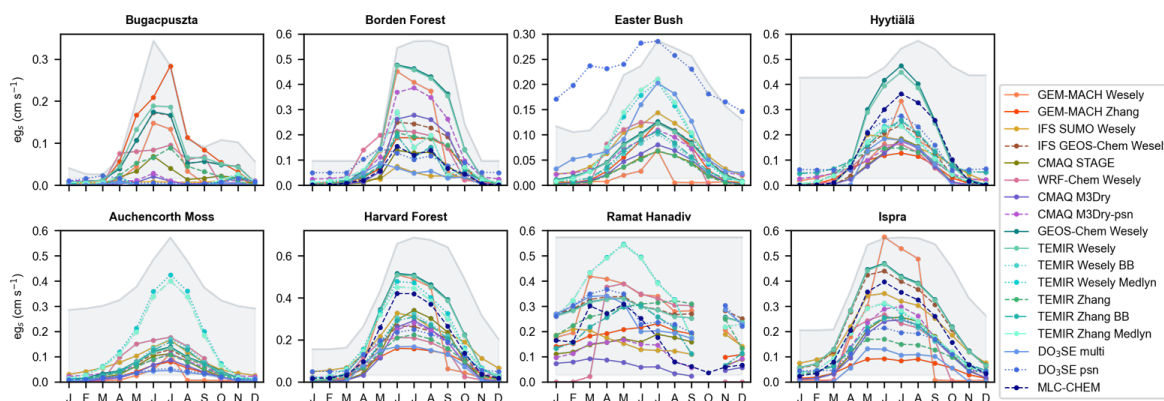
165
166   Figure 8 Multiyear monthly mean effective stomatal conductance (eg_s) from single-point models. Grey shading denotes
167   multiyear monthly mean leaf area index (used to emphasize seasonality in this variable; y-ranges not given). Note different y-
168   axis ranges for eg_s among panels.

169   Simulated v_d seasonality is mostly due to stomatal uptake (Fig. 6). Some models show that soil uptake plays a role, and all but

170   two models show moderate contributions from correlations between pathways. The seasonality shape and magnitude of stomatal

171   uptake is very similar across most models (Fig. 10). Major exceptions are TEMIR Medlyn models, which show peak values

172   around 0.4 cm s^{-1} in contrast to the rest that average just under 0.1 cm s^{-1}. For the relative seasonal amplitudes in stomatal uptake,

173   the spread across central models is low (Fig. 9). The value for GEM-MACH Wesely is very high (> 5), with other models'

174   values spanning 1.75 to 3. Models deviating from the rest with respect to stomatal uptake's seasonality shape are GEM-MACH

175   Zhang (near-zero during August and after; strong peak during July) and DO$_3$SE (low during summer) as well as WRF-Chem

176   Wesely and IFS SUMO Wesely (the latter two are similar and higher than others especially during spring).

177

178   While high summertime stomatal uptake combined with moderately high year-round nonstomatal uptake distinguishes TEMIR

179   Zhang Medlyn from others (Fig. 5), we see the best agreement between this model and observations during warm months.

180   However, TEMIR Zhang Medlyn does not capture observed seasonality (or lack thereof). TEMIR Zhang Medlyn may have more skill

181   during summer than other models, but like other models, TEMIR Zhang Medlyn struggles with seasonality. Future work should

182   establish whether there is strong seasonality in stomatal uptake coupled with offsetting seasonality in nonstomatal uptake at Auchencorth

183   Moss, or whether stomatal uptake should be higher year-round.
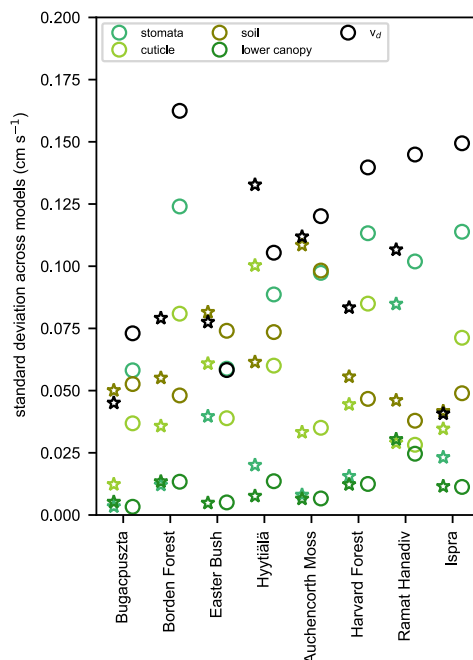
Figure 9 Model spread (standard deviation) across multiyear seasonal mean ozone deposition velocities (v_d) and effective conductances for DJF (stars) and JJA (circles). DJF is December, January, and February. JJA is June, July, and August.

For soil uptake, the model spread is strong and similar during summer and winter (Fig. 11). During summer, the spread in stomatal uptake is on par with soil uptake; spreads for stomatal and soil uptake are highest across pathways. During winter, the spread in stomatal uptake is very low, and the spread in soil uptake is highest. Wintertime stomatal fractions vary from 0% to 20% across models (Fig. 12). Models except CMAQ STAGE simulate non-negligible soil uptake (Fig. 5). However, during summer, models disagree on soil contribution to v_d (0–80%) as well as the magnitude of soil uptake. In contrast, during winter, models agree that soil uptake contributes substantially (>60%) (apart from CMAQ STAGE and GEM-MACH Wesely) but disagree on the magnitude of soil uptake. Snow depth is measured at Auchencorth Moss, but data are missing for half the ozone flux period, and there is not a substantial amount of time with snow when there are measurements. We do not expect a large impact on simulated values by accounting for snow throughout the ozone flux period.

Models estimate very-low-to-moderate cuticular uptake at Auchencorth Moss (Fig. 5), which is consistent across low vegetation sites. Moderate values of cuticular uptake are simulated by GEM-MACH Zhang and TEMIR Zhang models, and values are similar between summer and winter. Otherwise, models simulate very little cuticular uptake during winter and low cuticular uptake during summer. Nonetheless, the model spread in cuticular uptake is similar between seasons. Summertime stomatal fractions vary across central models from 25% to 55% (Fig. 12). Aside from one model simulating 80% and two models around

47

202 10%, half are around 20–30% and the other half are around 45–60%. There is a division across models in that no model

203 simulates stomatal fractions between 32.5% and 45%. The dichotomy seems to be due to variability in both stomatal and soil

204 uptake across models, consistent with high summertime model spreads for these pathways (Fig. 11).

205
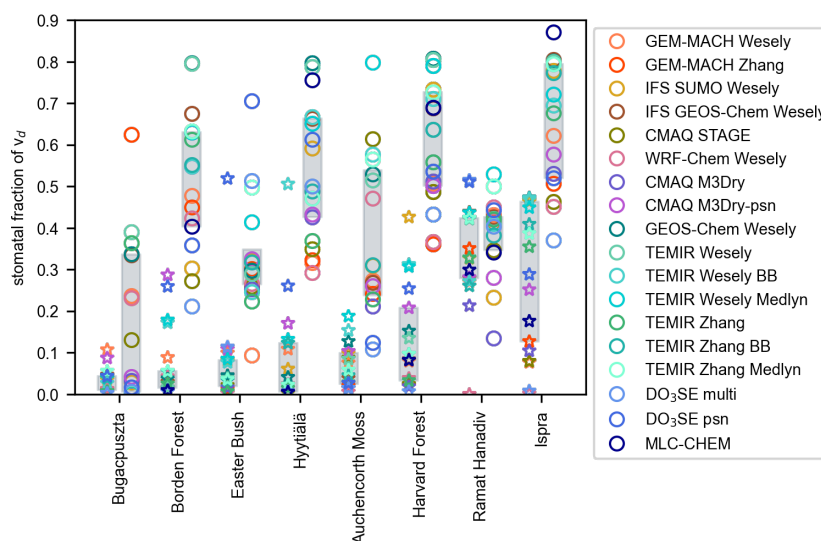
206
207 Figure 10 Multiyear seasonal mean stomatal fractions of ozone deposition velocities (v_d) across models during DJF (stars) and
208 JJA (circles). Grey shading denotes the interquartile range across models. DJF is December, January, and February. JJA is June,
209 July, and August.

210 Despite an unclear observed v_d seasonal pattern, the relationship between monthly mean *LAI* and v_d may provide insights into

211 model performance. With strong observed v_d variations at low *LAI* (less than 0.6 m^2 m^{-2}), there is thus relationship, but there is a

212 positive relationship at moderate *LAI* (in the range of 0.6 to 0.9 m^2 m^{-2}) (Fig. 7). Observations then show that v_d decreases with

213 *LAI* increases above 0.8 m^2 m^{-2} but there is only one data point here. Most models seem to capture the observed relationship at

214 moderate *LAI* as well as that there should not be a relationship at low *LAI*. Some models (e.g., TEMIR models) overestimate the

215 increase's slope at moderate *LAI*, though. Thus, some models may have some skill at simulating seasonality in cuticular and/or

216 stomatal uptake. Nonetheless, strong observed v_d variability at low *LAI* and changes with *LAI* during peak vegetation density need better

217 understanding. With observational constraints on stomatal uptake, we will be able to understand whether nonstomatal uptake should be

218 higher year-round and/or seasonality in nonstomatal uptake should act to offset seasonality in stomatal uptake.

219

220 We close by emphasizing that very high observed v_d at Auchencorth Moss are uncertain – there is strong interannual and day-to-day

221 variability, but a lot of missing data. The peat/bog LULC type does not have many ozone flux measurements at other sites that

222 could be used to provide additional context to Auchencorth Moss measurements. Schaller et al. (2022) show that v_d ranges from

223 0.05 cm s^{-1} at night to 0.45 cm s^{-1} during the day in July 2017 at a peatland in NW Germany. El Madany et al. (2017) look at

224 ozone fluxes at the same site during 2014 but does not present v_d. Fowler et al. (2001) present older measurements at

225 Auchencorth Moss, estimated with the gradient technique (eddy covariance is used for the data examined here), showing much

226 lower observed v_d than examined here (e.g., winter and fall values here are twice what they are during 1995-1998, summer are

227 almost twice, and spring are higher but not twice). It is not clear what drives higher, more recent v_d measurements at

228 Auchencorth Moss analyzed in this study and more detailed analysis is needed to figure it out. In general, building understanding

229 of ozone dry deposition at this LULC type provides a key test of understanding of soil uptake, and its dependence on its expected

230 drivers (soil organic carbon and water content), given peat/bog soils are organic rich and wet.

231 **5.3 Easter Bush**

232 Easter Bush is a managed grassland used for silage harvest and intensive grazing in Scotland. In terms of variability across

233 models, the spread based on the model with the highest annual average v_d divided by the model with the lowest is 1.8 (1.8 during

234 summer and 3.0 during winter) but based on the interquartile range is 1.3 (1.3 during summer and 1.4 during winter). Model

235 spreads at Easter Bush are some of the lowest compared to other sites.

236

237 Easter Bush has one of the longest ozone flux records (Clifton et al., 2020a), and the longest record examined here as well as

238 strongest interannual variability. For example, the coefficient of variation across years is on average 60% across months. In

239 contrast, other sites show coefficients of variations across years from 10% to 30%. There is also strong interannual variability in

240 the observed seasonal cycle's shape at Easter Bush (Fig. 1). As for other sites with long term records, we focus on multiyear

241 averages but touch on summertime interannual variability. Some models capture some low summers, but models do not capture

242 high summers (except GEOS-Chem Wesely, IFS GEOS-Chem Wesely, and TEMIR Wesely, which capture one high year) and

243 underestimate interannual spread (Fig. 13). Future work should focus on understanding observed interannual variability, and

244 consider that interannual variability changes strongly by month, both in terms of the spread across years and ranking of years.

245

246 The central models' spread largely brackets observed multiyear monthly values across months. Specifically, observed values sit

247 mostly on the lower end of or just below the central models' spread, except during May, November, and December when

248 observed values are on the higher end (Fig. 2). Only CMAQ STAGE consistently shows lower v_d than observed, but the relative

249 bias is low (-18% to -30%) (Fig. 4). During winter, GEM-MACH Wesely and TEMIR Wesely psn are too low, and the relative

250 biases are substantial (-51% to -70%). With a few exceptions (i.e., winter for GEM-MACH Wesely and TEMIR Wesely psn,

251 summer for WRF-Chem Wesely and TEMIR Wesely Medlyn), models are within ±50% of observed seasonal averages.

252

253 Overall, the below suggests that models may have skill at simulating climatological v_d seasonality at Easter Bush, aside from a

254 clear set of outliers. There is a weak warm-season peak in observed v_d (Fig. 3). Models show weak warm-season maxima and

255 relatively similar relative seasonal amplitudes (Fig. 9). Some models are clear outliers, however. For example, GEM-MACH

256 Wesely and TEMIR Wesely psn show particularly strong relative seasonal amplitudes (Fig. 9), in part due low wintertime v_d.

257   The absolute standard deviation across models for v_d is higher during winter than summer (Fig. 11). This only happens at Easter

258   Bush and Hyytiälä; however, as noted above, the wintertime model spread reduces when considering the full vs. interquartile

259   range, suggesting that low outliers may drive the large standard deviation across models.

260

261   For most models, the primary driver of v_d seasonality is stomatal uptake (Fig. 6). Individual contributions from stomatal uptake

262   barely contribute for GEM-MACH Wesely, TEMIR Wesely, and TEMIR Wesely BB. Several models, including GEM-MACH

263   Wesely, GEM-MACH Zhang, and TEMIR Wesely models, and to a lesser extent some TEMIR Zhang models, simulate large

264   contributions from soil uptake individually and/or via correlations with other pathways. Only two models, in contrast to seven at

265   the other grassland examined (Bugacpuszta), suggest that individual contributions from cuticular uptake matter for seasonality.

266

267   Most models are similar in terms of magnitude and seasonality shape of stomatal uptake (Fig. 10), as well as relative seasonal

268   amplitudes (Fig. 9). Exceptions are GEM-MACH Wesely (a very strong peak during July and is near zero after July; and thus

269   shows an anomalous seasonal amplitude), TEMIR Medlyn (much higher than other models during warm months), as well as IFS

270   SUMO Wesely and WRF-Chem Wesely (slightly higher than other models especially during spring). DO$_3$SE models are also an

271   exception – they show very different seasonal cycles from each other, despite both being high and seasonally distinctive relative

272   to other models. DO$_3$SE psn also shows an anomalous seasonal amplitude.

273

274   At Easter Bush, *LAI* peaks during July, with a broad maximum from May to November and low values during February and

275   March (Fig. 10). With some exceptions, models bound the observed relationship between v_d and *LAI*, agreeing on a fairly weak

276   but positive dependence (Fig. 7). Outliers with respect to the v_d-*LAI* relationship (GEM-MACH Wesely and TEMIR Wesely psn)

277   also indicate that stomatal uptake does not strongly influence v_d seasonality, suggesting the latter is incorrect.

278

279   During summer, model spreads for v_d and deposition pathways are highest for soil uptake, then stomatal uptake, and then

280   cuticular uptake (Fig. 11). Most models simulate moderate or substantial stomatal uptake, but there is a division as to whether

281   models simulate very low, low, or moderate cuticular uptake (Fig. 5). Models simulate substantial soil uptake, both in terms of

282   absolute magnitudes and relative contributions. Exceptions are DO$_3$SE models, which have very low soil uptake. Stomatal

283   fractions range from 10% to 70%, with most models around 30% and only four models above 40% (Fig. 12). The range across

284   models for stomatal fractions is one of the largest across sites, but the interquartile range is one of the smallest. High agreement

285   in stomatal uptake magnitude, seasonality shape, and relative amplitude, as well as stomatal fractions, across most models

286   suggests that the next step should be to use observation-based estimates of stomatal uptake (e.g., from water vapor fluxes) to

287   evaluate whether models are accurate with respect to this pathway.

288

289   During winter, models simulate that v_d is dominated by soil uptake, with some models simulating low-to-moderate contributions

290   from cuticular uptake (Fig. 5). Only DO$_3$SE models and GEM-MACH Wesely show little soil uptake; while soil uptake is still a

291   large fraction of v_d for GEM-MACH Wesely, it is a small fraction for DO$_3$SE models. Stomatal uptake is very low except for

292   DO$_3$SE psn. Stomatal fractions are between 0% and 10% except DO$_3$SE psn (50%) (Fig. 12). Because models largely agree that

293   wintertime v_d is dominated by soil uptake, and most models overestimate January–April v_d, but underestimate November–

294   December, future work should focus on changes in soil uptake on weekly to monthly timescales. We do not have snow depth

295   measurements at Easter Bush, but do not expect that accounting for snow would substantially impact on simulated values.

296   **5.4 Ramat Hanadiv**

297   Ramat Hanadiv is a shrubland is Israel near the Mediterranean coast. The spread based on the model with the highest annual

298   average v_d divided by the model with the lowest is 2.2 (2.3 during summer and 2 during winter) but based on the interquartile range

299   is 1.4 (1.3 during summer and 1.5 during winter). Metrics are on the lower end of the cross-site range.

300

301   There are ozone flux observations at Ramat Hanadiv during January–September only, and only March, August, and September

302   have substantial data coverage. Three different years contribute to multiyear averages, with each year only having a few months

303   of data per year. For some months, years have overlapping data coverage. Some months with data for two years show interannual

304   variability while others do not. Like Bugacpuszta and Auchencorth Moss, more data is needed to assess interannual variability as

305   well as seasonality at Ramat Hanadiv. Below, we examine 'multiyear averages', acknowledging that only six months of the year

306   have two years of data, and three months have data from one year only.

307

308   Models show weak relative seasonal amplitudes for v_d (Fig. 9). Values are very similar across models, more so than other sites.

309   Most models also show weak relative seasonal amplitudes for stomatal uptake, but there is a larger spread across central models

310   and some outliers. The lack of simulated seasonality for most models is likely due to constant *LAI*. Any simulated v_d seasonality

311   is from stomatal uptake (Fig. 6), more so than (or in contrast to) the other short vegetation sites. GEM-MACH Wesely and WRF-

312   Chem Wesely, which are two of three models with input initial resistances (i.e., model parameters) varying by season, have very

313   distinct v_d seasonal cycle shapes at this site, compared to the rest (Fig. 3).

314

315   The seasonal cycle shape of observed v_d at Ramat Hanadiv is hard to discern with many months with low or no data coverage

316   (Fig. 1). The current set of observations indicates higher values during early spring and lower values during late summer.

317   Individual models do not to capture this, with models simulating near-constant values year-round or increases from winter to

318   early summer (Fig. 3). Exceptions are MLC-CHEM, DO$_3$SE models, and GEM-MACH Wesely, which at least somewhat

319   capture that the predominant seasonality feature should be lower late-summer values and higher early-spring values.

320

321   Across months with observations, models bracket observed v_d (Fig. 2). In particular, models are within -35% to +55% of

322   observed seasonal averages (Fig. 4). Exceptions occur during summer and include GEM-MACH Wesely, IFS GEOS-Chem

323   Wesely, WRF-Chem Wesely, GEOS-Chem Wesely, TEMIR Wesely models, and TEMIR Zhang models (biases are higher than

324   +55%). The central models' spread only brackets observed values during January-April and June, and is too high during May

325   and July-September. The largest deviation happens during August. Thus, like Bugacpuszta, late summer is when the largest

326   model biases occur at Ramat Hanadiv.
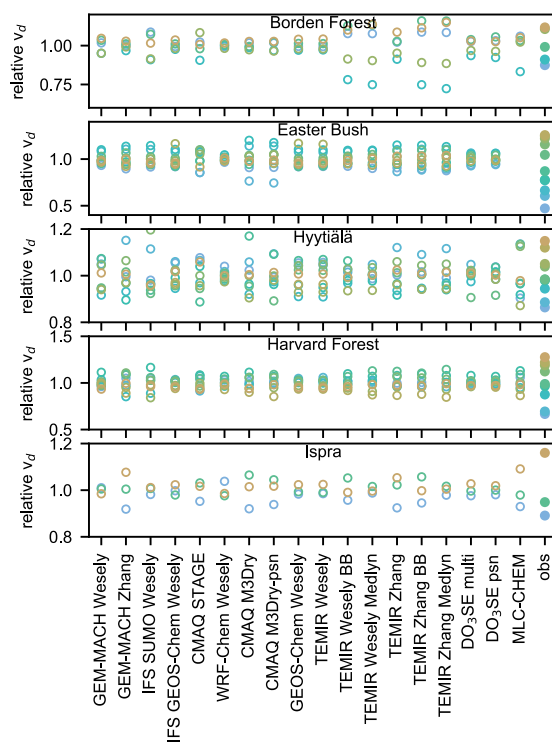
328   Figure 11 Simulated and observed yearly summertime mean ozone deposition velocities (v_d) for sites with records of at least
329   three summers. Values are normalized by the multiyear average of the respective model or observations to emphasize ranking
330   and spread across years. Colors rank yearly values from low (blue) to high (gold) for the observations. Model year when
331   observed year is missing is not shown. The highest year for Easter Bush is not shown because it is very high (2x the multiyear
332   mean observed value). Note that y-axis ranges vary among panels.

333   DO3SE models, MLC-CHEM, and TEMIR psn show weak v_d decreases from spring to fall. These models plus CMAQ models

334   consider stomatal conductance dependencies on soil moisture. CMAQ models show weaker v_d declines from spring to fall,

335   compared to DO3SE models, MLC-CHEM, and TEMIR psn. This behavior is consistent with their soil moisture dependencies.

336   For example, TEMIR psn and IFS SUMO Wesely models' stomatal conductance is set to zero when input soil moisture is less

337   than wilting point, but CMAQ models have more of a taper effect. Future work should aim to understand the role of soil moisture

338   on observed seasonal variation in v_d and stomatal uptake.

339

340   Models with the highest biases during April-September are TEMIR models, GEM-MACH Wesely, WRF-Chem Wesely, GEOS-

341   Chem Wesely, and IFS GEOS-Chem Wesely (Fig. 3). These models simulate the highest stomatal uptake during this period,

342 apart from a few models with lower-than-average nonstomatal uptake (CMAQ STAGE, DO₃SE models, GEM-MACH Zhang)

343 (Fig. 5). Only CMAQ M3Dry models capture low observed v_d during August. CMAQ M3Dry-psn captures July, but CMAQ

344 M3Dry does not, and they do not capture observed values during other months. Notably, CMAQ M3Dry models show much

345 lower summertime stomatal uptake than other models. CMAQ M3Dry models may have more skill during summer than other

346 models, but like the other models, they struggle with seasonality.

347

348 Lower canopy uptake is the highest for Ramat Hanadiv, both during summer and winter, across sites. However, relative and

349 absolute contributions of lower canopy uptake are still low compared to at least soil and stomatal uptake. Lower canopy uptake is

350 only simulated by Wesely models. Mostly Wesely models simulate low cuticular uptake compared to other models, so lower

351 canopy uptake does not necessarily contribute to the very high model biases of Wesely models.

352

353 Uptake by soil and stomata mostly comprises v_d during winter and summer (Fig. 5). The model spread is highest for stomatal

354 uptake during winter and summer, compared to other pathways (Fig. 11). The spread for soil uptake is remarkably low given its

355 importance across models (less than 20% relative spread compared to mostly between 40–75% of v_d). Ramat Hanadiv is the

356 only site with a large wintertime spread across stomatal uptake estimates, and similar model ranges of stomatal fractions during

357 winter and summer. Models except WRF-Chem Wesely show substantial wintertime stomatal uptake. In general, stomatal uptake

358 is very high compared to other sites during winter, presumably due to the site's Mediterranean climate. Models also show

359 substantial summertime stomatal uptake except CMAQ M3Dry. Wintertime stomatal fractions range from 20% to 50% across

360 models (Fig. 12). The range is only slightly less across central models (25–40%), suggesting that wintertime stomatal uptake is a

361 key uncertainty at this site. Central models simulate a very small range of summertime stomatal fractions (similar to only Easter

362 Bush), centering on 40%, but the full range spans 12.5% to 50%.

363

364 At Ramat Hanadiv, most models should simulate lower stomatal and/or nonstomatal uptake during late summer, on par with

365 CMAQ M3Dry models, which have both lower stomatal and nonstomatal uptake than other models. However, stomatal and/or

366 nonstomatal uptake should be higher than simulated by CMAQ M3Dry during other times of year, and other models bracket

367 observations well at this time so they may provide insight here as to driving processes. Observational constraints on stomatal

368 uptake year-round will help to further narrow uncertainties as to whether and when models need improvement with respect to

369 stomatal vs. nonstomatal uptake, including when they capture the absolute magnitude of v_d well.

370 **5.5 Ispra**

371 Ispra is a deciduous broadleaf forest in northern Italy. The model spread in terms of the model with the highest annual average

372 v_d divided by the model with the lowest is 2.3 (3.1 during summer and 2.9 during winter) but based on the interquartile range is 1.5

373 (1.5 during summer and winter). These metrics are towards the higher end of other sites.

374

375   Observed multiyear monthly mean v_d is similar year-round except during March and April when values are lower (Fig. 1). This

376   seasonal pattern is consistent across years except October–December. For example, observed v_d is high during October 2013,

377   low during November 2015, and high during December 2014. As discussed below, causes of high year-round values are

378   uncertain; this, together with strong interannual variability during fall, indicates a need for more years of observations at Ispra,

379   coupled with complementary measurements targeting individual pathways. Below, we focus on multiyear averages, after briefly

380   evaluating summertime interannual variability.

381

382   Summertime observed v_d is higher during 2014 than 2013 and 2015 (Fig. 1). Accordingly, model skill at interannual variability

383   should be determined by whether models capture much higher summertime average during 2014 vs. other years. Figure 13 shows

384   that some models suggest that v_d should be highest during 2014, but hardly any models capture the large observed relative

385   difference between this year and other years. The exception is MLC-CHEM, and to a lesser extent GEM-MACH Zhang. Thus,

386   most models have little skill at simulating summertime interannual variability at Ispra.

387

388   The v_d seasonality shape is a clear discrepancy between observations and models. In contrast to observations, central models' v_d

389   peaks during warm months (Fig. 2). Models show similar v_d relative seasonal amplitudes, aside from GEM-MACH Wesely,

390   relative to other forests (Fig. 9). Central models bracket observations during April–September, but models show a low bias

391   during October–March. Relative summertime and springtime biases range from -33% to +32% except DO₃SE multi, TEMIR

392   Zhang, TEMIR Wesely BB, and GEM-MACH Zhang (lower) as well as GEM-MACH Wesely (higher) (Fig. 4). Relative

393   wintertime and fall biases range from -22% to -89% across models. Ispra is the only site besides Auchencorth Moss where

394   models are biased in the same direction for an extended period (i.e., longer than three months).

395

396   Models show that stomatal uptake largely drives v_d seasonality (Fig. 6). Models simulate contributions from cuticular uptake,

397   mostly via positive correlations with the stomatal pathway. Models with non-zero individual contributions from cuticular uptake

398   (GEM-MACH Zhang, CMAQ models, and DO₃SE models) are the same as Harvard Forest and Borden Forest. Models show v_d

399   maxima during warm months because v_d strongly depends on LAI (Fig. 7), which has a broad maximum during warm months

400   (Fig. 10). Specifically, simulated v_d tends to increase with LAI, which contrasts with observed v_d.

401

402   A couple of models deviate from the majority in terms of v_d seasonal cycles (Fig. 3). For example, GEM-MACH Zhang is low

403   during warm months and GEM-MACH Wesely is very high during warm months. WRF-Chem Wesely shows higher wintertime

404   v_d than other models, especially January–March, due to high soil uptake, as well as high early-springtime uptake due to

405   combined high soil and stomatal uptake (Figs. 5, 10). GEM-MACH Wesely and WRF-Chem Wesely are two of three models

406   with input initial resistances (i.e., model parameters) varying by season, which likely causes these models to produce distinct

407   seasonal cycle shapes. GEM-MACH Zhang has low summertime stomatal and nonstomatal uptake, compared to the rest (Fig. 5).

408

409   Even though central models bracket observed multiyear monthly mean v_d during April–September (Fig. 2), and many individual

410   models capture the increase from April to May, individual models fail to capture that July–September values should be roughly

411   constant, rather than decrease (Fig. 3). For example, some models (including DO₃SE psn, MLC-CHEM) simulate April-July

412   multiyear monthly mean v_d very well but not August and September when they are low (because they simulate decreases from

413   early to late summer). Models may erroneously simulate decreases from early to late summer because they depend too strongly

414   on *LAI*, which weakly declines from July to September, or soil moisture.

415

416   During summer, the model spread is largest for stomatal uptake relative to other pathways (Fig. 11). Models simulate substantial

417   stomatal uptake, with DO₃SE multi and GEM-MACH Zhang simulating the lowest (but nonnegligible) values (Fig. 5). The

418   highest stomatal uptake is simulated by GEM-MACH Wesely, GEOS-Chem Wesely, IFS GEOS-Chem Wesely, IFS SUMO

419   Wesely, TEMIR Wesely, and MLC-CHEM. Central models show stomatal fractions of 50% to 77.5%, but the full model range is

420   37.5% to 87.5% (Fig. 12). The model spread across pathways is second largest for cuticular uptake. Soil uptake is very low

421   across models except WRF-Chem Wesely as well as CMAQ STAGE and GEM-MACH Wesely where it is higher. The ranking

422   and spread across pathways of pathways' standard deviations at Ispra is very similar to Borden Forest and Harvard Forest, but

423   not Hyytiälä. Given that central models capture the average magnitude of warm-season v_d well but disagree mainly on stomatal

424   vs. cuticular fractions as well as monthly changes within the warm season (or lack thereof), future work should prioritize using

425   observational constraints on stomatal uptake to further evaluate model performance.

426

427   During winter, simulated v_d tends not to be dominated by one pathway; instead, there are small contributions from 2–4 pathways

428   (Fig. 5). Exceptions are WRF-Chem Wesely where soil uptake dominates and a few models where cuticular uptake tends to

429   dominate (e.g., CMAQ STAGE, CMAQ M3Dry, DO₃SE multi). The model spread in soil uptake is largest across pathways (Fig.

430   11), and high WRF-Chem Wesely values play a role in this. Otherwise, soil uptake is low, or in a few cases moderately low (e.g.,

431   MLC-CHEM, IFS SUMO Wesely). Cuticular uptake is close behind soil uptake in terms of the spread. Stomatal fractions span

432   0% to 47.5%, with the largest range across central models (10–45%) across sites (Fig. 12). Eleven models show low-to-

433   moderately-low stomatal uptake, but others predict none (GEM-MACH Wesely, GEM-MACH Zhang, CMAQ STAGE, GEOS-

434   Chem Wesely, CMAQ M3Dry, TEMIR Wesely, DO₃SE multi). More models predict non-zero stomatal uptake at Ispra

435   compared to other sites, apart from Ramat Hanadiv. Whether simulated wintertime stomatal, cuticular, soil, and/or lower canopy

436   uptake should be higher at Ispra is uncertain. There may also be fast ambient losses of ozone. Ispra does not have snow depth

437   observations, but we anticipate that accounting for snow would not substantially change model results. Future attention should be

438   placed elsewhere with respect to better understanding of large wintertime model biases. A key first step is to understand whether

439   there is stomatal uptake during winter, and then what its magnitude is.

440   **5.6 Hyytiälä**

441   Hyytiälä is a boreal evergreen needleleaf forest in Finland. The model spread in terms of the model with the highest annual average

442   v_d divided by the model with the lowest is 2.7 (1.9 during summer and 21 during winter) but based on the interquartile range is 1.6

443 (1.4 during summer and 2.4 during winter). The metrics of model spread at Hyytiälä are at the higher end of other sites' values,

444 especially for annual and winter values.

445

446 Observed multiyear monthly mean v_d maximizes during warm months, and this is consistent across years (Fig. 1). Most models

447 simulate higher values during warm months relative to cool months (Fig. 3). Outliers with respect to the seasonality are TEMIR

448 Zhang (strong overestimate during cold months leading to near constant values year-round), GEM-MACH Wesely (strong

449 overestimate during warm months), GEOS-Chem Wesely and TEMIR Wesely (overestimate during summer), and WRF-Chem

450 Wesely (strongly overestimate during early spring). Here we examine observed relative seasonal amplitude for v_d because

451 observed and (most) modeled values have warm-month maxima and cool-month minima as well full seasonal cycles, allowing

452 meaningful comparisons. The observed relative seasonal amplitude falls within the central models' range, but towards the upper

453 end, and most models predict too-low values (Fig. 9).

454

455 In general, the largest relative model v_d biases at Hyytiälä occur during cool months (Fig. 4) and the wintertime v_d model spread is

456 the highest relative to other sites (Fig. 11), implying that wintertime v_d at this site is a key uncertainty. Wintertime relative biases range

457 from -81% to +87% except for a few models that have much higher positive biases: GEM-MACH Zhang (+307%), TEMIR Zhang

458 models (+211 to +245%), and DO$_3$SE psn (+104%). However, most models are biased high, apart from IFS SUMO Wesely (-5%), IFS

459 GEOS-Chem Wesely (-81%), GEOS-Chem Wesely (-62%), and TEMIR Wesely models (-15% to -57%). Models largely simulate that

460 cuticular and soil uptake are dominant contributors (Fig. 5). Most models simulate near-zero wintertime stomatal uptake, despite

461 relatively high *LAI* (Fig. 10), implying that models have at least rudimentary skill at capturing the seasonality of evergreen vegetation.

462 Central models show stomatal fractions between 0% and 12.5%, but a few models show contributions of 17.5% to 50% (Fig. 12). The

463 model with the 50% (TEMIR Wesely BB) in addition to very low stomatal uptake has very low nonstomatal uptake.

464

465 During winter, models also show differences in partitioning and magnitudes of cuticular vs. soil uptake (Fig. 5). The model spread in

466 cuticular uptake is larger than soil uptake (Fig. 11) – Hyytiälä is the only site where this happens – presumably because *LAI* remains

467 relatively high at this site year-round and models seem to suggest that cuticular uptake is more important than ground uptake at forests.

468 Ten models show substantial cuticular uptake, whereas only two models show low cuticular uptake, and the rest show none. Seven

469 models show substantial soil uptake, while ten show very little to none. Models showing high vs. low cuticular and soil uptake are

470 sometimes the same. For example, four simulate substantial cuticular uptake and soil uptake, and five simulate minimal cuticular uptake

471 and soil uptake. In the former case, models overestimate wintertime v_d; in the latter, models underestimate it. Most models capture small

472 observed decreases in wintertime v_d with snow, but the spread across models during snow and snow-free periods is very large (Fig. 8).

473 Thus, attention should focus on constraining wintertime cuticular vs. soil uptake. Establishing whether there is cuticular and/or soil uptake

474 during winter is an important first step towards narrowing model uncertainties.

475

476   Within the warm season, whether models show pronounced v_d seasonality varies (Fig. 3). Models also do not capture that

477   observations maximize during August and minimize during March (Fig. 2). Specifically, models tend to overestimate late-winter/spring

478   v_d while underestimating fall/early-winter v_d, as indicated by comparing the interquartile range to observations. Multiyear monthly

479   mean *LAI* peaks during August (around 3.75 m^2 m^{-2}), after an increase from May (Fig. 10). Then, *LAI* decreases to November,

480   and is constant from November to May (around 2.75 m^2 m^{-2}). Models bound the observed v_d-*LAI* relationship, and largely

481   capture the increase from 3 to 3.5 m^2 m^{-2} (Fig. 7). However, most models do not capture the v_d change from 3.5 to 3.75 m^2 m^{-2}

482   where observations suggest that the slope should be the same as for 3 to 3.5 m^2 m^{-2} (instead models suggest decreases). Models also

483   overestimate the increase from 2.75 to 3 m^2 m^{-2}. Some effect overrides *LAI*'s influence on seasonality in stomatal uptake in models,

484   given that both observed *LAI* and v_d peak during August, but simulated stomatal uptake and v_d do not. Simulated declines with soil

485   moisture may play a role here.

486

487   Models simulate that stomatal uptake and co-variations between pathways are important seasonality drivers (Fig. 6). Only two models

488   suggest that there are not individual contributions by stomatal uptake (GEM-MACH Wesely, GEM-MACH Zhang), but a number of

489   models suggest that the sum of individual contributions from other pathways and co-variations are at least as important as stomatal

490   uptake. There are similarly evenly distributed spreads across models in terms of relative seasonal amplitudes for stomatal uptake and v_d

491   (Fig. 9). Most models' stomatal uptake seasonal cycles show a broad warm-season peak, apart from some models with more pronounced

492   seasonality during warm months (e.g., GEM-MACH Wesely, GEOS-Chem Wesely, TEMIR Wesely, CMAQ M3Dry models) (Fig. 10).

493   IFS SUMO Wesely peaks during May and then declines afterwards. Model outliers in terms of high magnitudes of summertime stomatal

494   uptake include GEOS-Chem Wesely, TEMIR Wesely, MLC-CHEM, and GEM-MACH Wesely.

495

496   During summer, relative model biases range from -14% to +20% except for GEM-MACH Wesely (+88%), IFS SUMO Wesely (-25%),

497   WRF-Chem Wesely (+32%), TEMIR Wesely (+34%), and GEOS-Chem Wesely (+40%) (Fig. 4). Models show substantial stomatal

498   uptake (Fig. 5) with stomatal fractions spanning 27.5% to 80% (Fig. 12). Central models show 42.5–65%. Models that simulate lower

499   canopy uptake show low uptake via this pathway, like other forests. The largest model spread is for soil and stomatal uptake, but closely

500   followed by cuticular uptake (Fig. 11), which is distinct from other forests. Soil uptakes' high model spread is due to large estimates from

501   WRF-Chem Wesely and GEM-MACH Wesely and zero soil uptake from DO$_3$SE models; other models simulate more similar estimates

502   of soil uptake, ranging from low to moderate values. Models show cuticular uptake but disagree as to whether it is low or moderate.

503   Observational constraints on stomatal uptake will help to further narrow uncertainties as to the magnitude and relative

504   contribution of summertime stomatal uptake, as well as changes on weekly to monthly timescales.

505

506   Key findings regarding seasonality at Hyytiälä include: models struggle to capture the exact timing of maximum and minimum values,

507   overestimate wintertime values and thus underestimate the relative seasonal amplitude, and disagree about seasonality within the warm

508   season, while generally capturing that there should higher values during warm months. Silva et al. (2019) use Hyytiälä observations to

509   train a machine learning model and apply the model to predict v_d at Harvard Forest, finding that their model predicts a late summertime

510   peak in v_d, which is observed at Hyytiälä but not at Harvard Forest. Assuming that differences between these two sites are characteristic

511   of sites' broad LULC classifications, both our findings and theirs suggest a need for improved predictive ability of seasonality differences

512   between coniferous vs. deciduous forests.

513

514   Thus far we discuss multiyear averages at Hyytiälä. We turn to summertime interannual variability. Models do not capture the

515   summertime ranking across years (Fig. 13). Several models predict particularly low (high) v_d during some summers, but these are not

516   low (high) summers in the observations. Some models are close to capturing the degree of summertime interannual variability, but

517   typically these models show a more uneven distribution across years than suggested by observations. Notably, models show more

518   variability in their year-to-year rankings at Hyytiälä compared to other sites with longer records. Nonetheless, we conclude that model

519   skill is poor at this site in terms of interannual variability.

520   **5.7 Harvard Forest**

521   Harvard Forest is a temperate mixed forest in the northeastern United States. The model spread in terms of the model with the highest

522   annual average v_d divided by the model with the lowest is 1.9 (1.8 during summer and 4.8 during winter) but based on the

523   interquartile range is 1.2 (1.4 during summer and 2.6 during winter). Like other forests, the wintertime spread is largest. Aside

524   from winter values, the metrics of the spread at Harvard Forest are on the lower end of estimates across sites.

525

526   Observed multiyear monthly mean v_d maximizes during May–September (Fig. 1). Observed seasonal cycles vary across years, but

527   values are generally higher during warmer vs. cooler months across years. We focus on multiyear averages until the subsection end,

528   where we touch on summertime interannual variability. Models capture that v_d peaks during warm months (Fig. 2). The exception is

529   GEM-MACH Zhang, which has similar monthly averages year-round. Despite capturing seasonality shape, models overestimate the

530   relative seasonal amplitude (Fig. 9), apart from GEM-MACH Zhang, TEMIR Zhang, and TEMIR Zhang BB (substantial underestimate)

531   as well as DO₃SE psn (slight underestimate). Outliers show high wintertime v_d relative to other models and observations, implying that

532   models bound the observed relative seasonal amplitude does not necessarily indicate ensemble skill.

533

534   Models are within $\pm 65\%$ of observed values across seasons (Fig. 4). Exceptions occur during spring and summer for GEM-MACH

535   Wesely, winter and spring for GEM-MACH Zhang, and spring for WRF-CHEM Wesely and TEMIR Zhang Medlyn. Central models

536   bracket observations well. Specifically, observations fall in the lower end of the spread during warm months and the upper end during

537   November–January, but otherwise are in the middle of the spread. Across models, summertime biases are positive, ranging from +4 to

538   +144%, except IFS GEOS-CHEM Wesely (-4%) and TEMIR Zhang (-2%). Thus, overestimated relative seasonal amplitudes (Fig. 9) are

539   likely due to high summertime v_d. Previous work suggests that GEOS-Chem's overestimate at Harvard Forest is due to too-high model

540   *LAI* (Silva and Heald, 2018), but clearly there is another issue because models are forced with site-specific *LAI*. Most models tend to

541   underestimate v_d at low *LAI* and overestimate v_d at high LAI, overstating v_d increases with *LAI* (Fig. 7).

542

543 During winter, model biases tend to be negative, ranging from -24% to -71%, with exceptions of GEM-MACH Wesely (+85%), TEMIR

544 Zhang models (+25% to +33%), and MLC-CHEM (+13%) as well as two models with very low negative biases (DO₃SE psn and WRC

545 Chem Wesely) (Fig. 4). The wintertime model spread is highest for soil uptake across pathways, with cuticular uptake close behind. Soil

546 uptake is always at least 37.5% (and up to 70%) of v_d except for GEM-MACH Wesely (20%) (Fig. 5). Most models show little-to-no

547 stomatal uptake, but some models show nonnegligible values. Central models show stomatal fractions of 5–15% (Fig. 12). Estimates for

548 cuticular uptake vary – across models, there are substantial, small, and negligible contributions. Lower canopy uptake is low for models

549 that simulate this pathway but can be an important fraction of v_d. There are no snow depth observations at Harvard Forest. Assuming no

550 snow throughout may influence some models' ability to estimate wintertime v_d well. However, based on our analysis at other sites, we

551 do not anticipate the lack of snow data to be the main driver of model-observation or model-to-model differences. Establishing whether

552 there should be stomatal or cuticular uptake during winter would be a useful first step in further constraining models. Otherwise, attention

553 should focus on narrowing uncertainties related to wintertime ground uptake.

554

555 Some models capture the broad observed v_d maximum during the warm season while others show more seasonality within the warm

556 season (Fig. 3). A few models show pronounced declines after July (e.g., MLC-CHEM, TEMIR psn). Pronounced declines after July do

557 not occur in observed multiyear monthly averages but occur during several individual years (Fig. 1). Simulated pronounced declines may

558 follow these models' soil moisture dependencies (note that not all models have soil moisture dependencies, and there are differences

559 among models that do have them). That models with soil moisture dependencies are not capturing the observed multiyear mean

560 seasonality may be due to soil moisture dependencies themselves, and/or with uncertainty in soil moisture input. For example, soil

561 moisture was not measured during all years with ozone fluxes at Harvard Forest, and thus we use a climatological average during those

562 years. Future work should examine seasonality during individual years, paying attention to years with climatological average vs. year-

563 specific input soil moisture, to determine model strengths and limitations.

564

565 Models show stomatal uptake is an important driver of v_d seasonality (Fig. 6). Six models estimate that stomatal uptake largely drives

566 seasonality, with some contributions from correlations (mainly positive correlations between stomatal and cuticular pathways). The rest

567 estimate moderate contributions from stomatal uptake, but at least as much of an influence from individual nonstomatal pathways or

568 correlations (positive or negative). Models show a clear seasonality to stomatal uptake, with a peak during warm months and zero or near

569 zero values during winter (Fig. 10). The spread for relative seasonal amplitude for stomatal uptake across central models is the smallest

570 across sites (Fig. 9). Six models deviate from the rest, however. CMAQ M3Dry, CMAQ STAGE, and GEM-MACH Wesely have high

571 relative seasonal amplitudes for stomatal uptake, GEM-MACH Zhang, IFS SUMO Wesely, and DO₃SE psn have low values. In contrast,

572 the spread for relative seasonal amplitude for v_d has a more even distribution across models. Thus, while there is a fair amount of

573 agreement across models in terms of seasonality in stomatal uptake, models disagree as to nonstomatal uptake seasonality and its role on

574 v_d seasonality. Together with findings that models exaggerate the v_d-LAI relationship and most models overestimate the relative

575 seasonal amplitude for v_d, this result implies future work should aim to better constrain nonstomatal influences on seasonality.

576

577 During summer, the model spread is highest for stomatal uptake, with cuticular uptake close behind (Fig. 11). Models show substantial

578 contributions from stomatal uptake -- the model range spans 30% to 80%, but the central models' range spans 50% to 70% (Fig. 12).

579 Estimates for cuticular uptake vary (Fig. 5) – across models, there are substantial, moderate, and low contributions. Soil uptake is low,

580 except for WRF-Chem Wesely and GEM-MACH Wesely. Lower canopy uptake is low for models that simulate this pathway, like

581 other forests. Observational constraints on stomatal uptake will help to further narrow model uncertainties as to magnitude and

582 relative contribution of summertime stomatal uptake.

583

584 Interannual variability is strong across months (Fig. 1). A series of papers pointed this out for daytime values and investigated

585 drivers during summer (Clifton et al., 2017, 2019). Models capture neither the large observed spread across years during summer

586 nor the ranking of years (Fig. 13). Most models simulate that some of the highest summers observed are low v_d summers.

587 Previous work points to nonstomatal pathways driving summertime interannual variability (Clifton et al., 2017, 2019), and thus

588 models may be lacking in their ability to simulate the degree to which nonstomatal uptake varies from year to year, and likely

589 key process dependencies.

590 **5.8 Borden Forest**

591 Borden Forest is a mixed forest in the boreal-temperate transition zone in Canada. The model spread in terms of the model with the

592 highest annual average v_d divided by the model with the lowest is 2.3 (3.4 during summer and 10 during winter) but based on the

593 interquartile range is 1.4 (1.8 during summer and 3 during winter). The metrics of model spread are towards the higher end of

594 other sites, except for winter and the summertime interquartile range when they are the highest.

595

596 Observed multiyear monthly mean v_d shows a broad maximum during warm months at Borden Forest (Fig. 1), like Harvard

597 Forest and Hyytiälä. However, uniquely, observations at Borden Forest show particularly large winter vs. summer differences and steep

598 changes during spring and fall. Specifically, v_d increases from March to June by 0.5 cm s^{-1}. Then, v_d remains high from June to

599 September (0.6–0.65 cm s^{-1}) and declines steeply from September to November. Models simulate higher v_d during warmer vs.

600 cooler months (Figs. 2, 3), and the observed relative seasonal amplitude lies close to the middle of the central models' spread

601 (Fig. 9). However, there is a clear discrepancy between models and observations in that models do not capture very high v_d

602 across warm months (Fig. 3). All models except GEM-MACH Wesely have low summertime biases, with a range from -15% to -

603 74% (Fig. 4). In general, high observed v_d during warm months at Borden Forest needs better understanding, given uncertainty in ozone

604 flux measurements from the gradient technique (see discussion in Sect. 3.2).

605

606 The individual contribution from stomatal uptake is a key driver of v_d seasonality, apart from IFS SUMO Wesely, CMAQ

607 STAGE, and DO₃SE models (Fig. 6). These four models do, however, show stomatal contributions to seasonality via correlations

608 with other pathways. Notably, there are more individual nonstomatal contributions to seasonality at Borden Forest than other

609 forests. There are also a variety of simulated v_d seasonal cycle shapes at Borden Forest, in contrast to Harvard Forest and Ispra.

610 Some models simulate weak changes from cooler to warm months (DO₃SE models, TEMIR Zhang models, IFS SUMO Wesely,

611 GEM-MACH Zhang) while others simulate moderate changes (WRF-Chem Wesely, MLC-CHEM, CMAQ STAGE) or strong

612 changes (GEOS-Chem Wesely, TEMIR Wesely, IFS GEOS-Chem Wesely, GEM-MACH Wesely, CMAQ M3Dry models,

613 TEMIR Wesely psn). TEMIR psn simulate erratic monthly changes during June to October. Generally, models with the strongest

614 changes from cooler to warm months simulate that stomatal uptake predominately drives v_d seasonality (Fig. 6). Conversely,

615 models with weak changes from cooler to warm months indicate that nonstomatal pathways contribute more predominantly.

616

617 With respect to the relationship between multiyear monthly mean v_d and LAI, observed v_d increases with LAI but the slope varies

618 (Fig. 7). The observed slope is strongest for 0.5 to 1 m^2 m^{-2}, and models tend to underestimate this change, but do simulate increases.

619 Then, the observed slope weakens but remains positive for 1 to 2 m^2 m^{-2} – most models suggest decreases instead. Then, the

620 observed slope weakens even further above 2 m^2 m^{-2}. Some models capture the slope of LAI increases above 2 m^2 m^{-2} but others

621 exaggerate it (e.g., GEM-MACH Wesely, GEOS-Chem Wesely, TEMIR Wesely, CMAQ M3Dry models). The main issue is that

622 individual models tend not to capture that there should be relatively high v_d during May and October (Fig. 3). Specifically,

623 models simulate a later spring onset to higher v_d as well as an earlier fall decline, and thus a shorter season of elevated v_d than

624 observed. We thus suggest that models are too strongly tied to LAI, which strongly increases from May to June and strongly

625 decreases from September to October (Fig. 10).

626

627 Additionally, many models do not capture that multiyear monthly mean v_d is similar during June–September (Fig. 3). Some

628 models simulate declines from August to September (e.g., CMAQ M3Dry-psn, GEOS-Chem Wesely, TEMIR Wesely, GEM-

629 MACH Wesely). A weak decline from August to September occurs in the observed multiyear average (the strong decline

630 happens from September to November); some models capture the August-to-September decline's magnitude while others

631 exaggerate it. Some models show low values during July (e.g., TEMIR psn), in addition to August-to-September declines.

632 Observations show low values during July not in multiyear monthly mean seasonal cycles, but during 2012 and perhaps 2008

633 (Fig. 1). Many models show peak v_d during June. Again, this does not happen in observed multiyear monthly averages, but

634 occurs in 2010. Thus, models may exaggerate depositional responses (in particular, stomatal) to changes in environmental conditions

635 (e.g., soil moisture) on a climatological basis but have some skill in certain years.

636

637 During summer, the largest model spread across pathways occurs for stomatal uptake, followed by cuticular uptake and then soil

638 uptake (Fig. 11), similar to Harvard Forest and Ispra. Models show substantial stomatal uptake, apart from two with very low

639 values (IFS SUMO Wesely and DO₃SE multi). Stomatal fractions range from 20% to 80% across models, but 40% to 62.5%

640 across central models (Fig. 12). Eight models simulate lower cuticular uptake, while the rest simulate higher cuticular uptake

641 (Fig. 5). Models with lower canopy uptake show low cuticular uptake, with two exceptions: GEM-MACH Wesely, which has

642 high cuticular uptake, and MLC-CHEM, which does not archive lower canopy uptake diagnostic but has low cuticular uptake.

643 Most models simulate low soil uptake, but a few models simulate moderate-to-high soil uptake (GEM-MACH Wesely, GEM-

644   MACH Zhang, CMAQ STAGE, WRF-Chem Wesely, and MLC-CHEM). Observational constraints on stomatal uptake will help
645   to further narrow model uncertainties as to the magnitude and relative contribution of stomatal uptake.
646
647   During winter, models show a mixture of over- and under-estimates. Models with overestimates are TEMIR Zhang models (+68
648   to +73%), GEM-MACH Zhang (+124%), WRF-Chem Wesely (+13%), DO$_3$SE multi (+9%) and DO$_3$SE psn (+44%). Otherwise,
649   underestimates span -20% to -78%. Models with high v_d simulate high cuticular uptake, generally high soil uptake, and in one
650   case nonnegligible stomatal uptake (DO$_3$SE psn) (Fig. 5). Soil and cuticular uptake show the highest spreads across models, with
651   soil uptake the highest, similar to Harvard Forest and Ispra (Fig. 11). Central models show very low stomatal fractions, but
652   outliers span 10% to 30% (Fig. 12). Apart from DOS$_3$E psn, high stomatal fractions are due to high nonstomatal uptake, rather
653   than high stomatal uptake. Many models largely capture that observations show no v_d change with snow, although some slightly
654   overestimate the change. Thus, the primary issue with wintertime model biases is likely unrelated to responses to snow, and
655   rather related to mischaracterized magnitudes of pathways or responses to other environmental conditions.
656
657   In terms of summertime v_d interannual variability, some models underestimate the relative spread across years (Fig. 13), but
658   some only slightly underestimate it (IFS SUMO Wesely, CMAQ STAGE, TEMIR Zhang, MLC-CHEM, DO$_3$SE models) and a
659   few exaggerate it (TEMIR psn). Models generally struggle to capture the observed relative distribution across summers (i.e., two
660   high years, two low years, and one middle year). No model captures the year-to-year ranking across summers but many can
661   simulate that one of the highest years is a high v_d summer and in some cases that one of the lowest years is a low v_d summer.
662   CMAQ STAGE captures that the other high year is a high year, whereas no other model captures this (or distinguish it from
663   other years). Figure 1 shows that one year has particularly low v_d during August, and that there is a separation between some
664   years relative to others during June (three low years vs. two high years). Future work should examine interannual variability in
665   monthly averages to further establish model skill.

666   **6 Conclusion**
667   We introduce AQMEII4 Activity 2 for intercomparison and evaluation of eighteen dry deposition schemes configured as single-
668   point models at eight sites with ozone flux records, driven by the same set of meteorological and environmental conditions. We
669   provide our approach's rationale, document the single-point models, and describe the observational datasets used to drive and
670   evaluate the models. The design of Activity 2 allows us to focus on parametric and process uncertainty. We launch Activity 2
671   results by analyzing simulated multiyear mean ozone deposition velocities and effective conductances, as well as observed
672   multiyear mean ozone deposition velocities. Our focus is on monthly and seasonal averages across all hours of the day, apart
673   from one site for which we examine afternoon averages (Ramat Hanadiv). We evaluate simulated magnitudes and seasonal
674   cycles (e.g., shape, amplitude) of ozone deposition velocities against observations, and identify how differences and similarities
675   in relative and absolute contributions of individual deposition pathways and some dependencies on environmental conditions
676   influence the model spread and comparison with observations.

677

678 There are a variety of observed climatological seasonal patterns and magnitudes of ozone deposition velocities across sites. We
679 emphasize incomplete understanding of observed variations at several sites. Namely, there are unexpectedly high ozone
680 deposition velocities year-round at Auchencorth Moss, during the cool season at Ispra, and during the warm season at Borden
681 Forest; models do not capture these high values. Further model evaluation at these sites requires better understanding of the
682 observations. We emphasize that our measurement testbed is likely insufficient to generalize results to specific LULC types, so
683 we focus on site-specific results. We also cannot discount the fact that differences in ozone flux methods and instrumentation and
684 a lack of coordinated processing protocols across data sets limit meaningful synthesis of our results across sites. However, given
685 that key processes and parameters are strongly tied to LULC type in dry deposition parameterizations, a core question is whether
686 the magnitude and dependencies of ozone deposition velocities can be described from a LULC-type perspective. To address this
687 question, future work will need to better understand observed site-to-site differences in ozone deposition velocities, which likely
688 requires new multiscale ozone flux datasets.

689

690 Observed interannual variation in ozone deposition velocities is strong at most sites examined here, demonstrating the
691 importance of long-term ozone flux records for model evaluation. For example, even if a model captures values for a given year,
692 the model may not reproduce interannual variability or the multiyear average. Our focus is climatological evaluation, with the
693 caveat that three sites (Ramat Hanadiv, Auchencorth Moss, and Bugacpuszta) do not have multiple years of data for several
694 months and two are missing some months of data across all years. Of course, full annual records with several years of data are
695 required for confident constraints on climatological seasonality. Nonetheless, sites with short-term records have very similar
696 monthly averages between years when there is good data coverage, with only a few exceptions (October at Auchencorth Moss
697 and fall at Ispra), implying some utility of these datasets towards our aim.

698

699 For sites with more than three summers of data, we identify whether models capture the ranking and spread across summers. We
700 find that models do not capture observed summertime interannual variability, a finding that agrees with earlier work with one
701 model at Harvard Forest (Clifton et al., 2017). Our work here shows that the issue is widespread across models and sites.
702 Specifically, we show poor model skill in simulating the degree of the interannual spread as well as the ranking across years.

703

704 Individual model performance strongly varies by season and site. Throughout the manuscript, we examine individual models as
705 well as model ensembles including the full set of models as well as the interquartile range, which helps us to narrow our focus to
706 key common uncertainties across models. The interquartile range across simulated averages ranges from a factor of 1.2 to 1.9
707 annually across sites, and largely reasonably bounds multiyear monthly mean ozone deposition velocities. Exceptions to the
708 latter are times denoted as particularly uncertain at Auchencorth Moss, Ispra, and Borden Forest, in addition to late summer at
709 Bugacpuszta and Ramat Hanadiv. The latter finding, together with our finding that many models that include soil moisture
710 dependencies on stomatal conductance exaggerate late-summer decreases in ozone deposition velocities at forests, suggests a
711 need to focus on refining soil moisture dependencies. Such work should probe interannual variability and seasonality with

712 additional observational constraints on stomatal uptake in the context of uncertainty in soil moisture input data. In general, in

713 some cases, gaps in site-specific measurement data (e.g., soil moisture and characteristics) forced us to make assumptions or

714 derive estimates for key model variables and parameters. This may influence model performance, and points to a need for a

715 standard minimum set of observations at future field studies.

716

717 Even beyond differing effects of soil moisture across the ensemble of models, there are differences in simulated seasonal cycle

718 shapes of ozone deposition velocities. Models that rely strongly on seasonally dependent parameters are often identified as

719 outliers, so we recommend that related canopy resistance equations should be tied to variables like leaf area index instead of only

720 seasonally varying parameters. In principle, seasonally varying parameters are not problematic, but a challenge seems to be

721 indicating site-specific phenology accurately. At half the sites, the model spread is highest during cooler months, implying a

722 need to better understanding of wintertime deposition processes. Strong wintertime sensitivities of tropospheric ozone

723 abundances in regional-to-global chemical transport models (Helmig et al., 2007; Matichuk et al., 2017; Clifton et al., 2020b)

724 also point to this need. By compositing observed and simulated ozone deposition velocities for all vs. snowy conditions during

725 cool months at sites with snow depth observations, we show that models' inability to capture the magnitude of wintertime values

726 generally is a larger issue than models' inability to capturing responses to snow. While our analysis suggests that snow-induced

727 changes are not the main driver of observed seasonality in ozone deposition velocities, we also find models may too strongly rely

728 on leaf area index to determine seasonality.

729

730 Several papers illustrate challenges in determining which ozone dry deposition parameterization is best given observations

731 compiled from the literature (Wong et al., 2019; Cao et al., 2022; Sun et al., 2022) or comparing seasonal differences for ozone

732 and sulfur dioxide deposition velocities at Borden Forest (Wu et al., 2018). While we agree with these earlier findings with our

733 completer and more diverse testbed, we take the evaluation a step further by pinpointing how different pathways contribute to the

734 spread. In general, both stomatal and nonstomatal pathways are key drivers of variability in ozone deposition velocities across

735 models. Additionally, in some cases, ozone deposition velocities are similar across models when the partitioning among

736 deposition pathways is very different (i.e., similar results for different reasons).

737

738 For the most part, models simulate that stomatal uptake predominately drives seasonality in ozone deposition velocities. Like

739 large model differences in seasonality of ozone deposition velocities, there are large model differences in seasonality of stomatal

740 uptake. A few models show that seasonality in nonstomatal uptake terms is also important for seasonality in ozone deposition

741 velocities. Across sites, both stomatal and nonstomatal pathways are important contributors to ozone deposition velocities during

742 the growing season. For example, during summer, the median of the stomatal fraction of the ozone deposition velocity across

743 models ranges from 30% to 55% across most sites. Thus, like observationally based estimates of stomatal fraction over

744 physiologically active vegetation compiled by a recent review (Clifton et al., 2020a), models clearly indicate a codominant role

745 for dry deposition through nonstomatal pathways. Nonetheless, as stated in the previous paragraph, we emphasize large

746 differences in simulated nonstomatal uptake, in addition to stomatal uptake, across models.

747

748   In general, we confirm here with our unprecedented full documentation of eighteen dry deposition

749   schemes, especially nonstomatal deposition pathways, are highly empirical. While some schemes can capture some of the salient

750   features of observations and schemes could be adjusted to better capture the magnitude of observed ozone deposition velocities

751   at the sites examined here, better mechanistic understanding of observed variability, and a firm grasp on how different deposition

752   pathways change in time and space on different scales, are needed to improve predictive ability of ozone dry deposition. We will

753   continue to chip away at this problem; next for Activity 2 will be to leverage observation-based constraints on stomatal

754   conductance, together with inferred stomatal fractions of ozone deposition velocities, and examine diel, seasonal, and interannual

755   variations to further evaluate single-point models.

756   **Data Availability**

757   The hourly or half hourly observed ozone flux and forcing datasets are available to individuals wishing to participate in this

758   effort on a password-protected site managed by the U.S. EPA, subject to the individual's agreement that the people who created

759   and maintained the observation datasets are included in publications as the people see fit. Some datasets are already available

760   publicly, and in these cases, we have included the references to the datasets in the text.

761   **Author Contributions**

762   O. E. C. lead the manuscript's direction and writing, data processing and analysis, and coordination among authors. D. S. and C.

763   H. contributed to the manuscript's direction, data processing, and coordination among authors. J. O. B. contributed CMAQ

764   STAGE results and documentation. S. B. contributed DO$_3$SE results and documentation. P. C. contributed GEM-MACH results

765   and documentation. M. C. contributed data from Easter Bush and Auchencorth Moss. L. E. contributed DO$_3$SE results and

766   documentation and assisted with direction. J. F. contributed IFS results and documentation and assisted with direction. E. F.

767   contributed data from Ramat Hanadiv. S. G. assisted with direction. L. G. contributed MLC-CHEM results and documentation.

768   O. G. contributed data from Ispra. C. D. H. assisted with direction and contributed GEOS-Chem results and documentation. I. G.

769   contributed data from Ispra. L. H. contributed data from Bugacpuszta. V. H. contributed model results and documentation from

770   IFS. Q. L. contributed data from Ramat Hanadiv. P. A. M. contributed model results and documentation from GEM-MACH and

771   assisted with direction. I. M. contributed data from Hyytiälä. G. M. contributed data from Ispra. J. W. M. contributed data from

772   Harvard Forest. J. L. P. C. contributed WRF-Chem results and documentation. J. P. contributed M3Dry results and

773   documentation. L. R. contributed M3Dry results and documentation. R. S. J. contributed WRF-Chem results and documentation.

774   R. S. contributed data from Borden Forest. S. J. S. assisted with data processing and assisted with direction. S. S. and A. P. K. T

775   contributed TEMIR results and documentation. E. T. contributed data from Ramat Hanadiv. T. V. contributed data from

776   Hyytiälä. T. W. contributed data from Bugacpuszta. Z. W. and L. Z. contributed data from Borden Forest. All authors

777   contributed to manuscript writing and useful discussions on data analysis and processing and results.

797 **Competing Interests**
798 None

799   **References**

800   Abramoff, R., and Finzi, A: Phenology and Carbon Allocation of Roots at Harvard Forest 2011-2013 version 3, Environmental

801   Data Initiative, https://doi.org/10.6073/pasta/b545e796e37ecdf11fd7ff1275b41a12, 2019.

802

803   Ainsworth, E. A., Yendrek, C. R., Sitch, S., Collins, W. J., and Emberson, L. D.: The effects of tropospheric ozone on net

804   primary productivity and implications for climate change, Annu. Rev. Plant Biol., 63(1), 637–661,

805   https://doi.org/10.1146/annurev-arplant-042110-103829, 2012.

806

807   Altimir, N., Kolari, P., Tuovinen, J.-P., Vesala, T., Bäck, J., Suni, T., Kulmala, M., and Hari, P.: Foliage surface ozone

808   deposition: A role for surface moisture?, Biogeosciences, 3, 209–228, https://doi.org/10.5194/bgd-2-1739-2005, 2006.

809

810   Anav, A., Proietti, C., Menut, L., Carnicelli, S., De Marco, A., and Paoletti, E.: Sensitivity of stomatal conductance to soil

811   moisture: implications for tropospheric ozone, Atmos. Chem. Phys., 18, 5747–5763, https://doi.org/10.5194/acp-18-5747-2018,

812   2018.

813

814   Andersson, C., and Engardt, M.: European ozone in a future climate: Importance of changes in dry deposition and isoprene

815   emissions, J. Geophys. Res., 115(D02303), https://doi.org/10.1029/2008JD011690, 2010.

816

817   Archibald, A. T., Neu, J. L., Elshorbany, Y. F., Cooper, O. R., Young, P. J., Akiyoshi, H., et al.: Tropospheric Ozone

818   Assessment Report: A critical review of changes in the tropospheric ozone burden and budget from 1850 to 2100, Elem. Sci.

819   Anth., 8, 1, https://doi.org/10.1525/elementa.2020.034, 2020.

820

821   Baldocchi, D. D., Hicks, B. B., and Camara, P.: A canopy stomatal resistance model for gaseous deposition to vegetated

822   surfaces, Atmos. Environ., 21, 91–101, https://doi.org/10.1016/0004-6981(87)90274-5, 1987.

823

824   Bales, R., Valdez, M., and Dawson, G.: Gaseous deposition to snow 2. Physical-chemical model for SO_2 deposition, J. Geophys.

825   Res., 92, 9789–9799, https://doi.org/10.1029/JD092iD08p09789, 1987.

826

827   Ball, M. C., Woodrow, I. E., and Berry, J. A.: A model predicting stomatal conductance and its contribution to the control of

828   photosynthesis under different environmental conditions, in Progress in Photosynthesis Research, edited by: Biggins, J.,

829   Martinus Nijhoff Publishers, Dordrecht, Netherlands, 221–224, https://doi.org/10.1007/978-94-017-0519-6, 1987.

830

831   Barford, C. C., Wofsy, S. C., Goulden, M. L., Munger, J. W., Pyle, E. H., Urbanski, S. P., Hutyra, L., Saleska, S. R., Fitzjarrald,

832   D., and Moore, K.: Factors controlling long- and short-term sequestration of atmospheric CO_2 in a mid-latitude forest, Science,

833   294, 1688–1691, https://doi.org/10.1126/science.1062962, 2001.

834

835   Baublitz, C. B., Fiore, A. M., Clifton, O. E., Mao, J., Li, J., Correa, G., Westervelt, D. M., Horowitz, L. W., Paulot, F., and

836   Williams, A. P.: Sensitivity of Tropospheric Ozone Over the Southeast USA to Dry Deposition, Geophys. Res. Lett., 47,

837   e2020GL087158, https://doi.org/10.1029/2020GL087158, 2020.

838

839   Beddows, A. V., Kitwiroon, N., Williams, M. L., and Beevers, S. D.: Emulation and sensitivity analysis of the community

840   multiscale air quality model for a UK Ozone pollution episode, Environ. Sci. Tech., 51(11), 6229–6236,

841   https://doi.org/10.1021/acs.est.6b05873, 2017.

842

843   Bela, M. M., Longo, K. M., Freitas, S. R., Moreira, D. S., Beck, V., Wofsy, S. C., Wiedemann, K., Andreae, M. O., and Artaxo,

844   P.: Ozone production and transport over the Amazon Basin during the dry-to-wet and wet-to-dry transition seasons, Atmos.

845   Chem. Phys., 15(2), 757–782, https://doi.org/10.5194/acp-15-757-2015, 2015.

846

847   Boose, E., and Gould, E.: Shaler Meteorological Station at Harvard Forest 1964–2002, Harvard Forest Data Archive: HF000,

848   https://doi.org/10.6073/pasta/84cf303ea3331fb47e8791aa61aa91b2, 1999.

849

850   Bonan, G. B., Lawrence, P. J., Oleson, K. W., Levis, S., Jung, M., Reichstein, M., Lawrence, D. M., and Swenson, S. C.:

851   Improving canopy processes in the Community Land Model version 4 (CLM4) using global flux fields empirically inferred from

852   FLUXNET data, J. Geophys. Res., 116, G02014, doi:10.1029/2010JG001593, 2011.

853

854   Brook, J., Zhang, L., Franco, D., and Padro, J.: Description and evaluation of a model of deposition velocities for routine

855   estimates of air pollutant dry deposition over North America, Part I: Model development, Atmos. Environ., 33, 5037–5051,

856   https://doi.org/10.1016/S1352-2310(99)00250-2, 1999.

857

858   Campbell, G. S., and Norman, J. M.: An Introduction to Environmental Biophysics, Springer Sci. & Business Media, New York,

859   ISBN: 978-1-4612-1626-1, 1998.

860

861   Cao, J., Chang, M., Pan, Y., Song, T., Liu, Z., Zhao, H., Zhou, M., Zhang, L., and Wang, X.: Assessment and intercomparison of

862   ozone dry deposition schemes over two ecosystems based on Noah-MP in China, Atmos. Environ., https://doi.org/10.1016/

863   j.atmosenv.2022.119353, 2022.

864

865   Cape, J. N., Hamilton, R., and Heal, M. R.: Reactive uptake of ozone at simulated leaf surfaces: Implications for "non-stomatal"
866   ozone flux, Atmos. Environ., 43(5), 1116–1123, https://doi.org/10.1016/j.atmosenv.2008.11.007, 2009.
867
868   Cionco, R. M., Analysis of canopy index values for various canopy densities, Boundary-Layer Meteorol., 15, 81–93,
869   https://doi.org/10.1007/BF00165507, 1978.
870
871   Charusombat, U., Niyogi, D., Kumar, A., and Wang, X.: Evaluating a new deposition velocity module in the Noah land-surface
872   model, Boundary-Layer Meteorol., 137(2), 271–290. https://doi.org/10.1007/s10546-010-9531-y, 2010.
873
874   Clapp, R. B., and Hornberger, G. M.: Empirical equations for some soil hydraulic properties, Water Resour.
875   Res., 14(4), 601– 604, https://doi.org/10.1029/WR014i004p00601, 1978.
876
877   Clifton, O. E., Fiore, A. M., Munger, J. W., Malyshev, S., Horowitz, L. W., Shevliakova, E., Paulot, F., Murray, L. T., and
878   Griffin, K. L.: Interannual variability in ozone removal by a temperate deciduous forest, Geophys. Res. Lett., 44, 542–552,
879   https://doi.org/10.1002/2016GL070923, 2017.
880
881   Clifton, O. E., Fiore, A. M., Munger, J. W., and Wehr, R.: Spatiotemporal controls on observed daytime ozone deposition
882   velocity over northeastern U.S. forests during summer, J. Geophys. Res. Atmos., 124, https://doi.org/10.1029/2018JD029073,
883   2019.
884
885   Clifton, O. E., Fiore, A. M., Massman, W. J., Baublitz, C. B., Coyle, M., Emberson, L., Fares, S., Farmer, D. K., Gentine, P.,
886   Gerosa, G., Guenther, A. B., Helmig, D., Lombardozzi, D. L., Munger, J. W., Patton, E. G., Pusede, S. E., Schwede, D. B., Silva,
887   S. J., Sörgel, M., Steiner, A. L., and Tai, A. P. K.: Dry deposition of ozone over land: processes, measurement, and modeling,
888   Rev. Geophys., 58, https://doi.org/10.1029/2019RG000670, 2020a.
889
890   Clifton, O. E., Patton, E. G., Wang, S., Barth, M., Orlando, J., and Schwantes, R. H.: Large Eddy Simulation for Investigating
891   Coupled Forest Canopy and Turbulence Influences on Atmospheric Chemistry, J. Adv. Model. Earth Sys.,
892   14(10), https://doi.org/10.1029/2022MS003078, 2022.
893
894   Clifton, O. E., Paulot, F., Fiore, A. M., Horowitz, L. W., Correa, G., Baublitz, C. B., Fares, S., Goded, I., Goldstein, A. H.,
895   Gruening, C., Hogg, A. J., Loubet, B., Mammarella, I., Munger, J. W., Neil, L., Stella, P., Uddling, J., Vesala T., and Weng, E.:
896   Influence of dynamic ozone dry deposition on ozone pollution, J. Geophys. Res. Atmos., 125, e2020JD032398,
897   https://doi.org/10.1029/2020JD032398, 2020b.
898

899   Coe, H., Gallagher, M. W., Choularton, T. W., and Dore, C.: Canopy scale measurements of stomatal and cuticular O_3 uptake by

900   Sitka spruce, Atmos. Environ., 29(12), 1413–1423, https://doi.org/10.1016/1352-2310(95)00034-V, 1995.

901

902   Collatz, G., Ribas-Carbo, M. and Berry, J.: Coupled Photosynthesis-Stomatal Conductance Model for Leaves of C_4 Plants,

903   Funct. Plant Biol., 19, https://doi.org/10.1071/PP9920519, 1992.

904

905   Collatz, G. J., Ball, J. T., Grivet, C. and Berry, J. A.: Physiological and environmental regulation of stomatal conductance,

906   photosynthesis and transpiration: a model that includes a laminar boundary layer, Agric. For. Meteorol., 54(2–4), 107–136,

907   https://doi.org/10.1016/0168-1923(91)90002-8, 1991.

908

909   Collineau, S., annd Brunet, Y.: Detection of turbulent coherent motions in a forest canopy part II: Time-scales and conditional

910   averages, Boundary-Layer Meteorol., 66, 49–73, https://doi.org/10.1007/bf00705459, 1993.

911

912   Colorado State University, Soil Hydraulic Properties: https://biocycle.atmos.colostate.edu/shiny/soils/, last access: 8 June 2022.

913

914   Conklin, M. H., Sigg, A., Neftel, A., and Bales, R. C.: Atmosphere-snow transfer function for H_2O_2: microphysical

915   considerations, J. Geophys. Res., 98(D1), 18367–18376, https://doi.org/10.1029/93JD01194, 1993.

916

917   Cooter, E. J., and Schwede, D. B.: Sensitivity of the National Oceanic and Atmospheric Administration multilayer model to

918   instrument error and parameterization uncertainty, J. Geophys. Res., 105(D5), 6695–6707.

919   https://doi.org/10.1029/1999JD901080, 2000.

920

921   Coyle, M.: The Gaseous Exchange of Ozone at Terrestrial Surfaces: Non-stomatal Deposition to Grassland, PhD Thesis,

922   University of Edinburgh, Edinburgh, 2006.

923

924   Coyle, M., Nemitz, E., Storeton-West, R., Fowler, D., and Cape, J. N.: Measurements of ozone deposition to a potato canopy,

925   Agric. For. Meteorol., 149(3-4), 655-666, https://doi.org/10.1016/j.agrformet.2008.10.020, 2009.

926

927   Dabberdt, W. F., Lenschow, D. H., Horst, T. W., Zimmerman, P. R., Oncley, S. P., and Delany, A. C.: Atmosphere-surface

928   exchange measurements, Science, 260, 1472–1481, 1993.

929

930   Davidson, E., and Savage, K.: Soil respiration, temperature and moisture at Harvard Forest EMS Tower since 1995, Harvard

931   Forest Data Archive: HF006, https://doi.org/10.6073/pasta/33ba3432103297fe0644de6e0898f91f, 1999.

932

933   Dentener, F., Drevet, J., Lamarque, J. F., Bey, I., Eickhout, B., Fiore, A. M., Hauglustaine, D., Horowitz, L. W., Krol, M.,

934   Kulshrestha, U. C., Lawrence, M., Galy-Lacaux, C., Rast, S., Shindell, D., Stevenson, D., Van Noije, T., Atherton, C., Bell, N.,

935   Bergman, D., Butler, T., Cofala, J., Collins, B., Doherty, R., Ellingsen, K., Galloway, J., Gauss, M., Montanaro, V., Müller, J. F.,

936   Pitari, G., Rodriguez, J., Sanderson, M., Solmon, F., Strahan, S., Schultz, M., Sudo, K., Szopa, S., and Wild, O.: Nitrogen and

937   sulfur deposition on regional and global scales: A multimodel evaluation, Global Biogeochem. Cy., 20(4),

938   https://doi.org/10.1029/2005GB002672, 2006.

939

940   Echer, F. R., and Rosolem, C. A.: Cotton leaf gas exchange responses to irradiance and leaf aging, Biologia Plantarum, 59(2),

941   366–372, https://doi.org/10.1007/s10535-015-0484-3, 2015.

942

943   El-Madany, T. S., Niklasch, K., Klemm, O.: Stomatal and Non-Stomatal Turbulent Deposition Flux of Ozone to a Managed

944   Peatland, Atmosphere, 8, 175; https://doi.org/10.3390/atmos8090175, 2017.

945

946   Ellsworth, D. S., and Reich, P. B.: Canopy structure and vertical patterns of photosynthesis and related leaf traits in a deciduous

947   forest, Oecologia, 96, 169–178, https://doi.org/10.1007/BF00317729, 1993.

948

949   Emberson, L.: Effects of ozone on agriculture, forests and grasslands, Philos. Trans. Royal Soc. A, 378(2183),

950   https://doi.org/10.1098/rsta.2019.0327, 2020.

951

952   Emberson, L. D., Kitwiroon, N., Beevers, S., Büker, P., and Cinderby, S.: Scorched Earth: how will changes in the strength of

953   the vegetation sink to ozone deposition affect human health and ecosystems?, Atmos. Chem. Phys., 13, 6741–6755,

954   https://doi.org/10.5194/acp-13-6741-2013, 2013.

955

956   Erisman, J. W., van Pul, A., and Wyers, P.: Parameterization of dry deposition mechanisms for the quantification of atmospheric

957   input to ecosystems, Atmos. Environ., 28, 2595–2607, https://doi.org/10.1016/1352-2310(94)90433-2, 1994.

958

959   Fares, S., Savi, F., Muller, J., Matteucci, G., and Paoletti, E.: Simultaneous measurements of above and below canopy ozone

960   fluxes help partitioning ozone deposition between its various sinks in a Mediterranean Oak Forest, Agric. For. Meterol., 198-199,

961   181–191, https://doi.org/10.1016/j.agrformet.2014.08.014, 2014.

962

963   Fares, S., Conte, A., and Chabbi, A.: Ozone flux in plant ecosystems: new opportunities for long-term monitoring networks to

964   deliver ozone-risk assessments, Environ. Sci. Pollut. Res., https://doi.org/10.1007/s11356-017-0352-0, 2017.

965

966   Farmer, D. K., Boedicker, E. K., and DeBolt, H. M.: Dry Deposition of Atmospheric Aerosols: Approaches, Observations, and

967   Mechanisms, Ann. Rev. Phys. Chem., 72, 16.1–16.23, https://doi.org/10.1146/annurev-physchem-090519- 034936, 2021.

968

969   Farquhar, G. D., von Caemmerer, S. and Berry, J. A.: A biochemical model of photosynthetic CO_2 assimilation in leaves of C_3

970   species, Planta, 149(1), 78–90, https://doi.org/10.1007/BF00386231, 1980.

971

972   Ferréa, C., Zenone, T., Comolli, R., and Seufert, G.: Estimating heterotrophic and autotrophic soil respiration in a semi-natural

973   forest of Lombardy, Italy, Pedobiologia, 55(6), 285–294, http://dx.doi.org/10.1016/j.pedobi.2012.05.001, 2012.

974

975   Finco, A., Coyle, M., Nemitz, E., Marzouli, R., Chiesa, M., Loubet, B., Fares, S., Diaz-Pines, E., Gasche, R., and Gerosa, G.:

976   Characterization of ozone deposition to a mixed oak-hornbeam forest – flux measurements at five levels above and inside the

977   canopy and their interactions with nitric oxide, Atmos. Chem. Phys., 18, 17945–17961, https://doi.org/10.5194/acp-18-17945-

978   2018, 2018.

979

980   Fitzjarrald, D., and Sakai, R.: Measurements at Harvard Forest EMS Tower 1991-2007, Harvard Forest Data Archive: HF102

981   (v.22), Environmental Data Initiative, https://doi.org/10.6073/pasta/673330eb6a4e045fbc89d8e862b2c920, 2009.

982

983   Flechard, C. R., Nemitz, E., Smith, R. I., Fowler, D., Vermeulen, A. T., Bleeker, A., Erisman, J. W., Simpson, D., Zhang, L.,

984   Tang, Y. S., and Sutton, M. A.: Dry deposition of reactive nitrogen to European ecosystems: A comparison of inferential models

985   across the NitroEurope network, Atmos. Chem. Phys., 11, 2703–2728, https://doi.org/10.5194/acp-11-2703-2011, 2011.

986

987   Foken, T., Göockede, M., Mauder, M., Mahrt, L., Amiro, B., and Munger, W.: Post-field data quality control, in: Handbook of

988   Micrometeorology, Springer, Dordrecht, 181–208, https://doi.org/10.1007/1-4020-2265-4_9, 2004.

989

990   Fowler, D., Flechard, C., Cape, J.N. Storeton-West, R. L. and Coyle, M.: Measurements of Ozone Deposition to Vegetation

991   Quantifying the Flux, the Stomatal and Non-Stomatal Components, Water Air Soil Pollut., 130, 63–74,

992   https://doi.org/10.1023/A:1012243317471, 2001.

993

994   Fowler, D., Pilegaard, K., Sutton, M. A., Ambus, P., Raivonen, M., Duyzer, J., Simpson, D., Fagerli, H., Fuzzi, S., Schjoerring,

995   J. K., Granier, C., Neftel, A., Isaksen, I. S. A., Laj, P., Maione, M., Monks, P. S., Burkhardt, J., Daemmgen, U., Neirynck, J.,

996   Personne, Wichink Kruit, R. J., Butterbach-Bahl, K., Flechard, C., Tuovinen, J. P., Coyle, M., Gerosa, G. Loubet, B., Altimir, N.,

997   Gruenhage, L., Ammann, C., Cieslik, S., Paoletti, E., Mikkelsen, T. N., Ro-Poulsen, H., Cellier, P., Cape, J. N., Horvath, L.,

998   Loreto, F., Niinemets, U., Palmer, P. I., Rinne, J., Misztal, P., Nemitz, E., Nilsson, D., Pryor, S., Gallagher, M. W., Vesala, T.,

999   Skiba, U., Brueggemann, N., Zechmeister-Boltenstern, S., Williams, J., O'Dowd, C., Facchini, M. C., de Leeuw, G., Flossman,

000   A., Chaumerliac, N., and Erisman, J. W.: Atmospheric composition change: Ecosystems- atmosphere interactions, Atmos.

001   Environ., 43(33), 5193–5267, https://doi.org/10.1016/j.atmosenv.2009.07.068, 2009.

002

003   Froelich, N., Croft, H., Chen, J. M., Gonsamo, A., and Staebler, R. M.: Trends of carbon fluxes and climate over a mixed

004   temperate–boreal transition forest in southern Ontario, Canada, Agric. For. Meterol., 211-212, 72–84,

005   https://doi.org/10.1016/j.agrformet.2015.05.009, 2015.

006

007   Fuentes, J. D., and Gillespie, T. J.: A gas exchange system to study the effects of leaf surface wetness on the deposition of ozone,

008   Atmos. Environ., 26A(6), 1165–1173, https://doi.org/10.1016/0960-1686(92)90048-P, 1992.

009

010   Fuentes, J. D., Gillespie, T. J., den Hartog, G., and Neumann, H. H.: Ozone deposition onto a deciduous forest during dry and

011   wet conditions, Agric. For. Meteorol., 62, 1–18, https://doi.org/10.1016/0168-1923(92)90002-L, 1992.

012

013   Fuller, E. N, Schettler, P. D., and Giddings, J. C.: A new method for prediction of binary gas phase diffusion coefficients, Ind.

014   Eng. Chem., 53, 19–27, https://doi.org/10.1021/ie50677a007, 1966.

015

016   Fumagalli, I., Gruening, C., Marzuoli, R., Cieslik, S.: Long-term measurements of NO_x and O_3 soil fluxes in a temperate

017   deciduous forest, Agric. For. Meteorol., 228-229, 205–216, https://doi.org/10.1016/j.agrformet.2016.07.011, 2016.

018

019   Galmarini, S., Bianconi, R., Klug, W., Mikkelsen, T., Addis, R., Andronopoulos, S., et al.: Ensemble dispersion forecasting—

020   Part I: concept, approach and indicators, Atmos. Environ., 38(28), 4607–4617, https://doi.org/10.1016/j.atmosenv.2004.05.030,

021   2004.

022

023   Galmarini, S., Makar, P., Clifton, O., Hogrefe, C., Bash, J., Bianconi, R., Bellasio, R., Bieser, J., Butler, T., Ducker, J.,

024   Flemming, J., Hozdic, A., Holmes, C., Kioutsioukis, I., Kranenburg, R., Lupascu, A., Perez-Camanyo, J. L., Pleim, J., Ryu, Y.-

025   H., San Jose, R., Schwede, D., Silva, S., Garcia Vivanco, M., and Wolke, R.: Technical Note – AQMEII4 Activity 1: Evaluation

026   of Wet and Dry Deposition Schemes as an Integral Part of Regional-Scale Air Quality Models, Atmos. Chem. Phys., 21, 15663–

027   15697, https://doi.org/10.5194/acp-21-15663-2021, 2021.

028

029   Ganzeveld, L. and Lelieveld, J.: Dry deposition parameterization in a chemistry general circulation model and its influence on

030   the distribution of reactive trace gases, J. Geophys. Res., 100, https://doi.org/10.1029/95jd02266, 1995.

031

032   Ganzeveld, L., Lelieveld, J., and Roelofs, G. J.: A dry deposition parameterization for sulfur oxides in a chemistry and general

033   circulation model, J. Geophys. Res. Atmos., 103, 5679–5694, https://doi.org/10.1029/97JD03077, 1998.

034

035   Ganzeveld, L., Bouwman, L., Stehfest, E., van Vuuren, D., Eickhout, B., and Lelieveld, J.: Impacts of future land cover changes

036   on atmospheric chemistry-climate interactions, J. Geophys. Res., 115, https://doi.org/10.1029/2010JD014041, 2010.

037

038   Gao, W., Shaw, R. H., and Paw, U. K. T.: Observation of organized structure in turbulent flow within and above a forest canopy,

039   Boundary-Layer Meteorol., 47, 349–377, https://doi.org/10.1007/BF00122339, 1989.

040

041   Garratt, J. R.: The Atmospheric Boundary Layer, Cambridge University Press, Cambridge, Great Britain, 316 pp, 1992.

042

043   Gerosa, G. A., Marzuoli, R., and Finco, A.: Interannual variability of ozone fluxes in a broadleaf deciduous forest in Italy, Elem.

044   Sci. Anth., 10(1), https://doi.org/10.1525/elementa.2021.00105, 2022.

045

046   Global Modeling and Assimilation Office (GMAO): MERRA-2 tavg1_2d_flx_Nx: 2d,1-Hourly,Time-Averaged,Single-

047   Level,Assimilation,Surface Flux Diagnostics V5.12.4 (M2T1NXFLX), Greenbelt, MD, USA: Goddard Space Flight Center

048   Distributed Active Archive Center (GSFC DAAC), Last access: 1 July 2020, https://doi.org/10.5067/7MCPBJ41Y0K6, 2015.

049

050   Godowitch, J. M.: Vertical ozone fluxes and related deposition parameters over agricultural and forested landscapes, Boundary-

051   Layer Meteorol., 50, 375–404, https://doi.org/10.1007/BF00120531, 1990.

052

053   Goldstein, A. H., McKay, M., Kurpius, M. R., Schade, G. W., Lee, A., Holzinger, R., and Rasmussen, R. A.: Forest thinning

054   experiment confirms ozone deposition to forest canopy is dominated by reaction with biogenic VOCs, Geophys. Res. Lett.,

055   31(L22106), https://doi.org/ 10.1029/2004GL021259, 2004.

056

057   Gong, C., Liao, H., Yue, X., Ma, Y., and Lei, Y.: Impacts of Ozone-Vegetation Interactions on Ozone Pollution Episodes in

058   North China and the Yangtze River Delta, Geophys. Res. Lett., 48(12), e2021GL093814, 2021.

059

060   Guarin, J. R., Emberson, L., Simpson, D., Hernandez-Ochoa, I. M., Rowland, D., and Asseng, S.: Impacts of tropospheric ozone

061   and climate change on Mexico wheat production, Climatic Change, 155(2), 157–174, https://doi.org/10.1007/s10584-019-02451-

062   4, 2019.

063

064   Guenther, A., Kulmala, M., Turnipseed, A., Rinne, J., Suni, T., and Reissell, A.: Integrated land ecosystem-atmosphere processes

065   study (iLEAPS) assessment of global observational networks, Boreal Environ. Res., 16, 321–336, 2011.

066

067   Güsten, H., Heinrich, G., Schmidt, R. W. H., and Schurath, U.: A novel ozone sensor for direct eddy flux measurements, J.

068   Atmos. Chem., 14, 73–84, https://doi.org/10.1007/BF00115224, 1992.

069

070   Güsten, H., and Heinrich, G.: On-line measurements of ozone surface fluxes. 1. Methodology and instrumentation, Atmos.

071   Environ., 30(6), 897–909, https://doi.org/10.1016/1352-2310(95)00269-3, 1996.

072

073   Grulke, N. E., and Heath, R. L.: Ozone effects on plants in natural ecosystems, Plant Biology, 22(S1), 12–37,

074   https://doi.org/10.1111/plb.12971, 2019.

075

076   Grünzweig, J. M., Navon, Y., Kanas, D., Dirks, I., and Dumbur, R.: Study of major processes in the biogeochemical cycles of the

077   Phillyrea latifolia shrubland in Ramat Hanadiv, Final Research Report, The Hebrew University of Jerusalem and Ramat

078   Hanadiv, Israel, 2010.

079

080   Hardacre, C., Wild, O., and Emberson, L.: An evaluation of ozone dry deposition in global scale chemistry climate models,

081   Atmos. Chem. Phys., 15, 6419–6436, https://doi.org/10.5194/acp-15-6419-2015, 2015.

082

083   He, C., Clifton, O., Felker-Quinn, E., Fulgham, S. R., Juncosa Calahorrano, J. F., Lombardozzi, D., Purser, G., Riches, M.,

084   Schwantes, R., Tang, W., Poulter, B., and Steiner, A. L.: Interactions between Air Pollution and Terrestrial Ecosystems:

085   Perspectives on Challenges and Future Directions, Bull. Am. Meteorol. Soc., https://doi.org/10.1175/BAMS-D-20-0066.1, 2021.

086

087   Helmig, D., Cohen, L. D., Bocquet, F., Oltmans, S., Grachev, A., and Neff, W.: Spring and summertime diurnal surface ozone

088   fluxes over the polar snow at Summit, Greenland, Geophys. Res. Lett., 36, L08809, https://doi.org/10.1029/2008gl036549, 2009.

089

090   Helmig, D., Ganzeveld, L., Butler, T., and Oltmans, S. J.: The role of ozone atmosphere-snow gas exchange on polar, boundary-

091   layer tropospheric ozone – a review and sensitivity analysis, Atmos. Chem. Phys., 7, 15–30, 2007.

092

093   Hicks, B. B., Kolb, C. E., and Lenschow, D. H.: New opportunities for flux measurement, in: Global tropospheric chemistry:

094   Chemical fluxes in the global atmosphere, edited by Lenschow, D. H., and Hicks, B. B., National Center for Atmospheric

095   Research, Boulder, CO, 83–85, 1989.

096

097   Hicks, B. B, Baldocchi, D. D., Meyers, T. E, Hosker, R. E Jr., and Matt, D. R.: A preliminary multiple resistance routine for

098   deriving dry deposition velocities from measured quantities, Water, Air, and Soil Pollut., 36, 311,1987.

099

100   Hogrefe, C., Liu, P., Pouliot, G., Mathur, R., Roselle, S., Flemming, J., Lin, M., and Park, R. J.: Impacts of different

101   characterizations of large-scale background on simulated regional-scale ozone over the continental United States, Atmos. Chem.

102   Phys., 18(5), 3839–3864, https://doi.org/10.5194/acp-18-3839-2018, 2018.

103

104   Hong, C., Mueller, N. D., Burney, J. A., Zhang, Y., AghaKouchak, A., Moore, F. C., Qin, Y., Tong, D., and Davis, S. J.: Impacts

105   of ozone and climate change on yields of perennial crops in California, Nature Food, 1, 166–172, https://doi.org/10.1038/s43016-

106   020-0043-8, 2020.

107

108   Horváth, L., Koncz, P., Móring, A., Nagy, Z., Pintér, K., and Weidinger, T.: An attempt to partition stomatal and non-stomatal
109   ozone deposition parts on a short grassland, Boundary-Layer Meteorol., 167(2), 303–326, https://doi.org/10.1007/s10546-017-
110   0310-x, 2018.
111
112   Högström, U.: Non-dimensional wind and temperature profiles in the atmospheric surface layer: A re-evaluation, Boundary
113   Layer Meteorol., 42, 55–78, https://doi.org/10.1007/BF00119875, 1988.
114
115   Huang, L., McDonald-Buller, E. C., McGaughey, G., Kimura, Y., and Allen, D. T.: The impact of drought on ozone dry
116   deposition over eastern Texas, Atmos. Environ., 127, 176–186, https://doi.org/10.1016/j.atmosenv.2015.12.022, 2016.
117
118   Huang, M., Crawford, J. H., Carmichael, G. R., Bowman, K. W., Kumar, S. V., and Sweeney, C.: Satellite soil moisture data
119   assimilation impacts on modeling weather variables and ozone in the southeastern US – Part 2: Sensitivity to dry-deposition
120   parameterizations, Atmos. Chem. Phys., 22, 7461–7487, https://doi.org/10.5194/acp-22-7461-2022, 2022.
121
122   Hubert, M., and Vandervieren, E.: An Adjusted Boxplot for Skewed Distributions, Comput. Stat. Data Anal., 52(12), 5186–5201,
123   https://doi.org/10.1016/j.csda.2007.11.008, 2008.
124
125   Huthwelker, T., Ammann, M., and Peter, T.: The Uptake of Acidic Gases on Ice, Chem. Rev., 106, 1375–1444,
126   https://doi.org/10.1021/cr020506v, 2006.
127
128   Ilvesniemi, H., Levula, J., Ojansuu, R., Kolari, P., Kulmala, L., Pumpanen, J., Launiainen, S., Vesala, T., and Nikinmaa, E.:
129   Long-term measurements of the carbon balance of a boreal Scots pine dominated forest ecosystem, Boreal Env. Res., 14, 731–
130   753, 2009.
131
132   Iqbal, M., An Introduction to Solar Radiation, Academic Press, 386 pp., ISBN: 9780323151818, 1983.
133
134   Jarvis, P. G.: The interpretation of the variations in leaf water potential and stomatal conductance found in canopies in the field,
135   Philos. Trans. R. Soc. Lond. B Biol. Sci., 273, 593–610, https://doi.org/10.1098/rstb.1976.0035, 1976.
136
137   Jensen, N. O., and Hummelshøj, P.: Derivation of canopy resistance for water vapour fluxes over a spruce forest, using a new
138   technique for the viscous sublayer resistance, Agric. For. Meteorol., 73, 339–352, https://doi.org/10.1016/0168-1923(94)05083-I,
139   1995.
140

141 Jensen, N. O., and Hummelshøj, P.: Derivation of canopy resistance for water vapor fluxes over a spruce forest, using a new

142 technique for the viscous sublayer resistance (correction to vol. 73, pp. 339, 1995), Agric. For. Meteorol, 85(3-4), 289,

143 https://doi.org/10.1016/S0168-1923(97)00024-5, 1997.

144

145 Jones, S. K., Helfter, C., Anderson, M., Coyle, M., Campbell, C., Famulari, D., Di Marco, C., van Dijk, N., Tang, Y. S., Topp, C.

146 F. E., Kiese, R., Kindler, R., Siemens, J., Schrumpf, M., Kaiser, K., Nemitz, E., Levy, P. E., Rees, R. M., Sutton, M. A., and

147 Skiba, U. M.: The nitrogen, carbon and greenhouse gas budget of a grazed, cut and fertilised temperate grassland,

148 Biogeosciences, 14(8), 2069–2088, https://doi.org/10.5194/bg-14-2069-2017, 2017.

149

150 Kanamitsu, M., Ebisuzaki, W., Woollen, J., Yang, S.-K., Hnilo, J. J., Fiorino, M., and Potter, G. L.: NCEP-DOE AMIP-II

151 Reanalysis (R-2), Bull. Am. Meteorol. Soc., 83, 1631–1643, https://doi.org/10.1175/BAMS-83-11-1631, 2002.

152

153 Kaplan, M.: The soils of Ramat Hanadiv, Society for the Protection of Nature in Israel, Tel-Aviv, 1989.

154

155 Karl, T., Harley, T., Emmons, L., Thornton, B., Guenther, A., Basu, C., Turnipseed, A., and Jardine, K.: Efficient Atmospheric

156 Cleansing of Oxidized Organic Trace Gases by Vegetation, Science, 330, 816–819, https://doi.org/10.1126/science.1192534,

157 2010.

158

159 Kattge, J., Knorr, W., Raddatz, T., and Wirth, C.: Quantifying photosynthetic capacity and its relationship to leaf nitrogen

160 content for global-scale terrestrial biosphere models, Glob. Chan. Biol. 15, 976–991, https://doi.org/10.1111/j.1365-

161 2486.2008.01744.x, 2009.

162

163 Kavassalis, S. C., and Murphy, J. G.: Understanding ozone-meteorology correlations: A role for dry deposition, Geophys. Res.

164 Lett., 44(6), 2922–2931, https://doi.org/10.1002/2016GL071791, 2017.

165

166 Keronen, P., Reissell, A., Rannik, Ü., Pohja, T., Siivola, E., Hiltunen, V., Hari, P., Kulmala, M., and Vesala, T.: Ozone flux

167 measurements over a Scots pine forest using eddy covariance method: performance evaluation and comparison with flux-profile

168 method, Boreal Env. Res., 8, 425–443, 2003.

169

170 Knauer, J., El-Madany, T.S., Zaehle, S., and Migliavacca, M.: Bigleaf-An R package for the calculation of physical and

171 physiological ecosystem properties from eddy covariance data, PLoS ONE, 13(8), e0201114,

172 https://doi.org/10.1371/journal.pone.0201114, 2018.

173

174 Kolari, P., Pumpanen, J., Kulmala, L., Ilvesniemi, H., Nikinmaa, E., Grönholm, T., and Hari, P.: Forest floor vegetation plays an
175 important role in photosynthetic production of boreal forests, For. Ecol. Manag., 221, 241–248,
176 https://doi.org/10.1016/j.foreco.2005.10.021, 2006.
177
178 Koncz, P., Besnyői, V., Csathó, A. I., Nagy, J., Szerdahelyi, T., Tóth, Z. S., Pintér, K., Balogh, J, Nagy, Z, and Bartha, S.: Effect
179 of grazing and mowing on the microcoenological composition of semi-arid grassland in Hungary, Appl. Ecol. Environ. Res.,
180 12(2), 563–575, 2014.
181
182 Krupa, S. V.: Effects of atmospheric ammonia (NH_3) on terrestrial vegetation: A review, Environ. Pollut., 124(2), 179–221,
183 https://doi.org/10.1016/s0269-7491(02)00434-7, 2003.
184
185 Kurpius, M. R., and Goldstein, A. H.: Gas-phase chemistry dominates O_3 loss to a forest, implying a source of aerosols and
186 hydroxyl radicals to the atmosphere, Geophys. Res. Lett., 30(7), https://doi.org/10.1029/2002GL016785, 2003.
187
188 Launiainen, S., Katul, G. G., Grönholm, T., and Vesala, T.: Partitioning ozone fluxes between canopy and forest floor by
189 measurements and a multi-layer model, Agric. For. Meteorol., 173, 85–99, https://doi.org/10.1016/j.agrformet.2012.12.009,
190 2013.
191
192 Leith, F. I., Garnett, M. H., Dinsmore, K. J., Billett, M. F., and Heal, K. V.: Source and age of dissolved and gaseous carbon in a
193 peatland-riparian-stream continuum: A dual isotope (14C and 14C) analysis, Biogeochemistry, 119, 415–433,
194 https://doi.org/10.1007/s10533-014-9977-y, 2014.
195
196 Le Morvan-Quéméner, A., Coll, I., Kammer, J., Lamaud, E., Loubet, B., Personne, E., and Stella, P.: Impact of parameterization
197 choices on the restitution of ozone deposition over vegetation, Atmos. Environ., 178, 49–65,
198 https://doi.org/10.1016/j.atmosenv.2018.01.003, 2018.
199
200 Lenschow, D. H., Pearson, R. Jr., and Stankov, B. B.: Estimating the ozone budget in the boundary layer by use of aircraft
201 measurements of ozone eddy flux and mean concentration, J. Geophys. Res., 86(C8), 7291–7297, https://doi.org/10.1029/
202 JC086iC08p07291, 1981.
203 Leuning, R.: Modelling stomatal behaviour and photosynthesis of Eucalyptus grandis, Aust. J. Plant Physiol., 17, 159–175,
204 http://hdl.handle.net/102.100.100/257808?index=1, 1990
205 Leuning R.: A critical appraisal of a combined stomatal-photosynthesis model for C3 plants, Plant, Cell Environ., 18, 339–355,
206 https://doi.org/10.1111/j.1365-3040.1995.tb00370.x, 1995.

207

208 Leuning, R., Dunin, F.X., Wang, Y.-P.: A two-leaf models for canopy conductance, photosynthesis and partitioning of avail-
209 able energy II. Comparison with measurements. Agric. For. Meteorol. 91(1-3), 113–125, https://doi.org/10.1016/S0168-
210 1923(98)00074-4, 1998.

211

212 Li, S. M., Anlauf, K. G., and Wiebe, H. A.: Heterogeneous nighttime production and deposition of particle nitrate at a rural site
213 in North America during summer 1988, J. Geophys. Res., 98, 5139–5157, https://doi.org/10.1029/92JD02523, 1993.

214

215 Li, Q., Gabay, M., Rubin, Y., Fredj, E., and Tas, E.: Measurement-based investigation of ozone deposition to vegetation under
216 the effects of coastal and photochemical air pollution in the Eastern Mediterranean, Sci. Tot. Environ., 645, 1579–1597,
217 https://doi.org/10.1016/j.scitotenv.2018.07.037, 2018.

218

219 Li, Q., Gabay, M., Rubin, Y., Raveh-Rubin, S., Rohatyn, S., Tatarinov, F., Rotenberg, E., Ramati, E., Dicken, U., Preisler, Y.,
220 Fredj, Yakir, D., and Tas, E.: Investigation of ozone deposition to vegetation under warm and dry conditions near the Eastern
221 Mediterranean coast, Sci. Tot. Environ., 658, 1316–1333, https://doi.org/10.1016/j.scitotenv.2018.12.272, 2019.

222

223 Li, Y., Schichtel, B. A., Walker, J. T., Schwede, D. B., Chen, X., Lehmann, C. M. B., Puchalski, M. A., Gay, D. A., and Collett,
224 J. L.: Increasing importance of deposition of reduced nitrogen in the United States, Proc. Natl. Acad. Sci. U.S.A., 113, 5874–
225 5879, https://doi.org/10.1073/pnas.1525736113, 2016.

226

227 Lin, M., Horowitz, L. W., Xie, Y., Paulot, F., Malyshev, S., Shevliakova, E., Finco, A., Gerosa, G., Kubistin, D., and Pilegaard,
228 K.: Vegetation feedbacks during drought exacerbate ozone air pollution extremes in Europe, Nat. Clim., 10, 444–451,
229 https://doi.org/10.1038/s41558-020-0743-y, 2020.

230

231 Liu, Z., Doherty, R. M., Wild, O., O'Connor, F. M., and Turnock, S. T.: Correcting ozone biases in a global chemistry–climate
232 model: implications for future ozone, Atmos. Chem. Phys., 22, 12543–12557, https://doi.org/10.5194/acp-22-12543-2022, 2022.

233

234 Lombardozzi, D., Levis, S., Bonan, G., Hess, P. G., and Sparks, J. P.: The influence of chronic ozone exposure on global carbon
235 and water cycles, J. Clim., 28, 292–305, https://doi.org/10.1175/Jcli-D-14-00223.1, 2015.

236

237 Lombardozzi, D., Sparks, J. P., and Bonan, G.: Integrating O_3 influences on terrestrial processes: Photosynthetic and stomatal
238 response data available for regional and global modeling, Biogeosciences, 10(11), 6815–6831, https://doi.org/10.5194/bg-10-
239 6815-2013, 2013.

240

241 Machon, A., Horváth, L., Weidinger, T., Grosz, B., Móring, A., and Führer, E.: Measurement and modeling of N-balance

242 between atmosphere and biosphere over a grazed grassland (Bugacpuszta) in Hungary, Water Air Soil Pollut., 226(27),

243 https://doi.org/10.1007/s11270-014-2271-8, 2015.

244

245 Mahrt, L., Lenschow, D. H., Sun, J., Weil, J. C., MacPherson, J. I., and Desjardins, R. L.: Ozone fluxes over a patchy cultivated

246 surface, J. Geophys. Res., 100(D11), 23125–23131, https://doi.org/10.1029/95JD02599, 1995.

247

248 Makar, P. A., Akingunola, A., Aherne, J., Cole, A. S., Aklilu, Y., Zhang, J., Wong, I., Hayden, K., Li, S.-M., Kirk, J., Scott, K.,

249 Moran, M. D., Robichaud, A., Cathcart, H., Baratzedah, P., Pabla, B., Cheung, C., Zheng, Q., and Jeffries, D. S.: Estimates of

250 exceedances of critical loads for acidifying deposition in Alberta and Saskatchewan, Atm. Chem. Phys., 18, 9897–9927,

251 https://doi.org/10.5194/acp-18-9897-2018, 2018.

252

253 Manes, F., Incerti, G., Salvatori, E., Vitale, M., Ricotta, C., and Costanza, R.: Urban ecosystem services: tree diversity and

254 stability of tropospheric ozone removal, Ecol. Appl., 22(1), 349–360, https://doi.org/10.1890/11-0561.1, 2012.

255

256 Massad, R-S., Nemitz, E., and Sutton, M.A.: Review and parameterization of bi-directional ammonia exchange between

257 vegetation and the atmosphere, Atmos. Chem. Phys., 10, 10359–10386, https://doi.org/10.5194/acp-10-10359-2010, 2010.

258

259 Massman, W. J.: A review of the molecular diffusivities of H_2O, CO_2, CH_4, CO, O_3, SO_2, NH_3, N_2O, NO, and NO_2 in air, O_2 and

260 N_2 near STP, Atmos. Environ., 32(6), 1111–1127, 1998.

261

262 Massman, W. J.: Toward an ozone standard to protect vegetation based on effective dose: a review of deposition resistances and

263 a possible metric, Atmos. Environ., 38(15), 2323–2337, https://doi.org/10.1016/j.atmosenv.2003.09.079, 2004.

264 Matichuk, R., Tonnesen, G., Luecken, D., Gilliam, R., Napelenok, S. L., Baker, K. R., Schwede, D., Murphy, B., Helmig, D.,

265 Lyman, S. N., and Roselle, S.: Evaluation of the community multiscale air quality model for simulating winter ozone formation

266 in the Uinta Basin, J. Geophys. Res. Atmos, 122, 13,545–13,572, https://doi.org/10.1002/2017JD027057, 2017.

267 Mauder, M., Foken, T., Clement, R., Elbers, J. A., Eugster, W., Grünwald, T., Heusinkveld, B., and Kolle, O.: Quality control of

268 CarboEurope flux data – Part 2: Inter-comparison of eddy-covariance software, Biogeosciences, 5, 451–462,

269 https://doi.org/10.5194/bg-5-451-2008, 2008.

270

271 Mauzerall, D. L., and Wang, X: Protecting agricultural crops from the effects of tropospheric ozone exposure: reconciling

272 science and standard setting in the United States, Europe, and Asia, Ann. Rev. Energy Environ., 26, 237–268,

273 https://doi.org/10.1146/annurev.energy.26.1.237, 2001.

274

275   McGrath, J. M., Betzelberger A. M., Wang, S., Shook, E., Zhu, X. G., Long, S. P., and Ainsworth, E. A.: An analysis of ozone

276   damage to historical maize and soybean yields in the United States, Proc. Natl. Acad. Sci. U.S.A., 112, 14390–14395,

277   https://doi.org/10.1073/pnas.1509777112, 2015.

278

279   McRae, G. J.: Mathematical Modeling of Photochemical Air Pollution, Ph.D. Thesis, California Institute of Technology,

280   Pasadena, California, https://doi.org/10.7907/n8p7-fl49, 1981.

281

282   Medlyn, B. E., Duursma, R. A., Eamus, D., Ellsworth, D. S., Prentice, I. C., Barton, C. V. M., Crous, K. Y., de Angelis, P.,

283   Freeman, M., and Wingate, L.: Reconciling the optimal and empirical approaches to modelling stomatal conductance, Global

284   Change Biol., 17, 2134–2144, https://doi.org/10.1111/j.1365-2486.2010.02375.x, 2011.

285

286   Meyers, T. P., The sensitivity of modeled SO_2 fluxes and profiles to stomatal and boundary layer resistances, Water Air Soil

287   Pollut., 35, 261–278, https://doi.org/10.1007/BF00290935, 1987.

288

289   Meyers, T. P., Finkelstein, P., Clarke, J., Ellestad, T. G., and Sims, P. F.: A multilayer model for inferring dry deposition using

290   standard meteorological measurements, J. Geophys. Res., 5(103), 22645–22661, 1998.

291

292   Mészáros, R., Horváth, L., Weidinger, T., Neftel, A., Nemitz, E., Dämmgen, U., Cellier, P., and Loubet, B.: Measurement and

293   modelling ozone fluxes over a cut and fertilized grassland, Biogeosciences, 6(10), 1987–1999, https://doi.org/10.5194/bg-6-

294   1987-2009, 2009.

295

296   Michou, M., Laville, P., Serc¸, D., Fotiadi, A., Bouchouc, P., amd Peuch, V.-H.: Measured and modeled dry deposition velocities

297   over the ESCOMPTE area, Atmos. Res., 74, 89–116, https://doi.org/10.1016/j.atmosres.2004.04.011, 2004.

298

299   Milford, C.: Dynamics of atmospheric ammonia exchange with intensively-managed grassland, PhD Thesis, University of

300   Edinburgh, Edinburgh, 2004.

301

302   Muller, J. B., Coyle, M., Fowler, D., Gallagher, M. W., Nemitz, E. G., and Percival, C. J.: Comparison of ozone fluxes over

303   grassland by gradient and eddy covariance technique, Atmos. Sci. Lett., 10(3), 164–169, https://doi.org/10.1002/asl.226, 2009.

304

305   Muller, J. B., Percival, C. J., Gallagher, M. W., Fowler, D., Coyle, M., and Nemitz, E.: Sources of uncertainty in eddy covariance

306   ozone flux measurements made by dry chemiluminescence fast response analyzers, Atmos. Meas. Tech., 3, 163–176,

307   https://doi.org/10.5194/amt-3-163-2010, 2010.

308

309   Munger, J. W., Wofsy, S. C., Bakwin, P. S., Fan, S.-M., Goulden, M. L., Daube, B. C., Goldstein, A. H., Moore, K. E., and

310   Fitzjarrald, D. R.: Atmospheric deposition of reactive nitrogen oxides and ozone in a temperate deciduous forest and a subarctic

311   woodland 1. Measurements and mechanisms, J. Geophys. Res., 101(D7), 12639–12657, https://doi.org/10.1029/96JD00230,

312   1996.

313

314   Munger, J. W., and Wofsy, S.: Canopy-atmosphere exchange of carbon, water and energy at Harvard Forest EMS Tower since

315   1991, Harvard Forest Data Archive: HF004, https://doi.org/10.6073/pasta/dd9351a3ab5316c844848c3505a8149d, 1999.

316

317   Munger, W., and Wofsy, S.: Biomass Inventories at Harvard Forest EMS Tower since 1993 version 34, Environmental Data

318   Initiative. https://doi.org/10.6073/pasta/92143fc1a5a68864dc2ef99152aa4300, 2021.

319

320   Nemitz, E., Milford, C., and Sutton, M. A.: A two-layer canopy compensation point model for describing bi-directional

321   biosphere-atmosphere exchange of ammonia, Q. J. Roy. Meteor. Soc., 127, 815–833, https://doi.org/10.1002/qj.49712757306,

322   2001.

323

324   Nguyen, T. B., Crounse, J. D., Teng, A. P., Clair, J. M. S., Paulot, F., Wolfe, G. M., and Wennberg, P. O.: Rapid deposition of

325   oxidized biogenic compounds to a temperate forest, Proc. Natl. Acad. Sci. U.S.A., 112(5), E392–E401,

326   https://doi.org/10.1073/pnas.141870211, 2015.

327

328   NOAA Global Monitoring Laboratory: Trends in Atmospheric Carbon Dioxide: https://gml.noaa.gov/ccgg/trends/, last access:

329   31 August 2022

330

331   Norman, J. M.: Biometeorology in Integrated Pest Management, New York: Elsevier, ISBN: 9780323147965, 1982.

332

333   Norman, J. M.: Modeling the complete crop canopy, in: Modification of the Aerial Environment of Crops, edited by: Barfield, B.

334   J., and Gerber, J. F., Am. Soc. of Agric. Eng., St. Joseph, Michigan, 249–280, ISBN: 09-161-50151, 1979.

335

336   Oleson, K. W., Lawrence, D. M., Bonan, G. B., Drewniak, B., Huang, M., Koven, C. D., Levis, S., Li, F., Riley, W. J., Subin, Z.

337   M., Swenson, S. C., Thornton, P. E., Bozbiyik, A., Fisher, R., Heald, C. L., Kluzek, E., Lamarque, J.-F., Lawrence, P. J., Leung,

338   L. R., Lipscomb, W., Muszala, S., Ricciuto, D. M., Sacks, W., Sun, Y., Tang, J., and Yang, Z.-L.: Technical description of

339   version 4.5 of the Community Land Model (CLM), NCAR Earth System Laboratory – Climate and Global Dynamics Division,

340   Boulder, Colorado, USA, Tech. Rep. TN-503+STR, http://www.cesm.ucar.edu/models/cesm1.2/clm/ CLM45_Tech_Note.pdf

341   (last access: 03 January 2022), 2013.

342

343   Oliver, R. J., Mercado, L. M., Sitch, S., Simpson, D. M., Medlyn, B. E., Lin, Y., and Folberth, G. A.: Large but decreasing effect

344   of ozone on the European carbon sink, Biogeosciences, 4245–4269, https://doi.org/10.5194/bg-15-4245-2018, 2018.

345

346   Otu-Larbi, F., Conte, A., Fares, S., Wild, O., and Ashworth, K.: FORCAsT-gs: Importance of Stomatal Conductance

347   Parameterization to Estimated Ozone Deposition Velocity, J. Adv. Model. Earth Syst., 13,

348   https://doi.org/10.1029/2021MS002581, 2021.

349

350   Paoletti, E., Schaub, M., Matyssek, R., Wieser, G., Augustaitis, A., Bastrup-Birk, A.M., Bytnerowicz, A., Günthardt-Goerg,

351   M.S., Müller-Starck, G., and Serengil, Y.: Advances of air pollution science: from forest decline to multiple-stress effects on

352   forest ecosystem services, Environ. Pollut., 158(6), 1986–1989, https://doi.org/10.1016/j.envpol.2009.11.023, 2010.

353

354   Papp, M., Fóti, S., Nagy, Z., Pintér, K., Posta, K., Fekete, S., Csintalan, Z., and Balogh, J.: Rhizospheric, mycorrhizal and

355   heterotrophic respiration in dry grasslands, Eur. J. Soil Biol., 85, 43–52, https://doi.org/10.1016/J.EJSOBI.2018.01.005, 2018.

356

357   Patton, E. G., and Finnigan, J. J.: Canopy turbulence, in Handbook of Environmental Fluid Dynamics, edited by: H. J. S.

358   Fernando, CRC Press/Taylor & Francis Group, Boca Raton, 311–327, 2013.

359

360   Paulot, F., Malyshev, S., Nguyen, T., Crounse, J. D., Shevliakova, E., and Horowitz, L. W.: Representing sub-grid scale

361   variations in nitrogen deposition associated with land use in a global Earth system model: implications for present and future

362   nitrogen deposition fluxes over North America, Atmos. Chem. Phys., 18, 17963–17978, https://doi.org/10.5194/acp-18-17963-

363   2018, 2018.

364

365   Perry, R. H., and Green, D. W.: Chemical Engineering Handbook, 6th ed., 2240 pp, McGraw-Hill, New York, 1984.

366

367   Pleim, J., and Ran, L.: Surface Flux Modeling for Air Quality Applications, Atmosphere, 2(3), 271–302,

368   https://doi.org/10.3390/atmos2030271, 2011.

369

370   Pleim, J. E., and Xiu, A.: Development and testing of a surface flux and planetary boundary layer model for application in

371   mesoscale models, J. Appl. Meteorol., 34, 16–32, https://doi.org/10.1175/1520-0450-34.1.16, 1995.

372

373   Potempski, S., and Galmarini, S.: Est modus in rebus: analytical properties of multi-model ensembles, Atmos. Chem. Phys., 9,

374   9471–9489, https://doi.org/10.5194/acp-9-9471-2009, 2009.

375

376 Potier, E., Loubet, B., Durand, B., Flura, D., Bourdat-Deschamps, M., Ciuraru, R., and Ogée, J.: Chemical reaction rates of

377 ozone in water infusions of wheat, beech, oak and pine leaves of different ages, Atmos. Environ., 151, 176–187,

378 https://doi.org/10.1016/j.atmosenv.2016.11.069, 2017.

379

380 Potier, E., Ogée, J., Jouanguy, J., Lamaud, E., Stella, P., Personne, E., Durand, B., Mascher, N., and Loubet, B: Multilayer

381 modelling of ozone fluxes on winter wheat reveals large deposition on wet senescing leaves, Agric. For. Meteorol., 211-212, 58–

382 71, https://doi.org/10.1016/j.agrformet.2015.05.006, 2015.

383

384 Putaud, J. P., Bergamaschi, P., Bressi M., Cavalli, F., Cescatti, A., Daou, D., Dell'Acqua, A., Douglas, K., Duerr, M., 20

385 Fumagalli, I., Goded, I., Grassi, F., Gruening, C., Hjorth, J., Jensen, N. R., Lagler, F., Manca, G., Martins Dos Santos, S.,

386 Matteucci, M., Passarella, R., Pedroni, V., Pokorska, O., and Roux, D.: JRC – Ispra Atmosphere – Biosphere – Climate

387 Integrated monitoring Station 2013 Report, EUR 26995 EN, https://doi.org/10.2788/926761, 73-93, 2014.

388

389 Ran, L., Pleim, J., Song, C., Band, L., Walker, J. T., and Binkowski, F. S.: A photosynthesis-based two-leaf canopy stomatal

390 conductance model for meteorology and air quality modeling with WRF/CMAQ PX LSM, J. Geophys. Res. Atmos., 122, 1930–

391 1952, https://doi.org/10.1002/2016JD025583, 2017.

392

393 Rannik, Ü., Altimir, N., Mammarella, I., Bäck, J., Rinne, J., Ruuskanen, T. M., Hari, P., Vesala, T., and Kulmala, M.: Ozone

394 deposition into a boreal forest over a decade of observations: Evaluating deposition partitioning and driving variables, Atmos.

395 Chem. Phys., 12, https://doi.org/10.5194/acp-12-12165-2012, 2012.

396

397 Rannik, Ü., Mammarella, I., Keronen, P., and Vesala, T.: Vertical advection and nocturnal deposition of ozone over a boreal pine

398 forest, Atmos. Chem. Phys., 9, 2089–2095, https://doi.org/10.5194/acp-9-2089-2009, 2009.

399

400 Rao, S. T., Galmarini, S., and Puckett, K.: Air Quality Model Evaluation International Initiative (AQMEII): advancing the state

401 of the science in regional photochemical modeling and its applications, Bull. Am. Meteorol. Soc., 92(1), 23–30,

402 https://doi.org/10.1175/2010BAMS3069.1, 2011.

403

404 Raupach, M. R.: Anomalies in flux-gradient relationships over forest, Boundary-Layer Meteorol., 16, 467–486,

405 https://doi.org/10.1007/bf03335385, 1979.

406

407 Ren, W., Tian, H., Liu, M., Zhang, C., Chen, G., Pan, S., Felzer, B., and Xu, X.: Effects of tropospheric ozone pollution on net

408 primary productivity and carbon storage in terrestrial ecosystems of China, J. Geophys. Res. Atmos., 112(D22),

409 https://doi.org/10.1029/2007JD008521, 2007.

410

411 Repola J.: Biomass equations for Scots pine and Norway spruce in Finland, Silva Fennica, 43(4), https://doi.org/10.14214/sf.184,
412 2009.

413

414 Ronda, R., De Bruin, H., and Holtslag, A.: Representation of the canopy conductance in modeling the surface energy budget for
415 low vegetation, J. Appl. Meteorol., 40, 1431–1444, https://doi.org/10.1175/1520-0450(2001)040<1431:ROTCCI>2.0.CO;2,
416 2001.

417

418 Rondón, A., Johansson, C., and Granat, L.: Dry deposition of nitrogen dioxide and ozone to coniferous forests, J. Geophys. Res.,
419 98(D3), 5159–5172, https://doi.org/10.1029/92JD0233, 1993.

420

421 Ryan, E. and Wild, O.: Calibrating a global atmospheric chemistry transport model using Gaussian process emulation and
422 ground-level concentrations of ozone and carbon monoxide, Geosci. Model Dev., 14, 5373–5391, https://doi.org/10.5194/gmd-
423 14-5373-2021, 2021.

424

425 Sabbatini, S., Mammarella, I., Arriga, N., Fratini, G., Graf, A., Hörtnagl, L., Ibrom, A., Longdoz, B., Mauder, M., Merbold, L.,
426 and Metzger, S.: Eddy covariance raw data processing for CO_2 and energy fluxes calculation at ICOS ecosystem stations, Int.
427 Agrophys., 32(4), 495–515, https://doi.org/10.1515/intag-2017-0043, 2018.

428

429 Savage, K. E., and Davidson, E. A.: Interannual variation of soil respiration in two New England forests, Global Biogeochem.
430 Cy., 15(2), 337–350, https://doi.org/10.1029/1999gb001248, 2001.

431

432 Schaller, C., Hofer, B., and Klemm, O.: Greenhouse gas exchange of a NW German peatland, 18 years after rewetting, J.
433 Geophys. Res., 127, e2020JG005960. https://doi.org/10.1029/2020JG005960, 2022.

434

435 Schuepp, P. H.: Turbulent transfer at the ground: On verification of a simple predictive model, Boundary-Layer Meteorol., 12,
436 171–186, https://doi.org/10.1007/BF0012197, 1977.

437

438 Schwede, D., Zhang, L., Vet, R., and Lear, G.: An intercomparison of the deposition models used in the CASTNET and
439 CAPMoN networks, Atmos. Environ., 45(6), 1337–1346, https://doi.org/10.1016/j.atmosenv.2010.11.050, 2011.

440 Sharma, A., Ojha, N., Ansari, T. U., Sharma, S. K., Pozzer, A., and Gunthe, S. S.: Effects of dry deposition on surface ozone
441 over South Asia inferred from a regional chemical transport model, ACS Earth Space Chem.,
442 https://dx.doi.org/10.1021/acsearthspacechem.0c00004, 2020.

443   Shuttleworth, W. J., and Wallace, J. S.: Evaporation from sparse crops – an energy combination theory, Q. J. Roy. Meteor. Soc.,

444   111, 839–855, https://doi.org/10.1002/qj.49711146510, 1985.

445

446   Silva, S. J., and Heald, C. L.: Investigating dry deposition of ozone to vegetation, J. Geophys. Res. Atmos., 123, 559–573,

447   https://doi.org/10.1002/2017JD027278, 2018.

448

449   Silva, S. J., Heald, C. L., Ravela, S., Mammarella, I., and Munger, J. W.: A deep learning parameterization for ozone dry

450   deposition velocities, Geophys. Res. Lett., 46, 983–989, https://doi.org/10.1029/2018GL081049, 2019.

451

452   Simpson, D., Benedictow, A., Berge, H., Bergström, R., Emberson, L. D., Fagerli, H., Flechard, C. R., Hayman, G. D., Gauss,

453   M., Jonson, J. E., Jenkin, M. E., Nyíri, A., Richter, C., Semeena, V. S., Tsyro, S., Tuovinen, J.-P., Valdebenito, Á., and Wind, P.:

454   The EMEP MSC-W chemical transport model – technical description, Atmos. Chem. Phys., 12, 7825–7865,

455   https://doi.org/10.5194/acp-12-7825-2012, 2012.

456

457   Sitch, S., Cox, P. M., Collins, W. J., and Huntingford, C.: Indirect radiative forcing of climate change through ozone effects on

458   the land-carbon sink, Nature, 448, 791–794, https://doi.org/10.1038/nature06059, 2007.

459

460   Slevin, D., Tett, S. F. B., and Williams, M.: Multi-site evaluation of the JULES land surface model using global and local data,

461   Geosci. Model Dev., 8, 295–316, https://doi.org/10.5194/gmd-8-295-2015, 2015.

462

463   Solazzo, E. and Galmarini, S.: A science-based use of ensembles of opportunities for assessment and scenario studies, Atmos.

464   Chem. Phys., 15, 2535–2544, https://doi.org/10.5194/acp-15-2535-2015, 2015.

465

466   Solberg, S., Hov, Ø., Søvdee, A., Isaksen, I. S. A., Coddevillee, P., De Backer, H., Forster, C., Orsolini, Y., and Uhse, K.,

467   European surface ozone in the extreme summer 2003, J. Geophys. Res., 113, D07307, https://doi.org/10.1029/2007JD009098,

468   2008.

469

470   Song, C., Katul, G., Oren, R., Band, L. E., Tague, C. L., Stoy, P. C., and McCarthy, H. R.: Energy, water, and carbon fluxes in a

471   loblolly pinestand: Results from uniform and gappy canopy models with comparisons to eddy flux data, J. Geophys. Res., 114,

472   G04021, https://doi.org/10.1029/2009JG000951, 2009.

473

474   Stella, P., Loubet, B., de Berranger, C., Charrier, X., Ceschia, E., Gerosa, G., Lamaud, F. E., Serça, D., George, C., and Ciuraru,

475   R.: Soil ozone deposition: Dependence of soil resistance to soil texture, Atmos. Environ., 119, 202–209,

476   https://doi.org/10.1016/j.atmosenv.2018.11.036, 2019.

477

478   Stella, P., Loubet, B., Lamaud, E., Laville, P., and Cellier, P.: Ozone deposition onto bare soil: A new parameterization, Agric.

479   For. Meteorol., 151(6), 669–681, https://doi.org/10.1016/j.agrformet.2011.01.015, 2011.

480

481   Steiner, A. L., Pressley, S. N., Botros, A., Jones, E., Chung, S. H., and Edburg, S. L.: Analysis of coherent structures and

482   atmosphere-canopy coupling strength during the CABINEX field campaign, Atmos. Chem. Phys., 11, 11921–11936, https://

483   doi.org/10.5194/acp-11-11921-2011, 2011.

484

485   Sun, S., Moravek, A., Trebs, I., Kesselmeier, J., and Sörgel, M.: Investigation of the influence of liquid surface films on O_3 and

486   PAN deposition to plant leaves coated with organic/inorganic solution, J. Geophys. Res. Atmos., 121, 14239–14256,

487   https://doi.org/10.1002/2016JD025519, 2016a.

488

489   Sun, S., Moravek, A., von der Heyden, L., Held, A., Sörgel, M., and Kesselmeier, J.: Twin-cuvette measurement technique for

490   investigation of dry deposition of O_3 and PAN to plant leaves under controlled humidity conditions, Atmos. Meas. Tech., 9(2),

491   599–617, https://doi.org/10.5194/amt-9-599-2016, 2016b.

492

493   Sun, S., Tai, A. P. K., Yung, D. H. Y., Wong, A. Y. H., Ducker, J. A., and Holmes, C. D.: Influence of plant ecophysiology on

494   ozone dry deposition: comparing between multiplicative and photosynthesis-based dry deposition schemes and their responses to

495   rising CO_2 level, Biogeosciences, 19, 1753–1776, https://doi.org/10.5194/bg-19-1753-2022, 2022.

496

497   Tai, A. P., Val Martin, M., and Heald, C. L.: Threat to future global food security from climate change and ozone air pollution,

498   Nat. Clim. Change, 4, 817, https://doi.org/10.1038/nclimate2317, 2014.

499

500   Tan, J., Fu, J. S., Dentener, F., Sun, J., Emmons, L., Tilmes, S., Sudo, K., Flemming, J., Jonson, J. E., Gravel, S., Bian, H.,

501   Davila, Y., Henze, D. K., Lund, M. T., Kucsera, T., Takemura, T., and Keating, T.: Multi-model study of HTAP II on sulfur and

502   nitrogen deposition, Atmos. Chem. Phys., 18, 6847–6866, https://doi.org/10.5194/acp-18-6847-2018, 2018.

503

504   Tang, W., Cohan, D. S., Morris, G. A., Byun, D. W., and Luke, W. T.: Influence of vertical mixing uncertainties on ozone

505   simulation in CMAQ, Atmos. Environ., 45, 2898–2909, https://doi.org/10.1016/j.atmosenv.2011.01.057, 2011.

506

507   Tebaldi, C., and Knutti, R.: The use of the multi-model ensemble in probabilistic climate projections, Phil. Trans. R. Soc. A.,

508   365, 2053–2075, https://doi.org/10.1098/rsta.2007.2076, 2007.

509

510   Thomas, C., and Foken, T.: Flux contribution of coherent structures and its implications for the exchange of energy and matter in

511   a tall spruce canopy, Boundary-Layer Meteorol., 123, 317–337, https://doi.org/10.1007/s10546-006-9144-7, 2007.

512

513 Travis, K. R., and Jacob, D. J.: Systematic bias in evaluating chemical transport models with maximum daily 8 h average
514 (MDA8) surface ozone for air quality applications: A case study with GEOS-Chem v9.02., Geosci. Model Dev., 12(8), 3641–
515 3648, https://doi.org/10.5194/gmd-12-3641-2019, 2019.
516
517 Urbanski, S., Barford, C., Wofsy, S., Kucharik, C., Pyle, E., Budney, J., McKain, K., Fitzjarrald, D., Czikowsky, M., and
518 Munger, J. W.: Factors controlling CO_2 exchange on timescales from hourly to decadal at Harvard Forest, J. Geophys. Res., 112,
519 G02020, https://doi.org/10.1029/2006jg000293, 2007.
520
521 USDA, Soil Texture Calculator: https://www.nrcs.usda.gov/wps/portal/nrcs/detail/soils/survey/?cid=nrcs142p2_054167, last
522 access: 8 June 2022.
523
524 U.S. EPA: Integrated Science Assessment for Ozone and Related Photochemical Oxidants, Document EPA/600/R-20/012,
525 Center for Public Health and Environmental Assessment, U.S. Environmental Protection Agency, Research Triangle Park, North
526 Carolina, 2020a.
527
528 U.S. EPA: Integrated Science Assessment for Oxides of Nitrogen, Oxides of Sulfur, and Particulate Matter – Ecological Criteria,
529 Document EPA/600/R-20/278, Center for Public Health and Environmental Assessment, U.S. Environmental Protection Agency,
530 Research Triangle Park, North Carolina, 2020b.
531
532 Vautard, R., Honore, C., Beekmann, M., and Rouil, L.: Simulation of ozone during the August 2003 heat wave and emission
533 control scenarios, Atmos. Environ., 39, 2957–2967, https://doi.org/10.1016/j.atmosenv.2005.01.039, 2005.
534
535 Vermeuel, M. P., Cleary, P. A., Desai, A. R., and Bertram, T. H.: Simultaneous measurements of O_3 and HCOOH vertical fluxes
536 indicate rapid in-canopy terpene chemistry enhances O_3 removal over mixed temperate forests, Geophys. Res. Lett., 48(3),
537 e2020GL090996, https://doi.org/10.1029/2020GL090996, 2021.
538
539 Vermeuel, M. P., Novak, G. A., Kilgour, D. B., Claflin, M. S., Lerner, B. M., Trowbridge, A. M., Thom, J., Cleary, P. A., Desai,
540 A. R., Bertram, T. H.: Observations of biogenic volatile organic compounds over a mixed temperate forest during the summer to
541 autumn transition, EGUsphere, https://doi.org/10.5194/egusphere-2022-1015, 2022.
542
543 Verry, E. S., Bay, R. R., and Boelter, D. H.: Physical properties of organic soils, in: Peatland biogeochemistry and watershed
544 hydrology at the Marcell Experimental Forest, edited by: Kolka, R. K., Sebestyen, S. D., Verry, E. S., and Brooks, K. N., CRC
545 Press, New York, 1–13, ISBN 9780429130007, 2011.
546

547   Vesala, T., Suni, T. Rannik, Ü., Keronen, P., Markkanen, T., Sevanto, S., Grönholm, T., Smolander, S., Kulmala, M., Ilvesniemi,
548   H., Ojansuu, R., Uotila, A., Levula, J., Mäkelä, A., Pumpanen, J., Kolari, P., Kulmala, L., Altimir, N., Berninger, F., Nikinmaa,
549   E., and Hari, P.: Effect of thinning on surface fluxes in a boreal forest, Global Biogeochem. Cy., 19(GB2001),
550   https://doi.org/10.1029/2004GB002316, 2005.

551

552   Visser, A. J., Ganzeveld, L. N., Goded, I., Krol, M. C., Mammarella, I., Manca, G., and Boersma, F. K.: Ozone deposition
553   impacts assessments for forest canopies require accurate ozone flux partitioning on diurnal timescales, Atmos. Chem. Phys., 12,
554   18393–18411, https://doi.org/10.5194/acp-21-18393-2021, 2021.

555

556   Vivanco, M. G., Theobald, M. R., García-Gómez, H., Garrido, J. L., Prank, M., Aas, W., Adani, M., Alyuz, U., Andersson, C.,
557   Bellasio, R., Bessagnet, B., Bianconi, R., Bieser, J., Brandt, J., Briganti, G., Cappelletti, A., Curci, G., Christensen, J. H., Colette,
558   A., Couvidat, F., Cuvelier, C., D'Isidoro, M., Flemming, J., Fraser, A., Geels, C., Hansen, K. M., Hogrefe, C., Im, U., Jorba, O.,
559   Kitwiroon, N., Manders, A., Mircea, M., Otero, N., Pay, M.-T., Pozzoli, L., Solazzo, E., Tsyro, S., Unal, A., Wind, P., and
560   Galmarini, S.: Modeled deposition of nitrogen and sulfur in Europe estimated by 14 air quality model systems: evaluation,
561   effects of changes in emissions and implications for habitat protection, Atmos. Chem. Phys., 18, 10199–10218,
562   https://doi.org/10.5194/acp-18-10199-2018, 2018.

563

564   Voldner, E. C., Barrie, L. A., and Sirois, A.: A literature review of dry deposition of oxides of sulphur and nitrogen with
565   emphasis on long-range transport modelling in North America, Atmos. Environ., 20, 2101–2123, https://doi.org/10.1016/0004-
566   6981(86)90305-7, 1986.

567

568   von Caemmerer, S. and Farquhar, G. D.: Some relationships between the biochemistry of photosynthesis and the gas exchange of
569   leaves, Planta, 153(4), 376–387, https://doi.org/10.1007/BF00384257, 1981.

570

571   Walmsley, P. and Wesely, M.: Modification of coded parametrizations of surface resistances to gaseous dry deposition, Atmos.
572   Environ., 30, 1181–1196, https://doi.org/10.1016/1352-2310(95)00403-3, 1996.

573

574   Walker, T. W.: Applications of adjoint modelling in chemical composition: Studies of tropospheric ozone at middle and high
575   northern latitudes, PhD thesis, Univ. of Toronto, Toronto, Canada, https://hdl.handle.net/1807/65764, 2014.

576

577   Wang, Y., Jacob, D. J., and Logan, J. A.: Global simulation of tropospheric O_3-NO_x-hydrocarbon chemistry: 1. Model
578   formulation, J. Geophys. Res., 103(D9), 10713–10725, https://doi.org/10.1029/98JD00158, 1998.

579

580   Wesely, M. L.: Parameterization of surface resistances to gaseous dry deposition in regional-scale numerical models, Atmos.
581   Environ., 23(6), 1293–1304, https://doi.org/10.1016/0004-6981(89)90153-4, 1989.

Wesely, M. L. and Hicks, B. B.: Some factors that affect the deposition rates of sulphur dioxide and similar gases on vegetation, Journal of the Air Pollution Control Association, 27, 1110–1116, https://doi.org/10.1080/00022470.1977.10470534, 1977.

Wesely, M. L., and Hicks, B. B.: A review of the current status of knowledge on dry deposition, Atmos. Environ., 34, 2261–2282, https://doi.org/10.1016/S1352-2310(99)00467-7, 2000.

Wild, O.: Modelling the tropospheric ozone budget: Exploring the variability in current models, Atmos. Chem. Phys., 7, 2643–2660, https://doi.org/10.5194/acp-7-2643-2007, 2007.

Wolfe, G. M., Hanisco, T. F., Arkinson, H. L., Bui, T. P., Crounse, J. D., Dean-Day, J., Goldstein, A., Guenther, A., Hall, S. R., Huey, G. Jacob, D. J., Karl, T., Kim, P. S., Liu, X., Marvin, M. R., Mikoviny, T., Miszta, P. K., Nguyen, T. B., Peischl, J., Pollack, I., Ryerson, T., St. Clair, J. M., Teng, A., Travis, K. R., Ullmann, K., Wennberg, P. O., and Wisthaler, A.: Quantifying sources and sinks of reactive gases in the lower atmosphere using airborne flux observations, Geophys. Res. Lett., 42, 8231–8240, https://doi.org/10.1002/2015GL065839, 2015.

Wolfe, G. M., Thornton, J. A., McKay, M., and Goldstein, A. H.: Forest-atmosphere exchange of ozone: sensitivity to very reactive biogenic VOC emissions and implications for in-canopy photochemistry, Atmos. Chem. Phys., 11, 7875–7891, https://doi.org/10.5194/acp-11-7875-2011, 2011.

Wong, A. Y. H., Geddes, J. A., Tai, A. P. K., and Silva, S. J.: Importance of dry deposition parameterization choice in global simulations of surface ozone, Atmos. Chem. Phys., 19, 14365–14385, https://doi.org/10.5194/acp-19-14365-2019, 2019.

Wong, A. Y. H., Geddes, J. A., Ducker, J. A., Holmes, C. D., Fares, S., Goldstein, A. H., Mammarella, I., and Munger, J. W.: New evidence for the importance of non-stomatal pathways in ozone deposition during extreme heat and dry anomalies, Geophys. Res. Lett., e2021GL095717, 2022.

Wu, Z., Staebler, R., Vet, R., and Zhang, L.: Dry deposition of O_3 and SO_2 estimated from gradient measurements above a temperate mixed forest, Environ. Pollut., 202–210, https://doi.org/10.1016/j.envpol.2015.11.052, 2016.

Wu, Z. Y., Zhang, L., Wang, X. M., and Munger, J. W.: A modified micrometeorological gradient method for estimating O3 dry depositions over a forest canopy, Atmos. Chem. Phys., 15, 7487–7496, https://doi.org/ 10.5194/acp-15-7487-2015, 2015.

615   Wu Z., Schwede D. B., Vet R., Walker J. T., Shaw M., Staebler R., and Zhang L.: Evaluation and intercomparison of five North

616   American dry deposition algorithms at a mixed forest site, J. Adv. Model. Earth Syst., 10, 1571–1586,

617   https://doi.org/10.1029/2017MS001231, 2018.

618

619   Ye, Z., Wang, X., and Zhang, L.: Diagnosing the Model Bias in Simulating Daily Surface Ozone Variability Using a Machine

620   Learning Method: The Effects of Dry Deposition and Cloud Optical Depth, Environ. Sci. Tech.,

621   https://doi.org/10.1021/acs.est.2c05712, 2022.

622

623   Xiu, A., and Pleim, J. E.: Development of a land surface model part I: Application in a mesoscale meteorology model, J. Appl.

624   Meteorol., 40, 192–209, https://doi.org/10.1175/1520-0450(2001)040<0192:DOALSM>2.0.CO;2, 2001.

625

626   Xin, Q., Dai, Y., and Liu, X.: A simple time-stepping scheme to simulate leaf area index, phenology, and gross primary

627   production across deciduous broadleaf forests in the eastern United States, Biogeosciences, 16, 467–484,

628   https://doi.org/10.5194/bg-16-467-2019, 2019.

629

630   Yi, C.: Momentum transfer within canopies, J. Appl. Meteorol. Climatol., 47, 262–275,

631   https://doi.org/10.1175/2007JAMC1667.1, 2008.

632   Young, P. J., Naik, V., Fiore, A. M., Gaudel, A., Guo, J., Lin, M. Y., Neu, J. L., Parrish, D. D., Rieder, H. E., Schnell, J. L.,

633   Tilmes, S., Wild, O., Zhang, L., Ziemke, J. R., Brandt, J., Delcloo, A., Doherty, R. M., Geels, C., Hegglin, M. I., Hu, L., Im, U.,

634   Kumar, R., Luhar, A., Murray, L., Plummer, D., Rodriguez, J., Saiz-Lopez, A., Schultz, M. G., Woodhouse, M. T., and Zeng, G.:

635   Tropospheric Ozone Assessment Report: Assessment of global-scale model performance for global and regional ozone

636   distributions, variability, and trends, Elem. Sci. Anth., 6, 10, https://doi.org/10.1525/elementa.265, 2018.

637   Zahn, A., Weppner, J., Widmann, H., Schlote-Holubek, K., Burger, B., Kühner, T., and Franke, H.: A fast and precise

638   chemiluminescence ozone detector for eddy flux and airborne application, Atmos. Meas. Tech., 5, 363–375,

639   https://doi.org/10.5194/amt-5-363-2012, 2012.

640

641   Zhao, Y., Zhang, L., Zhou, M., Chen, D., Lu, X., Tao, W., Liu, J., Tian, H., Ma, Y., and Fu, T.-M.: Influences of planetary

642   boundary layer mixing parameterization on summertime surface ozone concentration and dry deposition over North China,

643   Atmos. Environ., 218, 116950, https://doi.org/10.1016/j.atmosenv.2019.116950, 2018.

644

645   Zeng, X., Shaikh, M., Dai, Y., Dickinson, R. E. and Myneni, R.: Coupling of the Common Land Model to the NCAR

646   Community Climate Model, J. Clim., 15(14), 1832–1854, DOI:10.1175/1520-0442(2002)015<1832:COTCLM>2.0.CO;2, 2002.

647

648   Zhang, L., Brook, J. R., and Vet, R.: On ozone dry deposition—With emphasis on non-stomatal uptake and wet canopies, Atmos.
649   Environ., 36(30), 4787–4799, https://doi.org/10.1016/S1352-2310(02)00567-8, 2002a.
650
651   Zhang, L., Brook, J. R., and Vet, R.: A revised parameterization for gaseous dry deposition in air-quality models, Atmos. Chem.
652   Phys, 3(6), 2067–2082, https://doi.org/10.5194/acp-3-2067-2003, 2003.
653
654   Zhang L., Moran, M. D., and Brook, J. R.: A comparison of models to estimate in-canopy photosynthetically active radiation and
655   their influence on canopy stomatal resistance, Atmos. Environ., 35, 4463–4470, 2001.
656
657   Zhang, L., Moran, M. D., Makar, P. A., Brook, J.R., and Gong, S.: Modelling gaseous dry deposition in AURAMS: a unified
658   regional air-quality modelling system, Atmos. Environ., 36, 537–560, https://doi.org/10.1016/S1352-2310(01)00447-2, 2002b.